UNIVERSITY OF CALIFORNIA
Santa Barbara

Nano to Micro Scale Coulter Counters

A Dissertation submitted in partial satisfaction
of the requirements for the degree of

Doctor of Philosophy

in

Electrical Engineering

by

Sukru Yemenicioglu

Committee in Charge:

Professor Luke Theogarajan, Chair

Professor Deborah Kuchnir Fygenson

Professor Carl Meinhart

Professor Jon Schuller

Professor Dmitri Strukov

September 2015

The Dissertation of
Sukru Yemenicioglu is approved:

Professor Deborah Kuchnir Fygenson

Professor Carl Meinhart

Professor Jon Schuller

Professor Dmitri Strukov

Professor Luke Theogarajan, Committee Chairperson

September 2015

Nano to Micro Scale Coulter Counters

by

Sukru Yemenicioglu

For my wife, son and family.

Acknowledgements

Prof. Meinhart for his guidance in COMSOL simulations
Justin Rofeh and Avantika Sodhi for their help in fabrication
Jennifer Chen for Jenset Amplifier
Laura Innes and Prof. Siwy from UC Irvine for cells
Lourdes Velasquez and Prof. Fygenson for DNA Nanotubes
Prof. Luke Theogarajan for unwavering support
UCSB Nanofab Staff
All the Biomimetic Circuits and Systems Group Members

Curriculum Vitæ

Sukru Yemenicioglu

Education
Electrical Engineering BS, University of Illinois Urbana Champaign 2008
Electrical Engineering MS, University of Illinois Urbana Champaign 2010

Experience:

Prof. Luke Theogarajan's BCNS Group, UCSB – August 2011-Present

- Successfully detected circulating tumor cells using self-designed and fabricated microfluidic chips
- Simulated current flow and cell deformation in the fabricated chips using COMSOL to deduce cell attributes
- Designed and fabricated electrode-embedded free-standing membranes along with 3D printed interfacing assembly, aiming to improve spatial resolution in solid-state membranes
- Coded a graphical user interface in Labview for a custom-design amplifier, able to handle and visualize 2 channel 16-bit 5MHz continuous data acquisition, corresponding to 5GB/min data
- Designed and implemented automated curve fitting, level finding and pattern recognition algorithms for 200GB+ time-series datasets for DNA Sequencing and Circulating Tumor Cell Detection research

Nabsys, Inc – June 2013-September 2013

- Devised a folder crawler algorithm in R to parse unformatted data using keyword searches and mined physical parameters, correlating with chip yield
- Developed a model based on automated curve-fitting to several datasets and designed automatic plotting algorithms in R to evaluate chip yield, providing actionable insights for design improvement item Improved DNA translocation rate prediction algorithm in R by optimizing function calls and array handling, resulting in 6x faster data analysis

Prof. Rashid Bashir's LIBNA Group, UIUC – August 2008-August 2010

- Designed and fabricated novel solid-state free-standing membranes for DNA sequencing research
- Performed DNA translocation experiments and analyzed the data acquired on the fabricated membranes using self-written Matlab algorithms to demonstrate advantages of different membrane materials

Prof. Gregory Timps NanoBio Group, UIUC – September 2006-April 2008

- Created algorithms in Matlab to detect low SNR stochastic pulses on rapidly drifting time series data by using a moving average filter to determine the baseline and event-triggers on dynamically adjusted thresholds, providing a data-analysis tool for DNA Sequencing research datasets in excess of 300MB

- Coded Labview algorithms to automate and interface measurement instruments

Awards

- MIT Clean Energy Prize Competition 2010 semi-finalist in Transportation Category

Publications:

- S. Yemenicioglu, L. Innes, Z. Siwy and L.Theogarajan, Electrical Detection of Circulating Tumor Cells with Highly Scalable Microfluidics, in Manuscript, 2015.
- S. Yemenicioglu, L. Velasquez, D. K. Fygenson, L. Theogarajan, Potential for Sorting DNA Nanotubes using Synthetic Nanopores, in Manuscript, 2015.
- D. Morton , S. Mortezaei, S. Yemenicioglu, M. J. Isaacman, I. C. Nova, J. Gundlach, and L. Theogarajan, Tailored Polymeric Membranes for Mycobacterium Smegmatis Porin A (MspA) based biosensors, Journal of Materials Chemistry B, accepted on 05/05/2015.
- C.-H. Chen, S. Yemenicioglu, A. Uddin, E. Corigliano and L. Theogarajan, A CMOS Enhanced Solid-State Nanopore Based Single Molecule Detection

Platform, Engineering in Medicine and Biology Conference 2013, 2013,pp. 164-167.

- A. Uddin, S. Yemenicioglu, C.-H. Chen, E. Corigliano, K. Milaninia and L. Theogarajan, Integration of Solid-State Nanopores in a 0.5 m CMOS Foundry Process, Nanotechnology, vol. 24, 2013, p. 155501.
- A. Uddin, S. Yemenicioglu, C.-H. Chen, E. Corigliano, K. Milaninia, F. Xia, K. Plaxco, and L. Theogarajan, Biosensing with integrated CMOS nanopores, Proc. SPIE 8460, Biosensing and Nanomedicine V, Oct. 2012, pp. 846010846010.
- A. Uddin, C. Chen, S. Yemenicioglu, K. Milaninia, E. Corigliano and L. Theogarajan, ”Integrated Nanopore Detectors in a Standard Complementary Metal-Oxide-Semiconductor Process.” Bulletin of the American Physical Society, vol. 57, 2012.
- S. Yemenicioglu, Stability and bandwidth investigation of alternative structures for nanopore sensors, M.S. Thesis, UIUC, Champaign, IL, 2010.
- V. Dimitrov, U. Mirsaidov, D. Wang, T. Sorsch, W. Mansfield, J. Miner, F. Klemens, R. Cirelli, S. Yemenicioglu, and G. Timp, Nanopores in solid-state membranes engineered for single molecule detection, Nanotechnology, vol. 21, 2010, p. 065502.

- B.M. Venkatesan, B. Dorvel, S. Yemenicioglu, N. Watkins, I. Petrov, and R. Bashir, Highly Sensitive, Mechanically Stable Nanopore Sensors for DNA Analysis, Advanced Materials, vol. 21, 2009, pp. 2771-2776.
- M. Venkatesan, S. Yemenicioglu, B. Dorvel, and R. Bashir, Fabrication And Characterization Of Tunable, Low Stress Al_2O_3 Nanopores For The Electronic Detection Of Biomolecules, Biophysical Journal, vol. 96, 2009, pp. 645a-645a.
- Q. Zhao, J. Comer, V. Dimitrov, S. Yemenicioglu, A. Aksimentiev, and G. Timp, Stretching and unzipping nucleic acid hairpins using a synthetic nanopore, Nucleic Acids Research, vol. 36, Mar. 2008, pp. 1532 -1541.

Abstract

Nano to Micro Scale Coulter Counters

Sukru Yemenicioglu

As biotechnology advances, personalized medicine has become one of the prominent trends. It can be briefly described as an effort to provide preventative, diagnostic and treatment measures for health problems implemented on an individual basis. Resistive pulse technique is a measurement scheme that has found a wide range of applications in this field. In this dissertation, research on devices that are based on resistive pulse technique from nano to micro scale are presented.

Nanopore sensing, one of the major candidate technologies for next-generation DNA sequencing is an example of nano-scale application of this technique. It is a promising technology due to its potential to provide label-free, robust and rapid DNA sequencing [7]. However, there are several challenges in reaching this ultimate goal [97]. We present an architecture for solving the aggregate base detection problem through ubiquitous, cost-effective CMOS fabrication. We describe the challenges and advantages of this approach.

Beyond DNA sequencing, there are many exciting potential applications of synthetic nanopores, such as sizing and investigating polymer based constructs. Due to its well understood properties, DNA can be used to build functional nano-

mechanical structures [59, 71, 101]. However, DNA nano-structures usually lack a robust validation and quality control method, leading to populations that are poorly characterized in terms of shape and size. In this dissertation, the feasibility of utilizing synthetic nanopores to characterize a high volume of DNA nanotubes is investigated.

Next, a micro scale application of resistive pulse technique for cancer diagnosis is explored. Particularly, Circulating Tumor Cells(CTCs) have recently emerged as indicators of cancer metastasis [2]. Thus, efficient detection of CTCs can provide non-invasive biopsy, enable personalized medicine and help understand cancer biology. Currently used immunoassay based CTC detection techniques are inefficient and insufficient to classify extremely heterogeneous CTCs such as Circulating Melanoma Cells(CMCs). Cancer cells have markedly different physical attributes, such as size and stiffness, and can be used to distinguish tumor cells from normal cells. We report a micro-fluidic chip potentially meeting the urgent need to detect individual CTCs in a label-free, fast and inexpensive fashion while maintaining cell viability. We present the design, fabrication and modeling of microfluidic channels that enable the classification of CTCs based on their size and stiffness. We use the device was to classify melanoma (MNT1)and breast cancer (MCF-7) cells both alone and in the presence of blood cells.

Contents

List of Figures

Chapter 1

Introduction

As biotechnology advances, personalized medicine has become a prominent trend. It can be briefly described as an effort to provide preventative, diagnostic and treatment measures for health problems on an individual basis. The resistive pulse technique is a measurement scheme that has found a wide range of applications in personalized medicine. In this dissertation, research on devices that use the resistive pulse technique on both nano and micro scale are presented.

Nanopore sensing, one of the major candidate technologies for next-generation DNA sequencing is an example of nano-scale application of this technique. It is a promising technology due to its potential to provide label-free, robust and rapid DNA sequencing [7]. There are two branches of the field: synthetic nanopores and biological nanopores. Initial experimental results from two decades ago have lead to a full-fledged technology at the verge of commercialization.

Nanopore research began with studies on alpha hemolysin, a biological nanopore found on bacteria, embedded in lipid membranes. Due to limitations associated with lipid membranes, a drive for mimicking the geometry in a solid-state device emerged. The race to thin down the solid state membranes to achieve high spatial resolution hit a physical limit when measurements with graphene, a virtually 2D membrane, showed that the E-field around the pore begins to dominate and the number of bases detected remains more than ten at a time [32, 34, 64, 80].

Research on biological nanopores continued in parallel and resulted in the discovery of a pore from a bacteriophage, MspA, with a conical shape. Data using these pores showed, the spatial resolution of the measurement can be improved down to a single base [11, 17, 19, 30, 57, 60, 61]. Despite these advancements, there are still several challenges to reach the ultimate goal of de novo sequencing using nanopores. In the case of biological nanopores, forming stable membranes with single protein insertion in an automated manner remains a major obstacle. On the other hand, reaching single base resolution with solid-state nanopores is still an on-going research. We present an architecture for solving the aggregate base detection problem in synthetic nanopores through ubiquitous, cost-effective

CMOS fabrication. The challenges and advantages of this approach are described in Chapter 2, Section 1.

Beyond DNA sequencing, there are many exciting potential applications of synthetic nanopores, such as sizing and investigating polymer based constructs [7, 70]. In the last decade, numerous ways of utilizing DNA molecules′ helical complementary structure have emerged. Proof of principle structures, like boxes, pores and masking features for nano-fabrication have been designed and documented [8, 59, 71, 101]. These structures provide an exciting paradigm for devising constructs for drug delivery, subcellular motors and nano-manipulation capable robot arms, furthering the applications of nanotechnology. However, DNA nanostructures usually lack a robust validation and quality control method, leading to populations that are poorly characterized in terms of shape and size [71]. In Chapter 2 Section 2, the feasibility of using synthetic nanopores to characterize a high volume of DNA nanotubes is investigated.

Finally in Chapter 3, a micro scale application of resistive pulse technique for cancer diagnosis is explored. Circulating Tumor Cells(CTCs) have recently emerged as indicators of cancer metastasis [2]. Thus, efficient detection of CTCs can provide non-invasive biopsy, enable personalized medicine and help understand cancer biology. Some proteins expressed on the surface of the cancer cells are accurate identifiers for cancer cell type. The commonly used methods rely on immobilization of the cells using anti-body detection of specific cell membrane proteins, requiring cancer-type specific surface functionalization and high surface to volume ratio channels. Given the wide variety of cancer types, immunoassay based CTC detection techniques are inefficient and insufficient to classify extremely heterogeneous CTCs such as Circulating Melanoma Cells(CMCs). However, in addition to surface proteins, cancer cells have markedly different physical attributes, such as size and stiffness. That can be used to distinguish tumor cells from normal cells. A micro-fluidic chip could potentially meet the urgent need to detect individual CTCs in a label-free, fast and inexpensive fashion while maintaining cell viability. We present the design, fabrication and modeling of microfluidic channels that enable the classification of CTCs based on their size and stiffness. We use the device was to classify melanoma (MNT1)and breast cancer (MCF-7) cells both alone and in the presence of blood cells.

At the heart of all these seemingly separate studies is the Coulter Counter, a devices that works on the basis of the resistive pulse technique. The applications of this technique have been revolutionizing many industries as well as the medical field. In the next section, an overview of Coulter Counters is given.

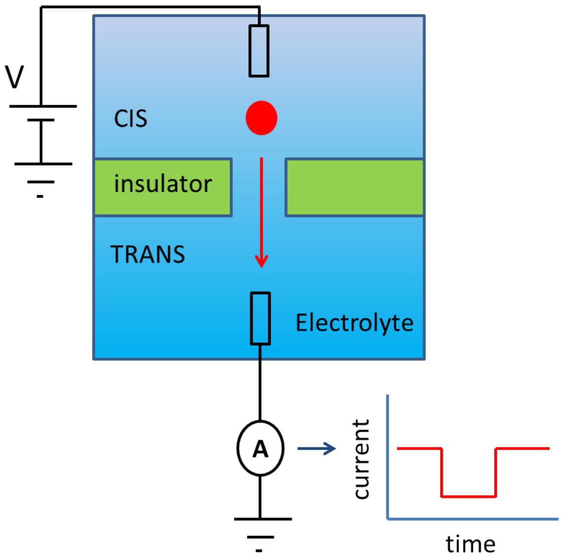

Figure 1.1: Schematic of a Coulter Counter.

1.1 Coulter Counters

Coulter Counters were invented in the wake of World War II, with the concern of testing blood count rapidly for a large population in the case of a nuclear war. At the time, the blood counting tests were done under the microscope with manual counting of individual cells in an area. Wallace H. Coulter suggested suspending blood in an electrolyte and making a flow-based high throughput test [3].

The idea is to form two reservoirs of electrolyte by separating them with a membrane. The membrane contains a single pore that is slightly bigger than the particle of interest. When a voltage is applied across these two reservoirs, the only conduction path is through the pore. Particles added to the CIS reservoir are translocated across the membrane by either electrophoresis, pressure, or both, to the TRANS reservoir. While the particle is traversing the pore, it induces an impedance change in proportion to the ratio of its volume to the volume of the pore. This method of detection is called Coulter Principle or resistive pulse technique.

The following expression is the governing equation of the resistive pulse technique:

$$\frac{\Delta R}{R} = f \cdot \frac{v}{V} \tag{1.1}$$

where the ratio of ΔR, the resistance change to the total resistance R is equal to the ratio of the volume of the particle,v, to the volume of the constriction, V, with a multiplier called the electrical shape factor, f. Essentially, the device works on the basis of charge exclusion. The interrogated particle functions as an insulator during the translocation, obstructing the passage of ions and causing an increase in the electrical resistance of the channel.

Using this technique, one can thus measure both the particle volume and the particle count. In addition, force spectroscopy measurements can be performed by driving a complex particle with attached secondary structures through a small pore and recording the amount of force required to cleave the secondary structure at the pore interface, allowing the main particle to pass through. The same principles apply from the macro scale all the way down to the nano scale, allowing the use of the technique for particles as minuscule as DNA nucleotides or as large as cells.

1.2 Challenges in Nanopore Sequencing

In this section, an overview of nanopore sequencing in its current state will be discussed. Nanopore sequencing began with a simple concept of differentiating each nucleic base by exploiting their volumetric differences in a nanopore. Shortly after the report that homopolymer strands of Adenine could be distinguished from homopolymer strands of Cytosine [51], nanopore sequencing gathered momentum as an interesting research topic. Nanopores presented the potential for cheaper, faster, robust and label-free DNA sequencing with long reads. As the understanding of the physics of nanopores expanded, the complications in accomplishing this goal became apparent [10]. Over the last two decades, significant distance has been covered in nanopore science for resolving these complications to replace the commonly used ”sequencing-by-synthesis” methods.

There are two main types of nanopores in use for nanopore research; biological and synthetic nanopores. Although synthetic nanopores are superior in terms of their mechanical stability and fabrication [97], currently biological nanopores are at the core of the first commercial nanopore sequencing device due to their advantage of molecular precision [97].

Synthetic nanopores are usually fabricated using CMOS processes on semiconductor materials. Therefore, they are also called solid-state nanopores. A common architecture for experimentation is 10 to 30nm thick low-stress LPCVD silicon nitride membranes on TEM-grid sized silicon chips. Although robust, this structure provides a signal due to at least 30 bases at a time. In order to alleviate this problem the use of 2D membranes had been proposed. In 2010 several groups reported double stranded DNA(dsDNA) translocation through graphene membranes over-laid on silicon nitride and silicon oxide apertures [32, 34, 64, 80]. As Meni Wanunu pointed out [97], even though the membrane thickness is minimal, the current signature would not be due to 1 base at a time. Resistance associated with the pore is a combination of access resistance and pore resistance. With thin membranes, although the pore resistance can be decreased, the access resistance remains the same. In other words, the E-field extending outside the pore becomes the dominant factor in determining the signal acquired from a translocation event.

Another major problem is the requirement for measuring dsDNA versus single stranded DNA. ssDNA strands are more likely to form secondary structures and coil, leading to unpredictable translocation time and characteristics. However, dsDNA does not have a base specific volumetric difference. Each base is complemented by another and shielded between the backbone. Moreover, it is known that AT and CG pairs have different transverse conductivity. Therefore, membranes with trans-electrodes have been developed.

First successful examples of solid state nanopores with electrodes were fabricated over free-standing silicon nitride membranes. In Tomoji Kawais group demonstrated a planar channel with gold electrodes [91, 92]. The short coming of this approach was the stochastic nature of the DNA entry in to the channel. DNA that entered the channel did not enter in the same orientation every time. This lead to distributions of nucleic base signals that mostly overlap each other and prohibited differentiation of individual bases.

On the other hand, the classical biological nanopore experiments were done with alpha-hemolysin pores embedded in lipid bilayers [51]. The challenges of this system were unstable membrane formation, ssDNA translocation requirement and about 5 base resolution. Recently, MspA pores have become the gold standard for biological nanopores due to their 3 base resolution. There are also reports of achieving single base resolution with a modified MspA pore [60]. This is possible due to the charge distribution and geometry of the pore. In addition, the stochastic nature of the DNA translocation and the ssDNA translocation requirements were alleviated by the attachment of a DNA polymerase at the entry of the pore that unzips or builds dsDNA, controlling the translocation rate of the DNA by a ratcheting motion. Furthermore, automation of membrane formation has been demonstrated, solving one of the greatest impediments to parallelization of sequencing measurements [52,72]. One more advancement propelling biological pores as a candidate platform for next generation sequencing was replacing lipid membranes with liquid crystal polymer membranes [68]. These membranes show greater physical durability than their lipid counterparts. With all this progress, the MinION from Oxford Nanopores has an accuracy of 85% [4]. This can be explained by 3 base resolution and ultimately the use of a polymerase for controlling the rate of translocation. The polymerase during the translocation is operated in the reverse direction to its function, leading to occasional slips while ratcheting the DNA. This makes repeating sequences such as AAAAAAA, hard to read as the time stamp of the signal associated with each base is not uniformly distributed. Therefore, the number of repeated bases can not be resolved accurately.

Given the challenges associated with biological nanopores, my research focused on tackling the aggregate response due to multiple bases in solid-state nanopores. I designed an architecture that would enable removing the access resistance from the nanopore signal, using cost-effective, ubiquitous CMOS fabrication techniques. It was a proof-of-principle device aimed at increasing the base resolution in solid-state nanopores.

1.3 Alternative Applications of Nanopores

The mechanical robustness and tunable diameter of nanopores on silicon nitride membranes make them a great candidate for multiple applications beyond DNA sequencing. Analysis of proteins, epigenomics related studies and force spectroscopy measurements constitute the most prominent topics of research. Furthermore, they can be considered as a nanosensing platform for analyzing any water-soluble analyte [7].

De novo protein sequencing is a very challenging field; as opposed to 4 bases there are 20 different amino acis to differentiate [7]. The human genomic information contains roughly 20000 proteins but they can be folded in many different configurations, achieving a plethora of functionality. Recently it has been reported that the proteins can be unfolded and translocated through pores. This may ultimately prove to be another major area where nanopores take the lead in analysis.

It has been shown that DNA methylation sites can be important indicators of gene regulation, controlling the development of diseases such as cancer [66,82]. In the Bashir and Timp groups, methylation sites were detected using synthetic nanopores with single methylated CpG dinucleotide. Using this method, the methylation level could also be quantified. Nanopores can be used for studying epigenomics for tracking gene regulation.

Due to its well understood properties, DNA can be used to build functional nano-mechanical structures [8, 59, 71, 101]. HHowever, DNA nano-structures usually lack a robust validation and quality control method, leading to populations that are poorly characterized in terms of shape and size [71]. In this project, the feasibility of utilizing synthetic nanopores to sort and characterize a high volume of DNA nanotubes is also investigated.

1.4 Circulating Tumor Cell Detection

Circulating tumor cells (CTCs) are blood borne cancer cells released from primary and secondary tumors with metastatic potential [6, 74]. The frequency and occurrence of CTCs monitored during the course of cancer therapy has been correlated with the prognosis of various types of cancers including melanoma [20, 22, 23, 67, 69]. While primary tumors are often operable, many metastatic tumors are difficult and dangerous to biopsy. Thus CTCs from peripheral blood could provide 'liquid' non-invasive biopsy, perhaps even replacing conventional tissue biopsies and offering new insight into cancer biology. The heterogeneity of CTCs can help explain late-stage relapse in patients and reasons for suboptimal outcomes in cancer therapy. However, the true potential of CTCs can be reached only if the captured cells remain viable.

It is estimated that there are only a few CTCs per 1ml of blood, meaning a few cells amidst billions of red blood cells and millions of leukocytes. More importantly the threshold for cancer metastasis is around 5 cells/7.6ml. Heterogeneity of tumor cells, even from the same primary tumor in the same patient, necessitates cell specific treatment [75]. Thus isolation and detection of CTCs requires high capture efficiency and minimal sample treatment [54]. In addition, CTCs are fragile; Large shear forces and approaches like filtration may cause a biased result and large variability [29]. Moreover, detection of circulating melanoma cells is particularly challenging due to lack of universal biomarkers [36, 43, 50, 87, 96].

Due to the enormous complexity and heterogeneity of cancer cells, one of the most successful detection methods of CTCs involves multiple immunofluorescent markers in combination with microscopic analysis [16, 62]. This approach is labor intensive, compromises cell viability, requires expensive chemicals, equipment and trained personnel, and thus cannot be performed as a routine procedure. The only FDA approved platform for CTC detection, CellSearch by Veridex [13, 90], captures cells overexpressing EpCam using magnetic particles covered with anti-EpCAM. Such targeted separation does not allow detection of cancers, which do not overexpress EpCAM e.g. cutaneous melanoma, tumors which downregulate EpCAM expression during epithelial-mesenchymal transition(EMT), and cancer stem cells. CellSearch is expensive, not easily automated, and cells are not viable for further analysis [54]. Microfluidic based separation has been increasingly used for CTC enrichment, often based on immunoassay coupled with the benefits of microfluidics such as small sample volume, preconcentration and sorting [1, 31, 38, 44, 53, 58]. One notable exception is the use of centrifugal forces in a curved microchannel to separate CTCs from whole blood [42].

Cancer metastasis requires mechanical properties facilitating their egress and ingress to and from the bloodstream (extra(intra)vasation) [49, 99], and cancer cells are often characterized by higher deformability compared to normal cells [24, 25,88,89,100]. Indeed, many studies have revealed different mechanical properties of CTCs across various cancers compared to non-malignant cells. Increased stiffness was also indicative of weaker metastatic potential of melanoma [98]. These studies were performed by atomic force microscopy and magnetic tweezers, neither of which is suitable for automated high-throughput analysis, and by a series of microfluidic devices [24, 25, 88, 89, 100]. However, the microfluidic channels designed to probe mechanical properties of cells had constrictions smaller than the cells to be detected, leading to cell deformation and compromising their viability [12, 15]. Rather than probing the cell, investigating physical features such as the size disparity between CTCs(larger) and leukocytes, and non-malignant epithelial cells enable a simple approach to CTC detection [18, 21]. Size exclusion has met with some success in detecting melanoma cells [26, 81]. However, size exclusion using filters with pre-determined pore diameters does not account for softer mechanical properties of CTCs, which enable them to pass through constrictions narrower than their diameter.

We report a micro-fluidic chip potentially meeting the urgent need to detect individual CTCs in a label-free, fast and inexpensive fashion while maintaining cell viability. Our chip couples the resistive pulse technique with controlled pressure gradients to measure size and stiffness of cells without applying large shearing forces. We present the design, fabrication and modeling of microfluidic channels enabling the classification of CTCs based on their size and stiffness. We find the interference due to the presence of blood cells is minimal and demonstrate the reliability of the device in detecting CTCs from a blood sample.

Chapter 2

Solid-State Nanopores

2.1 Solid-State Nanopore with Embedded Electrodes

CMOS Integrated Solid State Nanopores had a very interesting advantage in terms of its concept compared to other platforms [14, 93–95]. The membrane was between two electrodes made of poly silicon, essentially enabling the electrodes to bring the voltage up to the entry of the nanopore. The implication of this architecture is, the voltage drop that adds up to the pore resistance is circumvented, leading to higher base resolution. However, this project had some very challenging aspects such as the fact that preparation of each membrane took almost a week of fabrication. In addition, the circuitry inside the chip was very difficult to activate due to the small pitch between the contact pads in a 3mmx3mm chip. It required a specialized socket to make measurements and this did not ensure a good seal between the chip and the reservoirs.

In order to realize embedding electrodes in a nanopore, the best path to take was replacing the poly silicon electrodes with platinum electrodes in a completely new platform without the circuitry to show the proof-of-concept. The development cycle for etching nanopores using batch production techniques such as e-beam lithography can be very time-consuming. Therefore the preferred method was TEM drilling. In order to achieve this goal the die size was brought down to a 2.75mmx2.85mm octagon, as the standard membranes allowed in the TEM chamber had a diameter of 3mm. Another design consideration was making the passivation layer as thick as possible to have low capacitance/high bandwidth. One more important constraint was making a conductive layer as thin as possible for easy drilling in TEM. In order to ensure the real-estate on the chip was well used without increasing the capacitance the contact pads were designed to be at the very edge of the membrane. In addition, unlike most solid state nanopore architectures, the passivation layer is under the actual membrane to make sure the electrodes were on a flat surface. This was a requirement due to the extremely thin membrane layer. Although it had a lot more relaxed requirements for contacting the pads than the original project, it was still a daunting task to seal the membrane while having good contact. For this purpose, several cycles of membrane assembly designs and clamping schemes were implemented. Ultimately, a 3D printed assembly was able to satisfactorily seal the chip while allowing access for the probes to touch down.

The membrane topology was fabricated with success. The procedure for membrane fabrication is described in the next section. However, there was a physical road block: TEM drilling. In the experimental section, the consequences of using TEM drilling is explained.

2.1.1 Fabrication

The membranes are fabricated over a 302μm thick p-type double-side polished silicon wafer with <100> crystal orientation and $10\Omega \cdot cm$ resistivity. In order to measure the film-stress in the later stages of the process, the virgin wafer's radius of curvature is measured in Tencor Flexus Stress Measurement tool.

The wafer is deposited with a thick insulating layer to decrease capacitance. The choice of material is mixed-frequency PECVD Si_3N_4 due to its high deposition rate, low-stress and fast etch characteristics in SF_6 chemistry based bosch etch processes. Before the actual deposition, Advanced Vacuum PECVD chamber is conditioned with a 10 minute pre-coat using a mixed frequency Si_3N_4 recipe, which is essential for ensuring that the deposited film in the actual process is low-

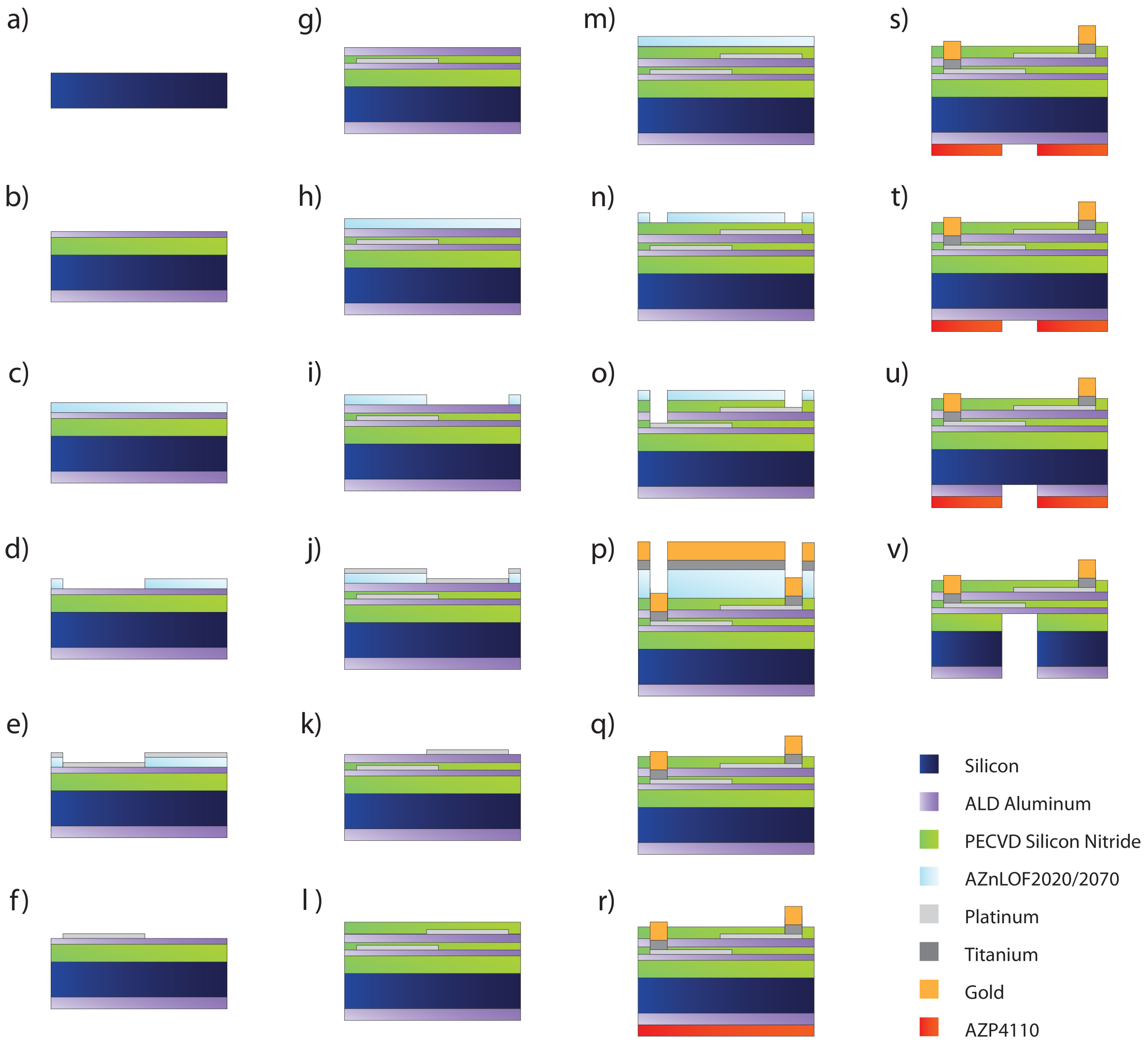

Figure 2.1: Embedded electrode nanopore fabrication steps.

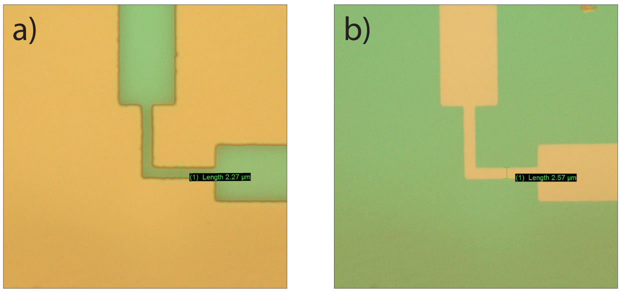

Figure 2.2: First metal electrode optical microscope images: a)Developed AZnLOF2020. negative resist. b) After Pt deposition lift-off process.

stress. Followed by the conditioning, the virgin wafer is placed in the PECVD chamber and deposited 32 minutes of Si_3N_4 using the same mixed frequency recipe on the top side of the wafer. The resulting film is measured to be $2489\mathring{A}$ thick using a Woolam M2000DI Variable Angle Spectroscopic Ellipsometer. After the deposition, the film stress on the wafer is measured with an average tensile stress of 64MPa using Tencor Flexus.

The process continues with the deposition of 94 cycles of ALD Al_2O_3 with a H_2O saturated recipe at 300°C, which resulted in a $105.6\mathring{A}$ thick film on the front side. This film provides an etch stop for DRIE process. In order to serve as a hard mask during the through etch in the final step of the process, another layer of ALD Al_2O_3 is deposited on the backside of wafer. 437 cycles of the same H_2O saturated deposition recipe resulted in a film thickness of $497.18\mathring{A}$. The final stack is shown in figure 2.1.b.

The first metal layer layer lithography begins by spinning the HMDS adhesion promoter at 6krpm for 30s on the front side of the wafer. Then, the HMDS dried using N_2 gun for 30s. The AZnLOF2020 is spread carefully over the wafer, avoiding bubbles. The negative photoresist is spun at 6krpm for 30s(2.1.c). After baking the wafer at 110°C for 75s, the wafer is aligned under the MJB MA6 contact aligner and exposed for 4.5s at $17.5\mathrm{W}\cdot\mathrm{cm}^{-2}$ using the mask pattern in fig.2.2. Immediately afterwards, the wafer is baked at 110°C for 1min. The exposed and baked patterns are developed in AZ300mif developer for 45s with minimum agitation. At the end of the development step, the wafer is thoroughly rinsed in water and N_2 dried. In order to remove photoresist residues, the wafer is ashed in O_2 plasma chamber for 30s with 100W power at 300mTorr pressure. The resulting critical features are measured to be 2.4μm, instead of 2μm. Extremely thin deposition of Pt film requires a high quality surface. Thus, the difference between the original pattern and the actual feature size is due to 10s over development and O_2 plasma ashing to ensure complete removal of photoresist from the surface(see figure 2.1.d.).

Metal deposition is performed in a custom electron beam evaporator with an easily replaceable crystal to track the deposition rate. After the chamber is pumped down to 1μTorr, a $50\mathring{A}$ thick Pt layer is evaporated with $1\mathring{A}$/min deposition rate. At the end of the process, the wafer is placed in resist stripper

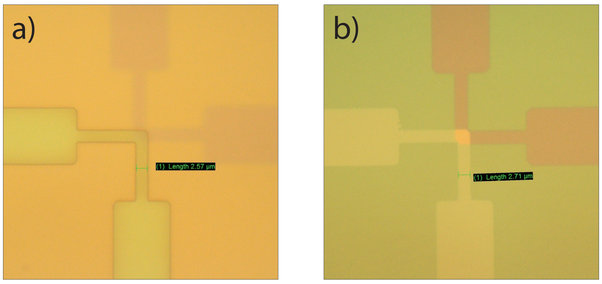

Figure 2.3: Second metal electrode optical microscope images: a)Developed AZnLOF2020. negative resist. b) After Pt deposition lift-off process.

1165 at 80°C for 30min, followed by isopropanol and deionized water(DI) rinse to lift-off the excess metal as can be seen in figure 2.2.b and figure 2.1.f.

The metal layer is passivated with 1min low-stress PECVD deposition, forming a 70.75$\mathring{A}$ film. The passivation step is continued with 188 cycles of ALD Al_2O_3 that resulted in a film of 219.1$\mathring{A}$ as in figure 2.1.g.

The second metal layer lithography is very similar to the first metal layer lithography. After spin coating the wafer front side with HMDS at 6krpm for 30s, followed by N_2 drying for 30s, the wafer is coated with AZnLOF2020 at 6krpm for 30s. After the spin process, the wafer is baked at 110°C for 75s. As the alignment process involves contact alignment of several 2x2μm features across a 4inch wafer, it can pose significant technical difficulties. After a 4.5s exposure at 17.5W$\cdot$cm^{-2} intensity using the same metal mask used in the first layer rotated 90°, the wafer is baked at 110°C for 1min. The resist is developed in AZ300mif developer for

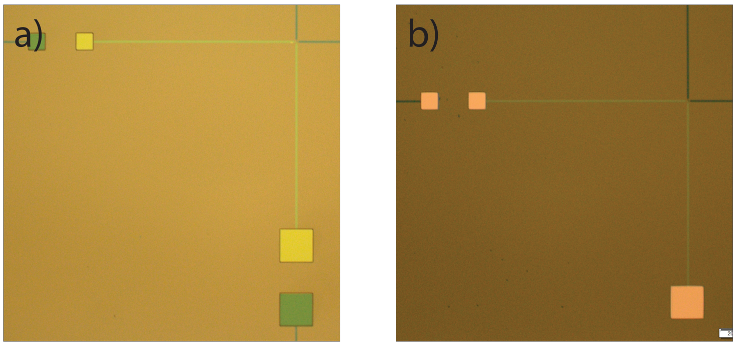

Figure 2.4: Contact pads' microscope images: a)Developed AZnLOF2070. negative resist. b) After Ti/Au deposition lift-off process.

45s. The remaining residual resist in the features are cleaned using O_2 plasma at 300mTorr at 100W for 30s.

After the lithography step, the wafer is placed in the electron beam evaporation chamber and deposited another 5nm layer of Pt. At the end of the metal deposition, the wafer is placed in 1165 at 80°C for 30min and rinsed with isopropanol and DI afterwards.The second metal layer is passivated with an additional 2min PECVD with the low-stress recipe, forming a 109.5$\mathring{A}$ thick layer(figure 2.1.k and figure 2.3.b).

In this phase of the fabrication, the wafer is ready for patterning the contact pads. In order to protect the alumina layer at the backside of the wafer from extensive exposure to AZ726mif developer, the backside of the wafer is also protected by photoresist. HMDS is spin-coated at 4krpm for 30s on the backside of the wafer, and dried with N_2. Then, AZ4110 is spun on the wafer at 4krpm for 30s and baked at 95°C for 1min. Subsequently, the wafer is turned front-side up and spin-coated with HMDS at 3.5krpm for 30s and dried with N_2 30s. The wafer is spin coated with AZnLOF2070 at 3.5krpm for 30s. While the metal layer lithography steps are meant to be as high resolution and thin as possible, contact pad lithography needs to be robust. Therefore, it is a relatively thick resist. After the coating, the wafer is baked at 110°C for 3min. Following the bake, the wafer is aligned in MJB MA-6 aligner and exposed for 15s at 17.5W$\cdot$cm^{-2} intensity. The wafer is baked at 110° for 1min. Exposed wafer is developed in AZ726mif developer for 2min30s. In order to remove the residual photoresist from the features, the wafer is placed in the O_2 plasma chamber for 1min at 300mTorr and 100W power. To remove the remaining solvent from the resist, the wafer is post-baked at 110°C for 5min.

To remove the passivation layers over the contact pads, ICP RIE and wet etch is used in conjunction. The wafer is mounted on a carrier wafer using pump oil and etched in ICP RIE chamber using CF_4/O_2 recipe with the conditions shown in table 2.1 to remove 20nm thick PECVD layer on the Al_2O_3. After the ICP RIE, the wafer is immersed in AZ300mif for 30mins to remove 20nm ALD alumina layer.

At this point, the Pt contact layers are exposed. The wafer is placed in the electron beam evaporator once more to deposit the contact pads. The chamber is

Source Power:	900W
Forward Bias:	25W
Flow Rates:	CF_4 5sccm O_2 45sccm
Pressure:	2.5Pa
Duration:	2min

Table 2.1: Panasonic ICP RIE PECVD Si_3N_4 etch conditions.

vacuumed down to 1μTorr. First Ti layer is deposited to provide good adhesion for Au and serve as a barrier layer for the probes at a rate of $0.1\mathring{A}$/s for 10nm, followed by up to $2\mathring{A}$/s until a thickness of 100nm is reached. Then, the 150nm Au layer is deposited at a rate of $2\mathring{A}$/s over the Ti layer. At the end of the deposition, the wafer is placed in 1165 for 30min at 80°C. The residual gold after the strip process is agitated using the sonication bath for 5min.

With the patterning of the contact pads, the fabrication steps on the front-side of the wafer are completed. Now, the backside of the wafer needs to be patterned and aligned to the front side structures. The backside patterning defines the membrane handle boundaries and the trench that forms the free-standing membrane. On the backside of the wafer, HMDS is spun at 4krpm for 30s and dried for 30s using N_2. Then, the wafer is spin-coated with AZP4110 at 4krpm for 30s and baked at 95°C for 1min. Using the IR microscope and illumination, the front-side features are aligned in MJB MA6 aligner. The wafer is exposed for 4s at 17.5W$\cdot$cm^{-2}. After the exposure, the wafer is developed in 4:1 AZ400K

Source:	900W
Bias:	200W
Pressure:	0.5Pa
Flow Rate:	CHF_3 40sccm
Duration:	2min

Table 2.2: Panasonic ICP RIE Al_2O_3 hard-mask patterning conditions.

	Etch A	Etch B	Deposition
Source:	825W	825W	825W
Bias:	9W	9W	0.1W
Pressure:	23mTorr	23mTorr	
Flow Rate:	C_4F_8 1sccm SF_6 100sccm AR 40sccm O_2 0sccm	C_4F_8 1sccm SF_6 200sccm AR 40sccm O_2 0sccm	C_4F_8 26.6sccm SF_6 1sccm AR 40sccm O_2 0sccm
Duration:	2s	9s	5s

Table 2.3: Plasma-Therm DRIE chamber conditions during silicon bosch etch steps.

developer for 90s. The remaining photoresist residues are removed using 1min of O_2 plasma at 300mTorr with 100W power. The patterned wafer is mounted on a carrier wafer to be placed in the ICP RIE chamber once more to etch away the alumina as in figure 2.1.u using the recipe in table 2.2.

As the patterned backside Al_2O_3 layer serves as the hard-mask for the through etch, the wafer is ready to be placed in the DRIE chamber. The wafer is mounted on a glass carrier wafer to be able to see from the other side if the silicon underneath membrane window is removed. It is etched for 4 hours at 20°C with the recipe in table 2.3. The recipe is optimized to minimize grassing in the trench.

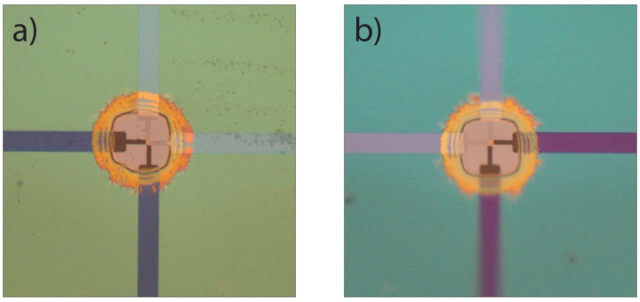

Figure 2.5: Typical membrane optical microscope images: a)Average membrane. b)Good membrane. The light colored area around the membrane is the blowout region.

After the etch, the wafer is separated in acetone from the carrier wafer. At the end of the acetone treatment, the wafer is further cleaned in DI. During this process, utmost attention is paid to making sure not to move the wafer in the normal direction to the surface in acetone or water not to damage the membranes. Due to the structure of the mask, there are many loose silicon triangles. These triangles can get stuck on the chip and when tried to be separated can damage the surface.Therefore, it is best when these triangles are removed in acetone during the carrier wafer separation process.

At the end of the fabrication, roughly 1/3 of the chips were in perfect condition, 1/3 of the chips had minor blemishes but still had functional membranes and electrodes and the rest did not have membranes or conducting electrodes. In figure 2.5, one can see the average and good membranes. The yellow halo around the membrane is the blow-out region due to DRIE. This feature is a by-product of the fabrication process; the PECVD silicon nitride etch rate is significantly slower than the silicon etch rate. While trying the punch through the silicon nitride to reveal the membrane, the trench starts to bloom at the boundary of silicon and silicon nitride interface. This topological inconvenience does not present any mechanical problems.

2.1.2 Experiments

There were a number of complications with the experimental phase of the membranes. The measurements were difficult to perform due to the design and assemby constraints of the membranes. In addition, the membranes did not perform well after being TEM drilled and immersed in the electrolyte. However, there were partial successes that could provide guidance for the next version.

The chips were designed to fit within a circle of 3mm diameter in order to allow the chip to be inspected and drilled in TEM. This required the contact pads for the electrodes to be patterned on a very small surface while allowing space for sealing the chip to the CIS and TRANS reservoirs. These design constraints made the experiment inherently difficult. The electrodes were patterned out of 5nm thick Pt layer, which was protected with a 20nm thick silicon nitride layer. In the case of a minor slip of the tweezers, the electrodes could be severed, making the membrane dysfunctional. Due to the fabrication process and design, the corners of the contact pads tended to extend free-standing out of the chip. When these corners were not treated with the necessary care, they could fold over and contact the silicon substrate, shorting the top and bottom electrodes. The contact pads were made out of a stack of 5nm Pt, 100nm Ti and 150nm Au, which may be an adequate stack for a chip with an insulating wafer handle. However, in the case of this design, if the micropositioners were not lowered with care, the probe would pierce through the contact pads, causing a short with the silicon wafer handle. This had implications during the experiment as well; a slight bump during micropipetting to the CIS chamber could make the probe needle skid across the chip, scratching the surface down to the silicon wafer. Another challenge was due to the inaccuracy of the interfacing gear, making the assembly of the chip very difficult, often resulting in an improper seal between the chip and the reservoirs. A combination of all these factors made the experimentation very challenging.

After testing 24 membranes with 4 different interfacing gears, there were partial successes. The electrodes had 10kΩ resistance and less than 10pF capacitance, resulting in a high bandwidth capable structure. The majority of the membranes did not have shorted electrodes after TEM drilling. The membranes did not show ion permeability when they were drilled far away from the electrodes. But, these successes did not translate into DNA measurements as the pores drilled through the electrodes began to show very high conductance shortly after wetting, leading to very low sensitivity to particle translocation through the pore. This phenomenon was hypothesized to be attributed to the drilling process. During the TEM E-beam sputtering, the electrode material got smeared in the pore surface, making it highly conductive. This condition is observed in a similar project by IBM as well [5].

This architecture can still prove to be instrumental in measuring several phenomena in addition to the DNA sequencing research. With functionalization of alumina layers inside the pore and integrated electrodes, the membranes can be used to measure binding properties of several different proteins to DNA and RNA molecules. With an update in the design and fabrication process, the experimental difficulties can be largely alleviated. These changes are described in detail in the "Future Work" section.

2.2 Application of Solid-State Nanopores to Sizing DNA Nanotubes

In the last decade, numerous ways of utilizing DNA′s helical complementary structure have emerged. Proof of principle structures, like boxes, pores and masking features for nano-fabrication have been designed and documented [8,35,48,56]. These structures provide an exciting paradigm for devising constructs for drug de-

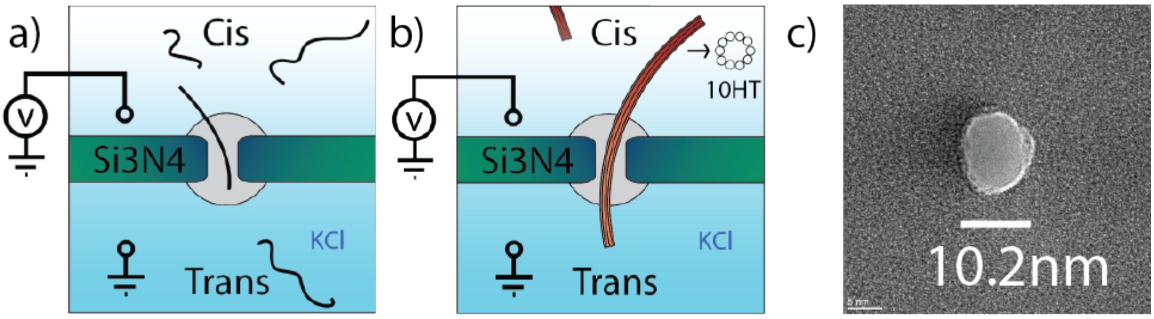

Figure 2.6: Measurement configuration. a) Cross-section of the pore with 5kbp dsDNA. b) Cartoon of a 10 Helices DNA nanotube translocation. c) TEM image of the 9.16nm effective diameter pore on 30nm thick Si_3N_4 membrane.

livery, subcellular motors and nano-manipulation capable robot arms, furthering the applications of nanotechnology.

DNA nanotubes are one of these structures that can function as interconnects in self-assembled networks and are readily amenable to metallization or surface functionalization with bio-molecules. Other potential applications of DNA nanotubes include usage as a substitute for actin filaments to magnify the motion of molecular motors with their greater durability and more versatile chemistry [71]. In order to achieve a higher yield for accomplishing these tasks, a high volume analysis method is highly desirable. Current DNA nanotube characterization methods rely on fluorescent tagging and image analysis, lacking in resolution and throughput. Atomic Force Microscopy(AFM) allows high resolution label-free detection, but is also slow to the point of being impractical for high volume characterization. Synthetic nanopores can meet this demand by translocating thousands of

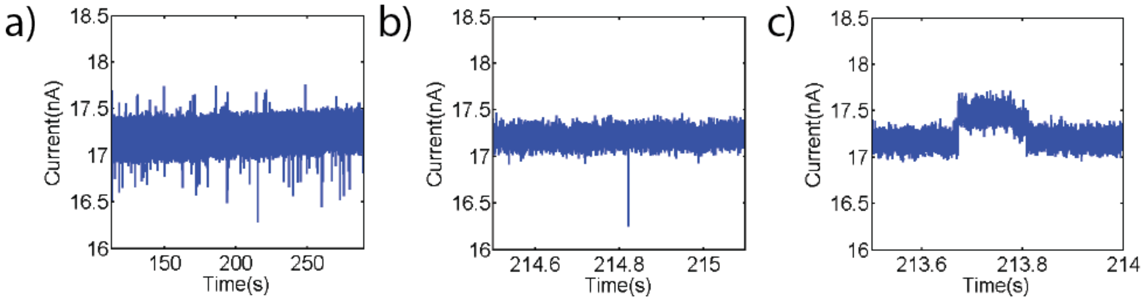

Figure 2.7: Sample current trace of DNA nanotube data with 600mV applied voltage. a) Current trace with enhancement and blockage events. b) Typical blockage event. c)Example of an enhancement event.

nanotubes per hour electrophoretically in an electrolytic environment and providing a current signature based on volume exclusion.

In this project, the feasibility of utilizing synthetic nanopores to characterize a high volume of DNA nanotubes is investigated. In figure 2.6, the cross-section of the experimentation geometry is depicted. 10-Helix DNA nanotubes(10HT) were driven through Si_3N_4 nanopores electrophoretically in 1M KCl at various voltage levels. The associated current signatures were analyzed using novel data analysis techniques and compared with those of 5kbp dsDNA. A 3D COMSOL model of the pore was simulated using the Poisson equation coupled with the Nernst-Plank equation to estimate the forces experienced by the DNA near the pore.

In addition to allowing us to evaluate the potential of using synthetic nanopores for DNA nanotube sizing, the experiments revealed a physical phenomenon never reported before. Most experiments conducted using synthetic nanopores are performed with dsDNA which produces only current blockage events at KCl concentrations above 400mM. Interestingly, the DNA nanotubes induce current enhancement events at 1M KCl electrolyte concentration. Possible mechanisms producing the enhancement events at this concentration level are discussed.(A sample current trace and examples of enhancement and blockage events are shown in figure 2.7.c.)

Finally, synthetic nanopores are evaluated for their performance in sizing DNA nanotubes, and possible improvements to the setup and experimentation are described.

2.2.1 Methods

Norcada brand 30nm thick Si_3N_4 TEM grid membranes were used in experiments. Following a 15 minutes O_2 plasma cleaning step at 100mW, a single 10nm pore was drilled in each membrane using e-beam sputtering at 300keV in a FEI Titan TEM. Then, the silicon nitride chips were immersed in an 80°C Cyantek Nano-Strip bath for 15 minutes and rinsed with copious amounts of deionized water. The chips were N_2 dried and O_2 plasma bonded with 200μm diameter opening PDMS gaskets before being assembled in a custom-made Teflon assembly. Within the teflon assembly the chip separates two reservoirs; a CIS reservoir of 80μl and a TRANS reservoir of 10ml.

Membranes were wetted by immersing the whole Teflon assembly in ethanol and placing the immersed assembly under vacuum for 20 minutes to degas the ethanol in the vicinity of the pore, dislodging nano-bubbles. Next, the pore assembly was removed from the ethanol and rinsed with Millipore 0.22μm filtered deionized water several times. Because diffusion around a nanopore can be very slow, it is important to prevent salt precipitation due to high ethanol content. Therefore, Ag/AgCl electrodes were immersed in the water-filled CIS and TRANS chambers and IV measurements were used to drive the remaining ethanol away from the pore interface. Finally, the pores were immersed in 1M KCl 20mM Tris pH7.8 solution and repeated IV measurements were taken until the pore reached the expected value of conductance. When the conductance level was within 25% of the theoretical value and the flicker noise became unnoticeable, the volume of the CIS chamber was replaced with a solution of 3nM 5kbp dsDNA 1M KCl 20mM Tris pH7.8 to take control measurements. The assembly was left to rest overnight for the DNA concentration to stabilize and reach the nanopore vicinity. Measurements were taken under 300mV, 450mV, 600mV and 750mV potential levels across the reservoirs for 30 minutes each. Mg^{2+} is a cation that is not found in most dsDNA translocation experiments; However it is an essential part of the buffer used for DNA nanotubes. Thus, the same experiment was repeated with 3nM 5kbp dsDNA 1M KCl 1xTAE 12.5mM Mg pH7.8 and confirmed that the current enhancement events seen with DNA nanotube measurements were not an artifact of the Mg^{2+} ions. The final experiment was performed with ~2nM 10HT DNA nanotubes in a solution of 1M KCl 1xTAE 12.5mM Mg pH7.8. Data acquisition was done with a Heka EPC10 potentiostat at 200kHz sampling rate with a 100kHz lowpass 8-pole Bessel filter built-in the amplifier.

Data acquisition can pose difficulties due to challenges inherent to operating a nano-scale aperture exposed to a macro scale environment. Pore wetting can be troublesome and time consuming as the wetting process can take from a couple hours to a day, requiring a certain level of experience to diagnose the root causes of problems. Furthermore, a wet pore may not always stabilize; in many instances high flicker noise is observed, ultimately necessitating discarding the membrane. Another failure mode of the experiments is produced by DNA-pore interactions which leave the pore irreversibly clogged. Given these failure modes, ~50% of the pores produce some data and roughly one quarter of the pores provide useful data.

Acquired data was analyzed using a custom threshold-based pulse detection Matlab algorithm that was capable of determining different levels in an event and analyzing the pulse characteristics within. After the raw data was 15kHz low-pass 8-pole Bessel filtered, the data was filtered again with a 20Hz moving average filter as a first step to determine the baseline. Then, the magnitudes of each point in the moving averaged data was used to form a histogram. An automated Gaussian distribution was fit on the most prominent peak, and taken to be the population of data points associated with the baseline. Data points with magnitudes more than two sigma away from the expected value of the baseline Gaussian distribution were assigned the expected value of the Gaussian distribution in the 15kHz data and the 20Hz moving average filter was reapplied. The resulting trace was used as the baseline throughout the rest of the Matlab event analysis algorithm.

Since pulses are detected based on a threshold, an accurate assignment of threshold is crucial. Ideally the threshold should be set at the minimum distance that cannot be mistaken for part of the baseline. To achieve this goal, the data points that were flattened during the baseline calculation procedure were removed from the baseline trace while calculating the standard deviation, providing a more precise value. Assuming the noise distribution around the baseline to be Gaussian, the threshold was set at four sigma throughout the pulse analysis.

All data points above threshold were considered part of events to be detected. When a data point above threshold was located, the algorithm traversed the current trace backwards until the current level dropped to baseline and recorded the associated time-stamp, marking the beginning of the event. Next, the algorithm traversed forwards until the current level dropped to baseline and recorded the time-stamp to mark the end of the event. The 15kHz lowpass filtered data be-

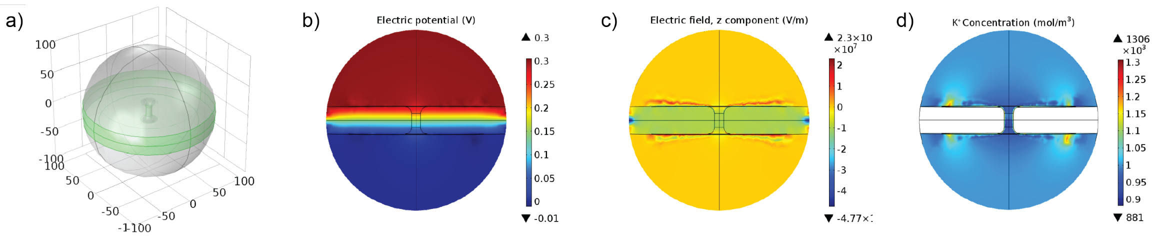

Figure 2.8: COMSOL simulation of the ionic concentrations in 9.16nm silicon nitride membrane. a) Geometry of the simulation. b) Electrical potential due to 300mV applied voltage shown over the cross-section. c) Electric field. d) Potassium concentration.

tween the start and end time-stamps of an event were analyzed for the maximum blockage level, event duration, total charge and current levels. If the event duration was longer than 2.5ms, the pulse analysis function was called recursively with the data points associated with the event as its input in order to analyze nested events.

2.2.2 COMSOL Simulation

COMSOL Multiphysics is a simulation software capable of calculating complex physical phenomena with a user-friendly interface. The program allows users to create and define simulation geometries and their boundary conditions within a versatile CAD environment. In addition to static problems, COMSOL is able to handle transient problems that alter the simulation topography(see Chapter 3). The accessibility and the depth of COMSOL Multiphysics make it an invaluable tool for investigating difficult problems such as conductance characteristics in a synthetic nanopore with surface charge.

The goal of our simulation is to evaluate the possibility of DNA nanotube disintegration inside and vicinity of the pore due to the forces induced by the E-field. A spherical geometry is preferred for capturing the symmetry in the zone of interest. Diffusion coefficients for potassium and chlorine ions and the surface charge density of Si_3N_4 for pH7.8 were taken from the literature [41, 79]. Ion concentrations, potential and E-field across the pore were computed, allowing the calculation of the force experienced by the DNA nanotube.

For this purpose, a sphere of 100nm radius was divided in half by a 30nm thick barrier, representing the silicon nitride membrane. A pore in the center of the barrier had a cylindrical cross-section with rounded corners. The surface of the barrier was assigned -0.020C/m^2 surface charge density within a radius of 75nm. Ideally the whole silicon nitride interface should be assigned a surface charge density but doing so causes conflicting boundary conditions at the edges of the geometry. The Nernst-Plank equation and the Poisson equation were solved simultaneously utilizing the "Electrostatic" and "Transport of Diluted Species" modules. The diffusion coefficient used for the potassium ion was 1.957x$10^{-9}\mathrm{m}^2/s$, while that used for the chlorine ion was 2.032x$10^{-9}\mathrm{m}^2/s$ [79]. The potassium concentration and the related electric field produce some irregularity at the boundary of the surface charge on the barrier(figure 2.8). This condition had no distinguishable effect in the conduction of the pore. As far as the local conditions around the pore are concerned, the surface is fully charged.

The simulation pore had an impedance of 26 MΩ. The actual pore impedance decreased in the course of the experiment from 43MΩ to 32MΩ. This discrepancy can be explained in part by the fact that 1M KCl solution is a high enough concentration to invalidate some of the assumptions made by "Transport of Diluted Species" module in COMSOL. Based on the model, the maximum E-field sustained in the pore is 9.98x10^6 V/m. This value drops to 10^6 V/m at the edges of the access resistance hemisphere. The simulation of the E-field formed in the channel provided the basis for calculating the maximum force applied to the DNA nanotubes.

2.2.3 Data Analysis

In this section, experiment data for 5kbp dsDNA and 10HT DNA are presented. Theoretical calculations for pore conductance and blockage ratios for the experiments are evaluated. Specifically, the possible physical mechanisms that produce the current enhancement and blockage events are discussed. The fact that enhancement events are observed reproducibly uniquely in the presence of DNA nanotubes is especially significant because dsDNA is widely reported in the

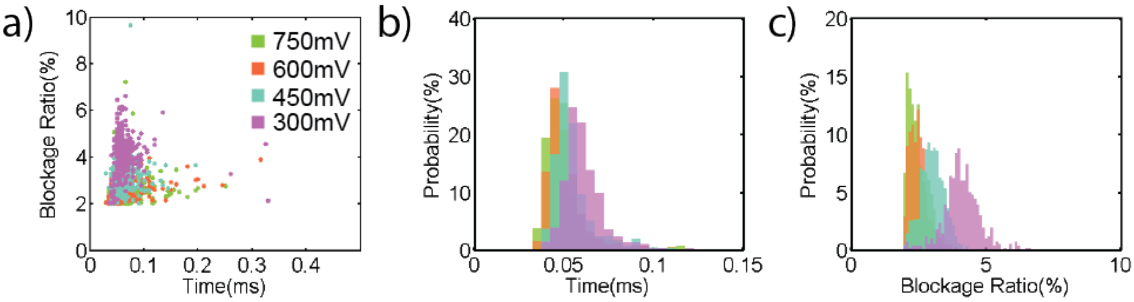

Figure 2.9: 5kbp dsDNA in buffer solution with Mg^{2+} measurement results are in line with typical default buffer experiments. There are no enhancement events as expected. a) Scatter plot of events due to 300mV, 450mV, 600mV and 750mV. b) Event blockage ratio histogram. c) Pulse duration histogram.

literature to produce only blockage events under similar conditions. Enhancement events are absent in our control measurements as well.

Data presented in this section were taken using a pore with a major axis of 10.2nm and a minor axis of 8nm diameter, corresponding to an effective diameter of 9.16nm. During the calculation of the pore impedance, a cylindrical pore model that takes into account the access resistance was preferred over a hyperboloid model [55]. The TEM used for drilling the pore was an FEI microscope, as opposed to the more commonly used JEOL 2010F. During the drilling process, the pore was punctured with a rough diameter of 4nm and then expanded by focusing on the edges. This was possible due to the narrower beam angle that hits the membrane compared to Jeol microscopes, leading to a steeper pore wall as opposed to an hourglass shape in the center section of the pore. The cylindrical pore model describes the pore conductance better than the hyperboloid model in the nanopore size regime used in this project, as confirmed by the model results(although in smaller pores drilled with FEI TEM, the hyperboloid model was more accurate). The pore model used to calculate the theoretical pore conductance was:

$$G_{open\ pore} = \left(\underbrace{\frac{4}{\pi}\frac{L_{pore}}{d^2}}_{\text{Geometric Term}} + \underbrace{\frac{1}{d}}_{\text{Access Resistance}} \right)^{-1} \underbrace{(\mu_K + \mu_{Cl}) n_{KCl}\, e}_{\text{Solution Conductivity}} + \underbrace{\frac{\mu_K\ \pi d \sigma}{L_{pore}}}_{\text{Electroosmotic Term}} \tag{2.1}$$

where μ_K and μ_{Cl} stand for electrophoretic mobility of potassium and chlorine ions with the values 7.691 x $10^{-8}\text{m}^2/Vs$ and 7.909 x $10^{-8}\text{m}^2/Vs$, respectively [83], d and L_{pore} are the diameter and length of the pore, σ is surface charge density in the pore, and n_{KCl} is the electrolyte concentration per unit volume. The first term is a simple conductance calculation based on pore geometry and solution conductivity with an additional term for the access resistance of the pore. The second part accounts for charge mobility along the surface of the pore. In Golovchenko's work [41](at the pH condition used here) the surface charge density is measured and calculated to be about -0.020C/m^2. This surface charge is screened by an extra layer of potassium ions, which can contribute to the conduction. During a

DNA translocation event, the change in pore conductance is:

$$
\begin{aligned}
\Delta G &= G_{with\ DNA} - G_{open\ pore} \\
&= \left[\left(\frac{4}{\pi} \frac{L_{pore}}{d_{eff}^2} + \frac{1}{d_{eff}} \right)^{-1} - \left(\frac{4}{\pi} \frac{L_{pore}}{d^2} + \frac{1}{d} \right)^{-1} \right] \cdot (\mu_K + \mu_{Cl}) n_{KCl}\, e + \frac{\mu_K^* \, q_{l,DNA}^*}{L_{pore}}
\end{aligned}
\tag{2.2}
$$

where the effective diameter, d_{eff} corresponds to:

$$d_{eff} = \sqrt{d^2 - d_{DNA}^2} \tag{2.3}$$

The first portion of the equation accounts for the conductance change due to the charge excluded by the presence of the DNA molecule. On the other hand, the second portion describes the extra charge brought by the DNA to the pore, again contributing in a positive way to the conductance of the pore. (Note that negative ΔG denotes a blockage event.) These equations are an amalgam of equations put forth individually by Kowalczyk, Smeets and Wanunu [55, 83, 97]. Each author ignored a portion of the equation as the term became negligible for their purposes. Since the DNA nanotubes induce enhancement events, it is crucial to account for all aspects of the conductance in a pore to have a better understanding.

Using equation 2.1, the expected impedance of our nanopore was calculated to be 35.7MΩ, matching very close to the average actual measurement of 35.29MΩ. The electrolyte conditions required for DNA nanotube assembly require a Mg rich buffer which was a variable that needed to be confirmed to have no effect on

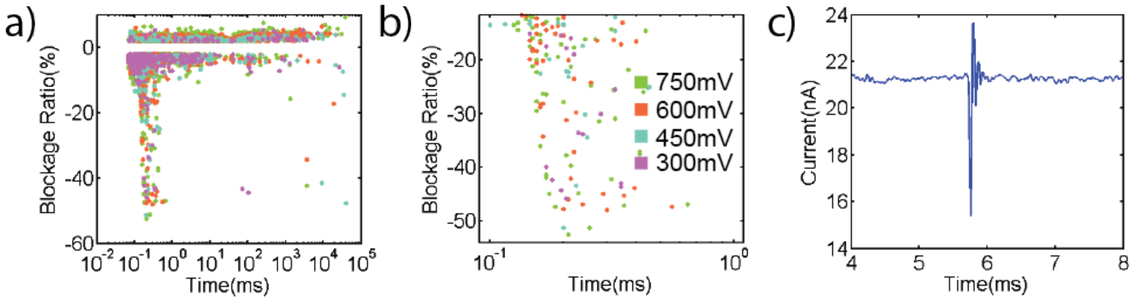

Figure 2.10: 10 Helices DNA nanotube data. There are low level long duration enhancements events, and a mix of short and long duration blockage events a) Scatter plot of events in terms of current change percentage and duration. b) Events associated with the intact DNA nanotube translocation. c) Sample event for a DNA nanotube translocation. The ringing after the event is an artifact of the capacitive feedback potentiostat headstage.

the DNA translocation characteristics. 5kbp dsDNA measurements were taken in Mg rich and regular buffer solutions and compared. These measurements showed no discernible difference, confirming that any effect Mg has on the translocation mechanism was negligible. This was especially significant since cations like Mg^{2+} are known to bind DNA helices. The charge deficit associated with dsDNA translocationsin the presence of 12mM Mg were in agreement with the reported values in the literature, confirming the validity of our measurements. In a translocation event through this nanopore, dsDNA is calculated to induce a current blockage percentage of 2.84%. Thus, the theoretical blockage ratio for dsDNA matches with the measurement results pretty well, as can be seen in figure 2.9.b.

When compared to dsDNA, 10HT DNA nanotubes produce very high blockage ratios with significantly longer durations. The theoretical blockage percentage associated with a DNA nanotube longer than 50nm is 30.7% based on equation 2.2. However, as can be seen in the scatter plot in figure 2.10, such large events constitute a small percentage of all the events.

The E-field that extends outside the pore entry is the sole way of aligning a charged polymer with the pore axis. Considering that this field is intense only within a diameter of the pore, it is understandable to see few intact events from a macro molecule that can extend for micrometers with longer than 4μm persistence length. Therefore it can be hypothesized that the DNA tubes that do not arrive the capture radius with an acceptable alignment can only translocate by disintegrating at the vicinity of the pore. According to COMSOL simualtions, the pore is able to exert a maximum force of over 4630pN(300mV applied voltage calculation), much higher than the snapping threshold of 600pN for DNA nanotubes with 10 helices based on Hariadis work [40]. This explains why majority of the blockage events have low blockage ratios. The percent blockage of events ranges between 1.75% to 20% with increasingly lower probability. We suspect such small events result from translocation of sub-tubular fragments.

The DNA nanotube length can be deduced from the event charge deficit(ECD)(integral of ΔI) induced. 5kbp dsDNA produce ~100+/-12.5ke charge deficit in the experimented nanopore. This value agrees well with similar studies in the literature [33, 65]. Given an effective charge per basepair of 0.53e, the ECD induced

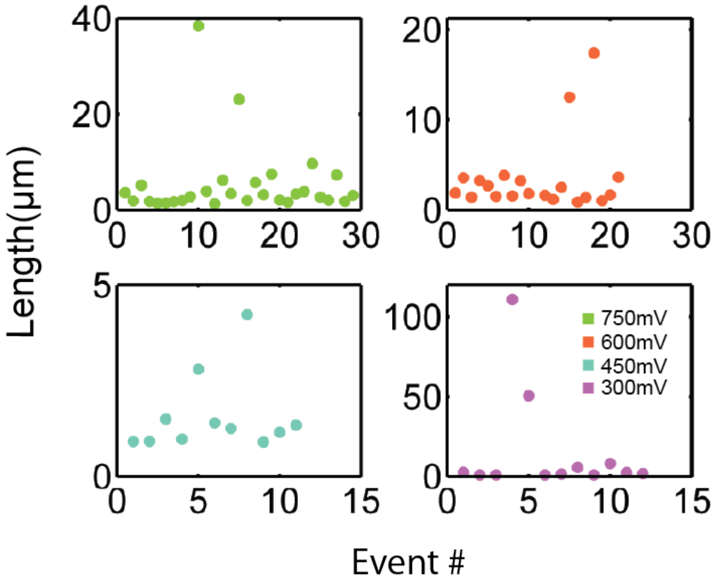

Figure 2.11: 10HT DNA nanotube lengths in micrometers for various applied voltage levels.

per effective DNA charge,γ is 0.0265. We use this as a reference for analyzing the charge deficit induced by the DNA nanotube translocation events. Figure 2.11 shows the DNA nanotube length for each event observed at different applied voltage levels. This approach assumes the electrophoretic mobility of both the dsDNA and 10HT in the nanopore are equal. Another assumption is that the DNA nanotube translocation occurs without pore/DNA interaction, In our experiments, the nanopore size was very close to the DNA nanotube diameter, which greatly increases the probability of pore/nanotube interaction, which would result in a longer dwell time. The results presented in this figure are preliminary findings,

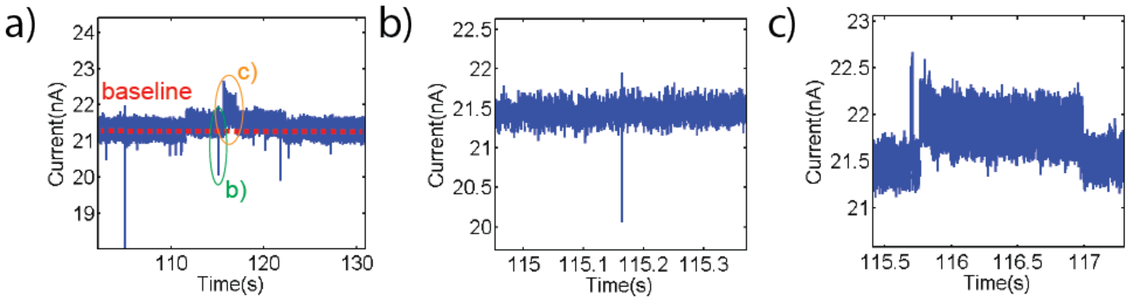

Figure 2.12: 10 Helices DNA nanotube sample enhancement events. There are nested events within enhancement events, indicating that DNA nanotube presence does not block the pore entry. a) A long duration enhancement event with nested events. b)A nested blockage event. c) An example of nested enhancement event.

requiring further experimentation and higher number of events to establish the validity of this approach.

There is one more group of intriguing events produced in the presence of DNA nanotubes. According to the equations and experiments derived in Smeets work [83], above 400mM KCl concentration DNA translocations produce current blockage events rather than enhancements. However, in the DNA nanotube data, enhancement events are observed at 1M KCl. Furthermore, they can contain nested events, meaning events within events. This indicates that the changed conditions around the pore do not prohibit DNA translocation events. In order to explain this phenomenon, the mechanis of pore conductance need to be revisited. The most basic condition required for a current enhancement event is an increased density of charges in the ambient electrolyte concentration. The access resistance can be calculated by integrating the resistance from the circular opening of the pore to a hemisphere at infinity. We would like to calculate the effect on the access resistance when a DNA nanotube occupies a hollow cylindrical space from the edge of the pore to infinity. If the DNA nanotube is immobilized on the surface, it can increase the surface charge density. If the DNA nanotube's axis lies parallel to the E-field (radial to the pore), the contribution of local mobile counter ion due to the DNA molecule would be the bare charge per base pair, 2e(figure 2.13.a).

Next, the equation governing the pore conductance is broken down to individual components. If the equation 2.1 is written in terms of resistance and neglecting the electroosmosis, it will be:

$$R_{open\ pore} = \underbrace{\frac{\rho_{KCl} \cdot L_{pore}}{\pi r^2}}_{\text{Cylindrical Pore Resistance}} + \underbrace{\frac{\rho_{KCl}}{4r}}_{\text{Top Access Resistance}} + \underbrace{\frac{\rho_{KCl}}{4r}}_{\text{Bottom Access Resistance}} \tag{2.4}$$

where ρ_{KCl} is the KCl resistivity and r is the radius of the pore. Hill derived the first approximation for the access resistance by the integral from a hemisphere with the same diameter as the pore to a hemisphere at infinity. This equation did not take in to account the resistance associated with the hemisphere. A correction to this equation was done by Hall, which resulted in the access resistance equation in use today. A dsDNA strand that extends radially to infinity from the edge of the pore would change the portion of the access resistance derived by Hill. A

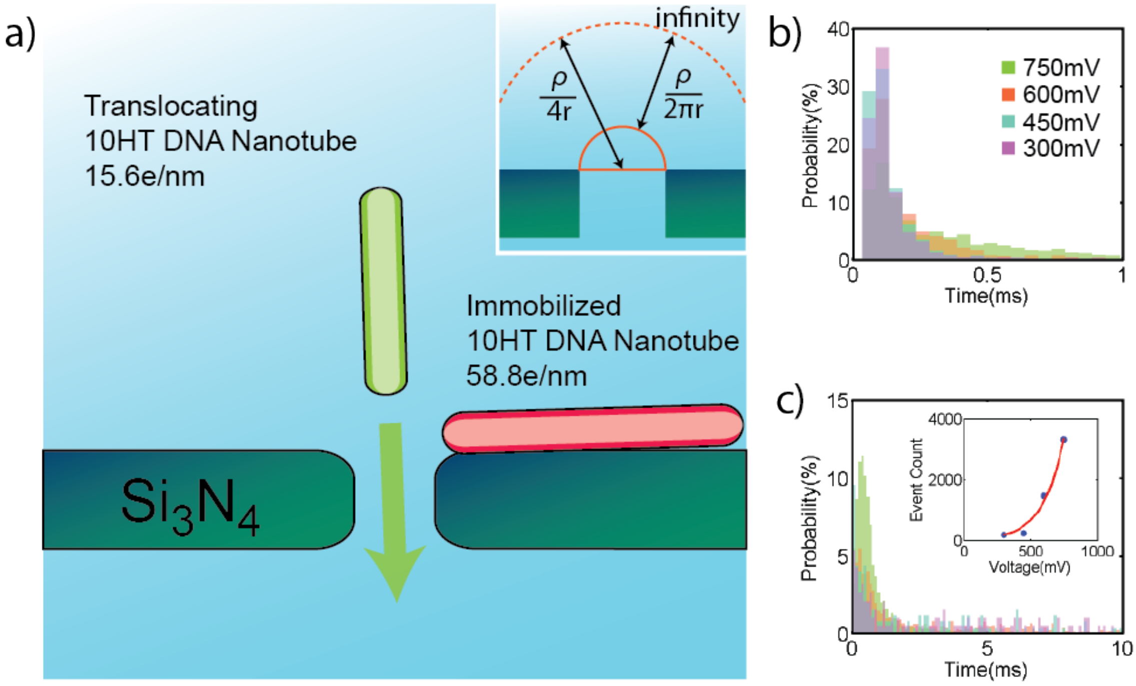

Figure 2.13: Schematic of DNA nanotube entry into the pore. a) Mobile charge difference introduced by free to move DNA nanotubes and immobilized DNA nanotubes around the pore.Inset: Showing the resistance formulas for inner and outer hemispheres around a cylindrical pore.b) Blockage events duration histogram. Blockage events occur at a faster time scale. c) Enhancement events duration histogram. Inset: Event counts increase exponentially as a function of voltage.

breakdown of access resistance on one side of the pore can be written as such:

$$R_{access} = \frac{\rho_{KCl}}{4r} = \underbrace{\frac{\rho_{KCl}\,(\pi - 2)}{4\,\pi\,r}}_{\text{Inner Hemisphere}} + \underbrace{\frac{\rho_{KCl}}{2\,\pi\,r}}_{\text{Outer Hemisphere}} \tag{2.5}$$

The mobile charge contribution of the dsDNA diminishes as a percentage of the mobile charges participating in conduction as the distance from the pore increases. Therefore, the outer hemisphere portion of the equation needs to be re-derived with a resistivity, ρ that changes with distance from the pore. The number of charges participating in conduction, n is described as a function of radial distance, r with the following equation:

$$n(r)\;dV = dn$$

$$n(r) \cdot (2\,\pi\,r^2 - A_{10HT})dr = n_{KCl} \cdot (2\,\pi\,r^2 - A_{10HT})\;dr + \lambda dr$$

$$n(r) = \left(n_{KCl} + \frac{\lambda}{(2\,\pi\,r^2 - A_{10HT})}\right) \tag{2.6}$$

where λ stands for the number of counter-ions brought by the DNA nanotube per unit length and A_{10HT} is defined by the area of a cross-section of DNA nanotube. This corresponds to a λ of 5.58x10^{10}/m. It is also important to note that of the excess ions introduced by 10HT nanotube, only the potassium ions can participate in conduction, while in bulk KCl both the potassium and the chlorine ions can participate. This situation is accounted by assigning different mobility,μ for λ and

KCl in the below equation:

$$\rho(r) = \frac{1}{n(r)\mu q} = \frac{1}{n_{KCl}\;(\mu_K + \mu_{Cl})\;q + \dfrac{\lambda}{(2\;\pi\;r^2 - A_{10HT})}\mu_K^*\;q} \tag{2.7}$$

μ_K^* is the effective electrophoretic mobility of the potassium ions on the DNA nanotube. Integrating this resistivity from a hemisphere with the diameter of the pore to the infinity, we find the total access resistance associated with the outer hemisphere.

$$\begin{aligned} R_{w\;10HT\;DNA} &= \int_{r_{pore}}^{\infty} \frac{\rho(r)}{(2\;\pi\;r^2 - A_{10HT})} dr \\ &= \int_{r_{pore}}^{\infty} \frac{1}{n_{KCl}\;(\mu_K + \mu_{Cl})\;(2\;\pi\;r^2 - A_{10HT})\;q + \lambda\;\mu_K^*\;q} \\ &= \frac{\dfrac{\pi}{2} - tan^{-1}\left(r_{pore}\sqrt{\dfrac{2\;\pi\;n_{KCl}\;(\mu_K + \mu_{Cl})}{\lambda\mu_K^*\; - A_{10HT}\;n_{KCl}\;(\mu_K + \mu_{Cl})}}\right)}{\sqrt{2\;\pi\;n_{KCl}\;(\mu_K + \mu_{Cl})(\lambda\mu_K^*\; - A_{10HT}\;n_{KCl}\;(\mu_K + \mu_{Cl}))\;q^2}} \end{aligned} \tag{2.8}$$

Assuming $mu_K^* = mu_K$, the predicted decrease in resistance correspond to only 0.15% enhancement in conduction. On the other hand, the average enhancement event is about 2.3%. Thus, there is another factor, affecting the conduction; the electrophoretic mobility.

This discrepancy can be resolved by analyzing the data presented in an article from the Keyser Group [8], where the authors investigate the insertion characteristics of a DNA origami nanopore inside a solid-state nanopore. Given the pore

Applied Voltage	Average Enhancement Event Ratio(%)	Total Enhancement Event Count
750mV	2.24	3326
600mV	2.28	1464
450mV	2.35	252
300mV	2.15	188

Table 2.4: Enhancement event ratios and counts as a function of applied voltage.

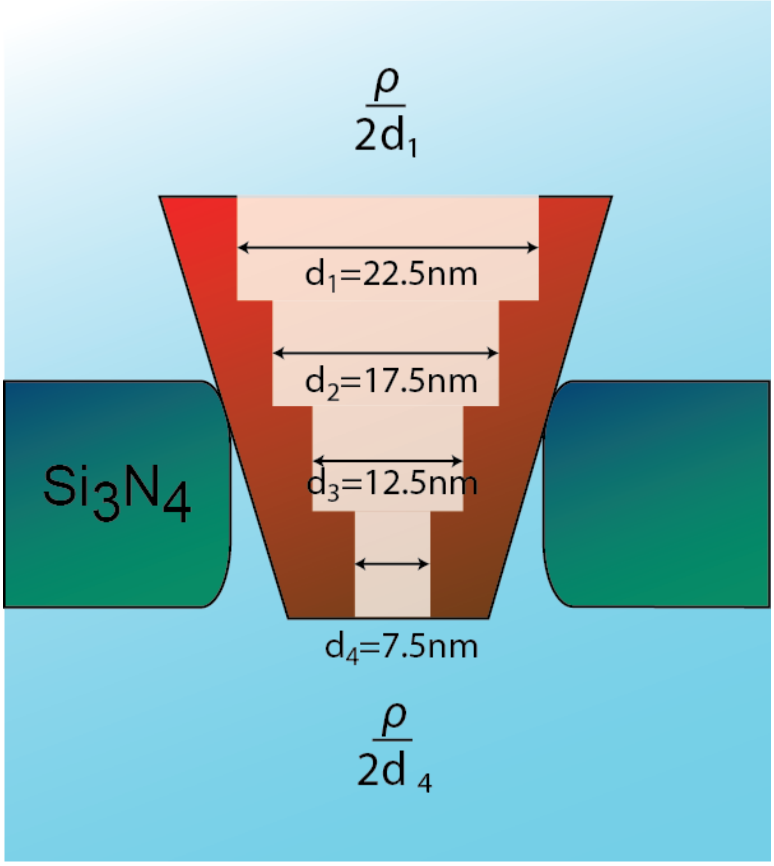

Figure 2.14: Schematic of DNA origami nanopore described in Bell et al article [8]. The resistance of the pore is calculated by adding the resistances of 4 12.85nm long cylindrical pores with varying diameters. The access resistance for each side of the pore is computed according to the appropriate diameter.

geometry formed by the DNA origami pore and the surface charge density based on 2e per basepair of dsDNA, the expected resistance is 54MΩ(see figure 2.14) but the figures presented show a resistance of 9.8MΩ. According to our calculations, the effective electrophoretic mobility for potassium, μ_K^* inside a pore constructed out of DNA needs to be ∼16.3 times the bulk value to yield the reported resistance. That is because electroosmotic velocity of the potassium ions at the surface of the DNA is a lot higher than the bulk KCl. When this condition is invoked in our experiment, the enhancement due to a DNA nanotube extending to infinity would be 3.2%, which is in agreement with our measurements as well, for all applied voltage levels(see table 2.4). Moreover, the extended duration of enhancement events versus the blockage events supports the idea of an immobilized DNA nanotube,because such a binding event would have a longer lasting effect on the current(see figure 2.13 b and c). In addition, the exponential voltage dependence of the event counts, shown in figure 2.13.c inset, leads to the hypothesis that the higher voltages are more likely to break the DNA nanotubes and cause them to immobilize around the pore. This explanation for the current enhancement events are a first order approximation that corresponds to the data remarkably well.

Characteristics of current enhancement and blockage events were discussed after a description of the pore blockage physics were described. According to the data, only a small number of DNA nanotube events constitute an unobstructed translocation event of an intact nanotube. The rest of the events were interpreted as due to smaller DNA segments and immobilized DNA nanotube / pore interactions. After an evaluation of the results in the next section, a brief summary of improvements to achieve sizing of DNA nanotubes is laid-out.

2.2.4 Outlook

The small yield in DNA nanotube translocations requires an improvement in the experimental conditions, which will be discussed in Chapter 4. Events that are produced in the presence of DNA nanotube structures yielded an interesting phenomenon never reported before. The characteristics of these events were documented and investigated.

In order to improve the conditions in a nanopore, a bigger pore with lower molarity needs to be used. Good candidate sizes for this would be 30nm diameter pore in 10mM KCl concentration. The goal is to increase the radius of the E-field extending from the pore to allow DNA nanotubes to better align with the pore axis. Furthermore, the applied voltage needs to be decreased to the range of 100mV to decrease the possiblity of disintegrating the DNA nanotubes inside the pore. Another possibility is to use a nano-channel with embedded electrodes to confine the entry of the channel, causing the E-field to extend for hundreds of nanometers. The embedded electrodes can be used to make 4 point probe measurements.

According to our analysis, silicon nitride pores could be used to translocate DNA nanotubes but precise sizing of them requires different experimental conditions and geometry. During this project, besides exploring the feasibility of using nanopores for DNA nanotube detection, a new physical phenomena was observed and explained.

Chapter 3

Circulating Tumor Cell Detection

Circulating Tumor Cells(CTCs) have recently emerged as indicators of cancer metastasis [2]. Thus, efficient detection of CTCs can provide non-invasive biopsy, enable personalized medicine and help understand cancer biology. Currently used immunoassay based CTC detection techniques are inefficient and insufficient to classify extremely heterogeneous CTCs such as Circulating Melanoma Cells(CMCs). Cancer cells have markedly different physical attributes, such as size and stiffness, and can be used to distinguish tumor cells from normal cells [24, 25, 88, 89, 100]. In this chapter, we report a micro-fluidic chip potentially meeting the urgent need to detect individual CTCs in a label-free, fast and inexpensive fashion while maintaining cell viability. The chip uses resistive pulse technique coupled with controlled pressure gradients to measure size and stiffness of cells without subjecting cells to large shearing forces. We present the design, fabrication and modeling of microfluidic channels enabling the classification of CTCs based on their size and stiffness. Using coupled Nernst-Planck and Navier-Stokes models in COMSOL subtle features in the current profile are corroborated with the size, angle of entry and stiffness. The insight provided by careful modeling of these devices enables accurate classification and clustering, which would not otherwise be possible. Validity of the modeling was proved by sizing commercial available 10μm polystyrene particles and matched results obtained by optical microscopy analysis. The device was used to classify melanoma(MNT1) and breast cancer(MCF7) cells both with and without blood cells. Results show the interference due to the presence of blood cells is minimal demonstrating the reliability of the device in detecting CTCs from a blood sample.

3.1 Measuring Deformation

Specialized Coulter Counters can be great candidates for measuring the mechanical properties of tumor cells. We propose to use a channel with controlled pressure gradients that can flex the cells repeatedly while being traversed. This system can exploit the current signature differences associated with polar-to-equatorial axis ratios to determine the deformation of the cell [37]. As in figure 3.1.a, the channel will have 5 zones with two different cross-sections. The

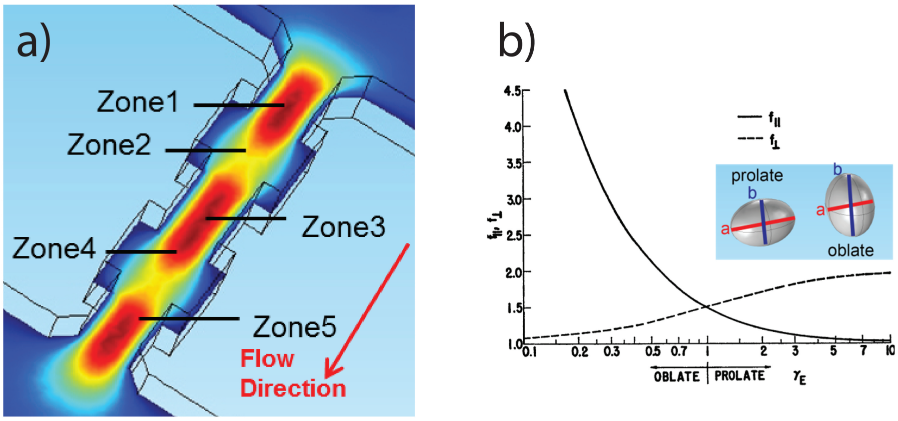

Figure 3.1: a)Undulating channel to set pressure gradients for flexing cells. b) Electrical shape factor increases as the spheroid becomes more oblate [37]. The inset gives the definition of oblate and prolate spheroids.

pressure difference between the narrow and wider zones cause pressure gradients, resulting in deformation of the cells during translocation. In order to understand the mechanics of electrical signals produced by the cell translocation, a detailed study of basic Coulter Counter equation is crucial. The main factors that affect the signal can be summarized with polar-to-equatorial axis ratio, cell size and cell entry axis to the channel. Like all Coulter Counters the fundamental equation is:

$$\frac{\Delta R}{R} = f \cdot \frac{v}{V} \tag{3.1}$$

Simply put, the ratio of the change in resistance, ΔR to total resistance,R is proportional to the ratio of the particle volume,v to the volume of the constriction that the particle traverses across,V by an electrical shape factor f.

Maxwell proved that a small non-conductive sphere in a conductive channel gave rise to an electrical shape factor of 3/2 [63]. However, this value is only true for a special case of the electrical shape factor. Indeed f is a nonlinear function governed by spheroid size to channel ratio and spheroid axial ratios [37, 84]. Therefore, the task of determining the size of any particle in a non-uniform channel based on an electrical signal is non-trivial. The electrical shape factor can be separated into two parts:

$$f = f_s \cdot f_x \tag{3.2}$$

where f_s stands for the electrical shape factor due to the actual shape of the object determined by the ratio of the polar-to-equatorial axis. The other element, f_x describes the portion associated with the increase in resistance induced by increasing ratio of the cross-section of the particle to the channel.

There are many studies that aim to provide an analytical equation to describe the electrical shape factor as a function of the cell size [27, 28, 39, 63, 77, 84, 85]. Qin et al report [76] that Smythe's equation provides the most accurate solution compared to the COMSOL simulation of Maxwell's equations in a channel. It has also been used by many prominent investigations in the field [46, 47, 102]. Smythe derived that for an intermediate size sphere in a channel [84, 85]:

$$\frac{\Delta R}{R} = \frac{d^3}{(D^2 L)} \cdot \left(\frac{1}{1 - 0.8(\frac{d}{D})} \right)^3 \tag{3.3}$$

where d is the diameter of the sphere, D is the cross-sectional diameter of the tube -considering that the channel is a simple cylinder- and L is the length of the tube. If this equation is separated in to f_s and f_x format and volume ratios as in the equation 3.1, it becomes:

$$\frac{\Delta R}{R} = \frac{3}{2} \cdot \left(\frac{1}{1 - 0.8(\frac{d}{D})} \right)^3 \cdot \frac{v}{V} \tag{3.4}$$

where $f_s = \frac{3}{2}$ and $f_x = \left(\frac{1}{1 - 0.8(\frac{d}{D})} \right)^3$. A quick analysis reveals that the f_x portion of the equation is a multiplier for the small sphere limit. This feature of the electrical signal can be used to determine the size of the particle very precisely.

In the case of the CTC detection chip, the cells often assume prolate and oblate geometries rather than a perfect sphere shape during the translocation. Sausage like shapes have longer polar axes, a and are examples of prolate objects. Conversely, earth is an example of an oblate object due to its more pronounced equatorial axis, the quantity of which is denoted by b in the figure 3.1.b inset. f_s component of the electrical shape factor was extensively investigated by Golibersuch. In his work, he also takes into account the probability of non-parallel orientation of the cell's polar axis to the flow direction [37].

$$f_s = f_\perp + (f_\parallel - f_\perp)\ cos^2\alpha \tag{3.5}$$

where $f_\perp$ stands for the perpendicular component of the f_s to the flow direction, while $f_\parallel$ represents the parallel component. These values are defined as:

$$f_\parallel = \frac{1}{1 - n_\parallel} \quad \text{and} f_\perp = \frac{1}{1 - n_\perp} \tag{3.6}$$

with a relation of

$$n_\parallel + 2\ n_\perp = 1 \tag{3.7}$$

The values of $n_\perp$ and $n_\parallel$ are widely documented demagnetization factors divided by 4π[references]. The relation between the quantities of polar and equatorial axis and demagnetization factors are as follows:

$$n_\perp = \frac{1}{m^2 - 1} \left(\frac{m}{\sqrt{m^2 - 1}}\ ln(m + \sqrt{m^2 - 1}) - 1 \right) \tag{3.8}$$

for a prolate spheroid(m>1) and

$$n_\perp = \frac{1}{1 - m^2} \left(\frac{m}{\sqrt{1 - m^2}}\ cos^{-1}(m) \right) \tag{3.9}$$

for an oblate spheroid(m<1) where $m = a/b$. Fortunately, based on Spohr's work the equations for f_s can be significantly simplified since we can assume that the translocation under pressure would cause the cells' polar axes to line up with the fluid flow direction [86, Page 186-187]. In that case, the f_s would reduce to:

$$f_s = f_\parallel = \frac{1}{2\ n_\perp} \tag{3.10}$$

As m goes lower, it defines a more oblate spheroid that forms a wider surface orthogonal to current flow, leading to a higher blockage level. On the other hand, as m goes higher, the spheroid becomes more prolate and more conformal to the current flow direction, resulting in an electrical shape factor assymptotically approaching to 1. If f_s is resolved as a result of data analysis, it can be used to determine the deformation of the cell for a given set of conditions.

In addition to the electrical shape factor, the entry axis of the cell plays an important role in the magnitude of the electrical signal. One can think of the electrical shape factor as a result of the density of E-field around a non-conductive object in a conductor. The field lines need to curve around the object to maintain continuity. This leads to a lower density of field lines in the front and back of the object. Now, if the object is placed to the edge of the conductive channel, the area that the E-field lines are distorted expands, leading to an even lower density of E-field lines in comparison to an object in the middle of the channel. In a channel, this situation is expressed as [78]:

$$\Delta R = \Delta R_0 \left[1 + \alpha \left(\frac{xd^3}{D}\right)\right] \tag{3.11}$$

In this equation, α is an empirical constant that varies between 3.5 and 7.4, while x defines how off-center a particle is. The relation between x and the distance of spheroid center to center axis is given by:

$$x = \frac{2b}{D} \tag{3.12}$$

where b is the distance of the cell center to the channel center. Ultimately, to size a cell, the off-axis effect on the current signature needs to be canceled out. Omar Saleh reported[references] that this is possible for systems with pressure driven flow where the center of the channel has higher flow rate than the edges due to the no-slip boundary condition. In such a case, the translocation duration can be correlated with how off-axis the particle is with the following equation formulated by Berge et al [9]:

$$\tau = \frac{\tau_0}{(1 - x^2)(c_1 - c_2 x^5)} \tag{3.13}$$

τ_0 stands for the on-axis translocation time for a particle through a channel and it is defined as $\tau_0 = 16\eta(L/D)^2/\Delta P$. In this equation, η is viscosity of the fluid, ΔP is the pressure drop across the channel and L is the length of the channel. In equation 3.13, c_1 and c_2 are formulized as $c_1 = 1 - (2/3)(d/D)^2$ and $c_2 = 23.36(1 - c_1)$. One can potentially exploit the relation between the translocation time and ΔR to evaluate ΔR_0 and accurately size a spheroid.

Electrical signals associated with cell translocation through a Coulter Counter have unique properties. The cell axis ratio and size dependent current signatures can be exploited to measure mechanical properties, such as deformation and size. Utilizing the equations explained in this section, we can devise a chip that can

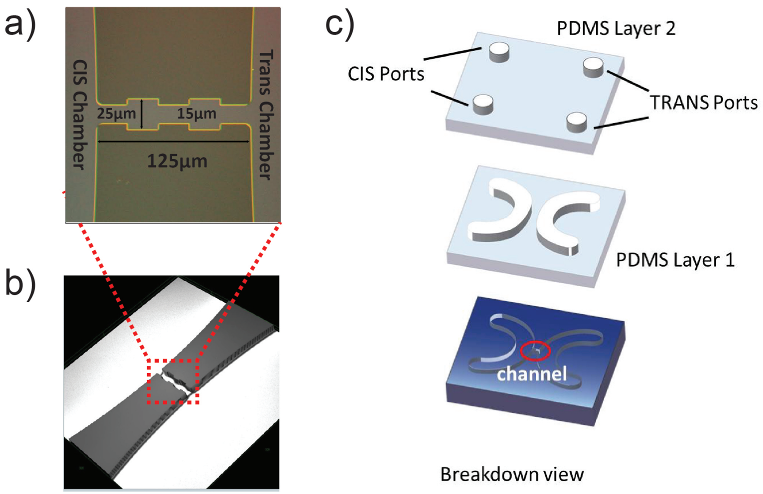

Figure 3.2: a) Optical microscope image of the channel lithography. b) 3D rendering of the confocal microscope image. c)Breakdown view of the chip design.

perform flow focusing and repeated measurements to achieve the goal of circulating tumor cell detection. In the next section, the design of such a device is discussed.

3.2 Design

The design of the device was determined by compatibility with mass production, experimental requirements and measurement instruments. The measurement system used was a trans-impedance amplifier with a very high-dynamic range, leading to a DC measurement with current levels in the order of microamps. In order to lead to real world applicability, the production of the device needed to be compatible with mass production techniques. As the measurement required particle and cell interaction with a narrow channel, it also meant that the sedimentation and clogging were possibilities that needed to be addressed. These constraints were the main factors that influenced the final design of the device.

In microfluidic design, especially if the electrodes do not need to be integrated, the desirable procedure would involve soft lithograpy with PDMS. The most important reasons for such a design can be summarized by cheap production and transparency for allowing visual feedback. Soft lithography is a process based on a master copy that serves as a mold for curable polymers like PDMS. Preparation of the master, and the subsequent fabrication of the channel requires more processing steps in comparison to a direct etch on silicon based process. In addition, due to the insulating nature of the PDMS, it is also more difficult to validate the dimensions of small features, as it complicates imaging with SEM. A silicon based device can potentially allow easy integration of microelectrodes, anodic bonding with borosilicate glass for see-through design and provide resistance against pressure and organic solvents. Furthermore, building the device using common CMOS based fabrication processes allows for an easily mass producible design. Thus, device was designed to be fabricated directly on the silicon wafer.

As the goal of the device is to measure the current during cell translocation through a narrow constriction, clogging can be a major problem, requiring a channel structure that allows flushing. Therefore the channel shape was designed to be two U shapes connected to each other by the undulating channel. These U shapes formed the CIS and TRANS reservoirs. To remove the clogging cells at the entry of the undulating channel, manual pressure was applied from one end of the U shape, causing lateral sweep of the liquid at the entry of the channel.

In order to confirm the unimpeded cell translocation and removal of the coalesced cells, the device was designed to be see-through. In addition to the PDMS gaskets, the assembly used for interfacing the microfluidics with tubing had to be transparent as well. To achieve this goal, the assembly was designed to be fabricated using a SLA 3D printer with transparent polymethyl methacrylate resin. As the surface finish of the printed parts were not very smooth due to the layer by layer building mechanism, the design of the parts put emphasis on getting the final parts as flat as possible for easy polishing.

The data acquisition instrument was an in-house designed trans-impedance amplifier. The previous article on the topic used this amplifier to perform the experiments as well [45]. The measurements with this system provide low noise, high bandwidth data. As it was a DC measurement system, the current can reach up to microamps due to the size of the channel and the conductivity of the media used. This level of current precluded the usage of integrated micro electrodes. With such high current, the patterned electrodes would become dysfunctional after a short period of use. In addition, the voltage applied over the electrode would cause electrolysis and bubbles at the vicinity of the channel which in turn would occlude the passage of particles to be interrogated. As a result, the electrodes were designed to be external and exchangeable.

External electrodes influence design due to the limitations they introduce in terms of sensitivity of the device to the passage of a particle. External electrodes are common practice with nanopore measurements. This is feasible due to the geometry of the device, where the electrolyte serial resistance is minimized because the reservoirs are not constrained until the nanopore. To imitate the conditions in a planar device, the access channels of the device were designed to be as deep as possible until the media reached to the undulating channel. This is ensured by using a separate 700μm thick PDMS layer with features that mirror the U shaped channel on the silicon chip as in figure 3.2.c Layer 1. The device was designed to interrogate $\sim 13\mu$m diameter tumor cells. While setting up the undulating channel dimensions, narrow and wide unit regions were set to be the minimum length possible to attain the maximum sensitivity. As in figure 3.2.a, they are 25μm long each, corresponding roughly to 2 times as long as the diameter of the observed particles. The channel depth is 19.2μm, the wide regions are 25μm and the narrow regions are 15μm wide to keep the channel cross-section comparable to the diameter of the cells. Before the fabrication of the device, the resistance of the channel was calculated using Matlab algorithms,predicting a sensitivity over 2%. This design principle allowed the sensitivity to be higher by decreasing the serial resistance.

Another complication introduced by external electrodes is achieving a proper seal with a Ag/AgCl wire electrode under pressurized conditions. This problem was solved by tying a knot across a silicon tubing with the Ag/AgCl electrode inside. It provided seal against pressure levels far above experimental conditions.

The CTC chip was designed to meet the goals of mass production compatibility and instrumentation. Overall, the device proved to be very effective and versatile in interrogating live cells, allowing acquisition of valuable data. There are aspects of the device that could be improved to gather even more precise data. These improvements are going to be discussed in Future Work section on Chapter 4.

3.3 Fabrication

The devices were fabricated over a 500μm thick 4" single-side polished silicon wafer with <100> crystal orientation. After a dehydration bake at 150°C, the virgin silicon wafer was primed with HMDS adhesion promoter by a spin at 3500rpm for 30s. The HMDS was dried for 30s using a N_2 gun. The wafer was spin-coated with AZP4110 positive photoresist at 3500krpm for 30s and baked at 95°C for 1min. The features were exposed on the wafer in GCA 6300 i-line(365nm)

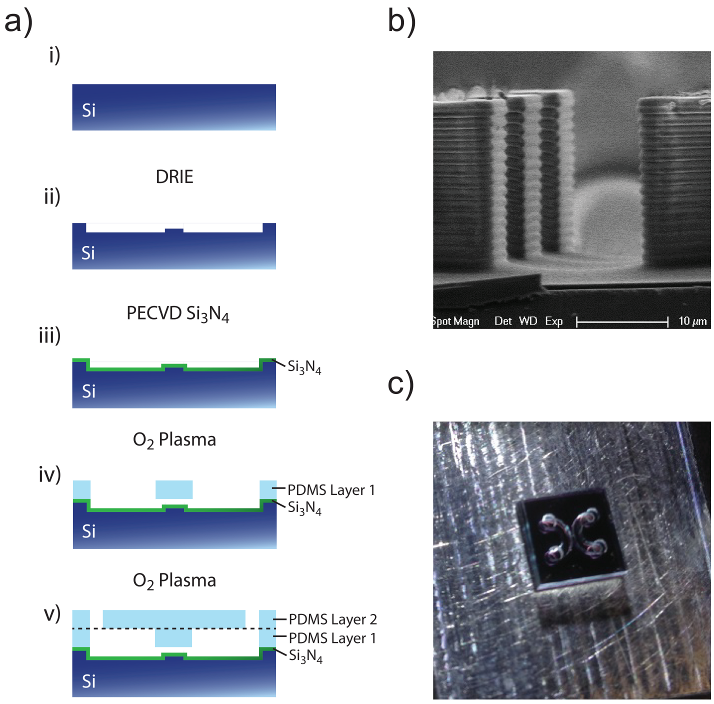

Figure 3.3: a) Fabrication steps of CTC detection chip. b) SEM image of the channel entry. c) Ready to measure chip.

Source:	825W
Bias:	9W
Pressure:	23mTorr
Flow Rate:	C_4F_8 0sccm
	SF_6 200sccm
	AR 40sccm
	O_2 0sccm
Duration:	60s

Table 3.1: Isotropic etch conditions in DRIE chamber.

stepper at 180mW/cm^2 for 0.5s. Exposed wafer was developed in 1:4 AZ400K developer for 90s. Following optical microscope inspection, the wafer was hard-baked at 110°C for 5min. The remaining photoresist residue was removed in O_2 plasma at 100W power and under 300mTorr pressure in 1min.

The patterned features on the wafer were etched in Plasma-Therm 770 SLR for 4.5min using a custom bosch etch recipe(see table 2.3). In order to achieve a very smooth surface, potential grassing due to the bosch process was removed by an additional 1min isotropic SF_6 etch with the recipe in table 3.1. As one can see in figure 3.3, the walls of the channel are vertical and the base of the channel is very smooth, preventing shearing and obstruction passing polystyrene beads and cells.

After the DRIE, the photoresist was removed using 1165 Photoresist Stripper at 80°C for 30 minutes and rinsed with isopropanol and deionized water. Subsequently, the wafer was thoroughly dried with N_2 and placed in ALD chamber for 300 cycles, resulting in a 343$\mathring{A}$ film. The ALD film was further enforced with a 600nm thick layer of PECVD Si_3N_4. The film thicknesses were measured using an ellipsometer. The final dimensions were confirmed by SEM and confocal microscopy(figure 3.2.b).

Before the chips were diced in a dicing saw, the wafer was spin coated with AZP4110 at 3500rpm for 30s and baked at 95°C for protection against the slurry produced during dicing.The diced chips were placed in 1165 Photoresist stripper at 80°C for 30min to remove the photoresist.

The PDMS layers were prepared by curing PDMS in a 80mm petridish using 10:1 4g of co-polymer 0.4g of cross-linker ratio at 65°C for 4 hours on a hot plate. When the PDMS was ready, the layers were cut using a Trotec CO_2 laser with 3mm focus distance and 30W power. A pulse frequency of 1000Hz in conjunction with 2m/s cutting rate and 16% power is used to cut the $\sim$700μm thick PDMS layers. The distance of 400μm between the U-shaped CIS and TRANS chambers was defined by the smallest feature attainable by the laser cutter without ashing the surface and making the plasma bonding impossible on the PDMS layer. On the second layer of PDMS, four holes were cut at the ends of U-shapes to provide access to the CIS and TRANS chambers using the same laser cutter conditions.

The PDMS layers were cleaned in Tween 80 mixture to remove the debris followed by scotch tape and solvent cleaning. Each layer was placed on a glass

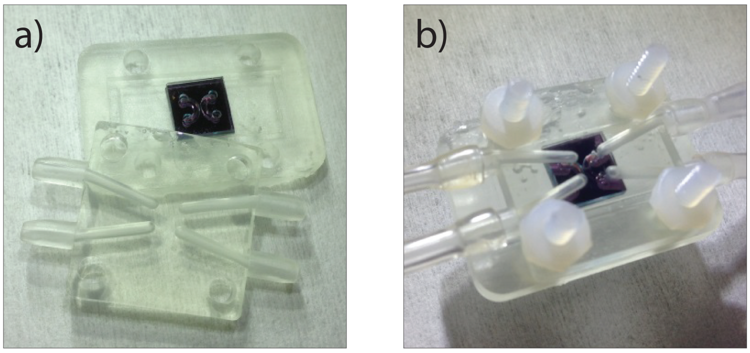

Figure 3.4: a) 3D printed assembly with chip inside. b) Clamped assembly ready to measure.

slide and exposed to the 30W O_2 plasma for 20 seconds at 300mTorr to activate the surface. Immediately after the plasma exposure, the PDMS layer is aligned and bonded on the chip using a custom made aligner. Then, the chip was placed on a hot plate at 75°C for 5mins. This process was repeated for the second layer as well, corresponding to figure 3.3.c.

The assembly consisted of two pieces that clamp around the chip. The bottom piece provided two grooves for placing permanent magnets to secure to the metal stage of the microscope for easy handling. It also included alignment marks for placing the chip to the center of the assembly. On the other hand, the top piece provided two tubes protruding from 2 opposing sides to match with the 2 input ports and 2 output ports of the ctc detection chip, as shown in figure 3.4. The access tubes in the 3D printed assembly was calculated to add 5kΩ serial resistance each side for a total of 10kΩ impedance based on the Matlab modeling. The assembly is printed using a Formlabs Form 1+ 3D printer using clear resin with 0.5mm layer resolution. The finished parts are very resilient against many solvents such as, acetone, ethanol, isopropanol, methanol and hexanes. The requirement for polishing arises from the fact that 3D printed parts have ridges on the surface due to the nature of layer by layer printing. The assembly was polished by using 1000,1500,2000 and 2500 grain size 3M wet/dry sand paper for 1min each in circular motion manually under wet conditions. After each sand paper step, the part was thoroughly rinsed. Next, the part was polished using a VWR cleanroom wipe in conjunction with NOVUS grade 3 and 2 scratch removers for 1min each. At the end of the process, the part looks completely transparent and ready to be used under a microscope. The flatness of the surface is confirmed by the PDMS adhesion properties to the polished surface. After polishing, the surface of the PDMS in contact with the assembly surface changes color visibly indicating a good seal between two surfaces. With the device ready and assembled in the 3D printed interface, the system needs to be routed with Tygon tubing to the media to be measured.

3.4 Microfluidics

One of the easily overlooked aspects of microfluidics is plumbing. Setting proper pressure and removing bubbles from the tubing can be complicated. As

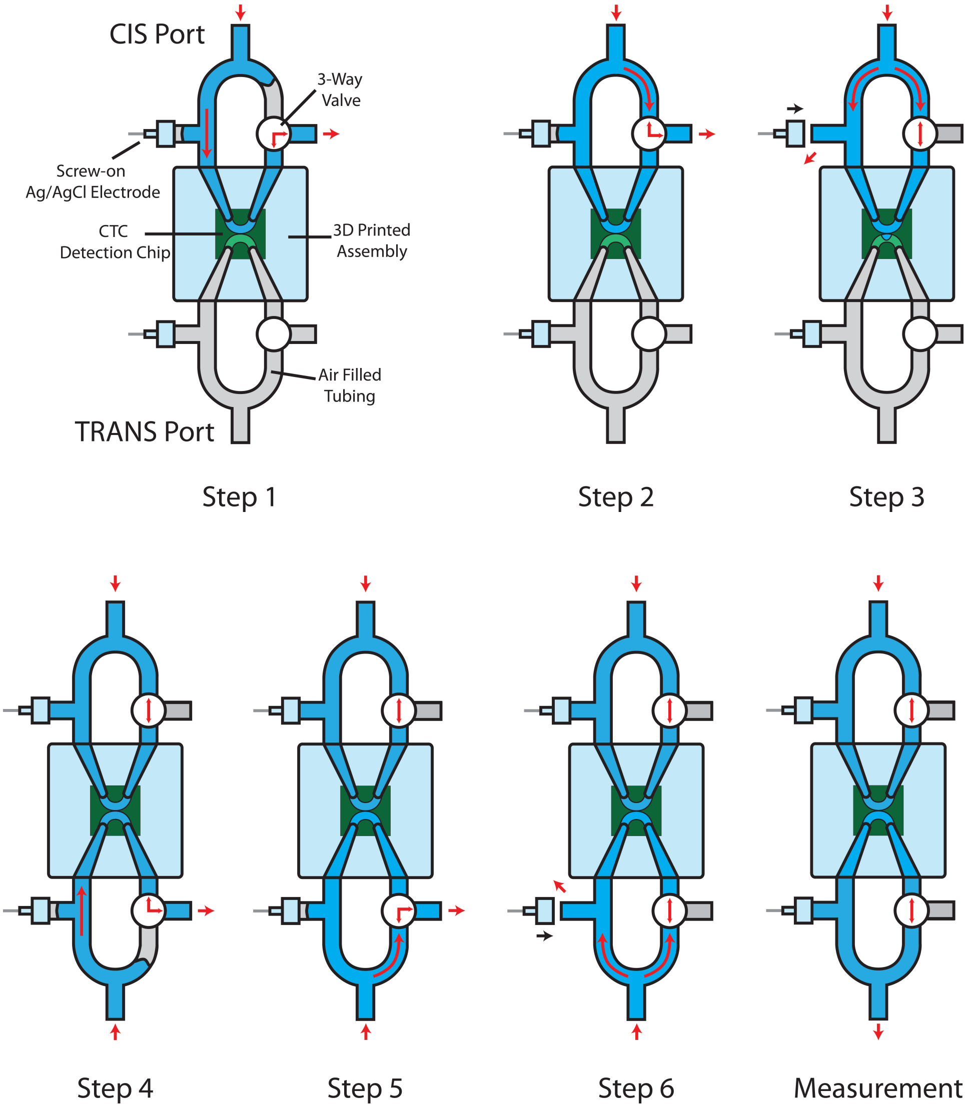

Figure 3.5: Steps of flowing media into the microfluidics.

can be seen in the plumbing diagram in figure 3.5, the tubing has two valves and several T joints. The electrodes were designed to be screwed in to provide seal in pressure and replaceable, while allowing high current flow.

The microfluidic system becomes ready to test in 6 steps. In the 1st step, the valve on the CIS side is switched to position 2 allowing media to flow through the channel inside the chip and exit from the system. During this step, the air inside the U-channel in the CTC detection chip is removed. However, this procedure traps air in the right side of the fork. Since uneven pressure at the entrance of the undulating channel causes the event characteristics to change significantly, it is crucial to have equal pressure from both branches of the CIS chamber.

In the 2nd stage, the liquid is flown from towards the right branch of the fork to push the trapped air while the valve is in position 3. At this point the only air pocket left in the tubing is at the electrode interface in the CIS chamber.

During the 3rd stage, the media is flown normally but the electrode is screwed out to allow leakage with valve in position 1. When the electrode port starts overflowing, the electrode is screwed in forming a bubble free microfluidic environment in the CIS chamber. At this point, the TRANS reservoir is inspected in the U channel on the chip to see if the undulating channel is also partially filled with the media as can be seen in figure 3.5 Step 3. If it is filled, the steps 1 to 3 are repeated on the TRANS reservoir side, by providing media through the output port using an injector, making the system ready for actual measurements.

3.5 Experiments

The 3D printed assembly was designed to be used under a Omano stereo microscope with a 2X barlow lense. The 2X barlow decreased working distance significantly and made illumination challenging. Therefore, the device was illuminated through one of the eye piece ports and recorded from the camera port with a 14 megapixel CMOS 14X camera at a total magnification of 126X. The camera had USB3 interface and capable of delivering 45fps at 1024x768 pixel resolution video with adequate illumination to minimize exposure time. The chip assembly was placed underneath the microscope, and connected to the transimpedance amplifier. After negating the offset voltage due to the circuitry and the electrodes, the measurements were recorded at 500kHz sampling rate using a Data Translations DAQ(DT9862). During the measurements, videos of the bead and cell translocations were also concurrently recorded.

The bead experiments were performed in a 23% glycerol, 0.1% Tween80, 20mM Tris, pH7.4, 100mM KCl electrolyte solution with a conductivity of 8.4mS/cm. The gravity of the solution was increased to ensure that the 10μm polystyrene

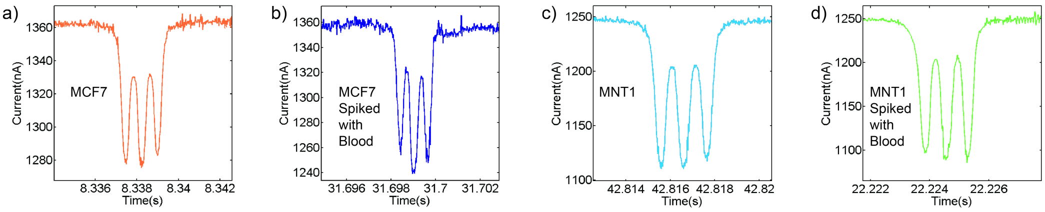

Figure 3.6: Panel of typical current signatures obtained when cells are passed through the system a) MCF7 cells b) MCF7 cells spiked with blood, the trace shows that the presence of blood cells does not adversely affect the measurement. c) MNT1 cells. d) MNT 1 cells spiked with blood again showing the insensitivity of the measurement to the presence of blood cells.

beads and the electrolyte were at similar densities to prevent sedimentation at the bottom surface of the channel and clogs at the undulating channel.

A control measurement without beads were taken to establish a baseline. High concentration Bang Labs beads were sonicated for 15 minutes, and a $100\mu l$ aliquot of the solution was added to 50ml of electrolyte solution. The solution was provided a hyrostatic pressure of 2477Pa to drive the beads towards the undulating channel. The measurement was interrupted several times due to clogging. After a flushing procedure the channel was operational again. The measurement was continued until the undulating channel was permenantly blocked by beads.

For the cell measurements, a solution of 34% pluronic 150mM HBSS solution with pH7.4 was used with a resistivity of 110Ω·cm. After control measurements, a solution of MCF7 cells were added to the channel. After an unclogged recording

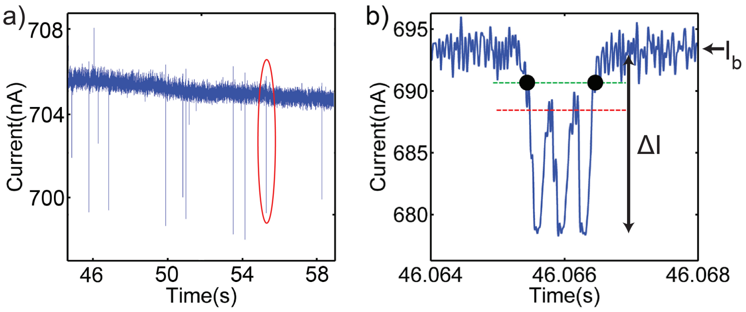

Figure 3.7: a)Sample current trace data from 10μm polystyrene bead measurement. The red circle indicates an event. b)Close-up of a pulse marks the baseline current level, I_b and the blockage current, ΔI. An event contains three pulses associated with 5 zones.

of 40 minutes, the a 100μl solution of mice blood was spiked into a 50ml solution. The measurements with this solution was taken for one hour as well. At the end of the experiment, the channel was clogged and required a flushing procedure. The flushing procedure consisted of sonication and bleach solution followed by an ethanol rinse. The same measurement was repeated one more time with MCF7 cells and another measurement was performed with melanoma cells(MNT1) with the same procedure. During these recordings, the video clips of the cells translocations were recorded as well. The collected data was analyzed using Matlab scripts.

3.6 Pulse Detection and Level Finding Algorithms

The recorded data consists of stochastic pulses over current trace data with drifting baseline, like seen in the figure 3.7.a. The current amplifier used in the measurements is a custom designed circuit capable of canceling baseline current and measuring the residual current with higher amplitude resolution and lower noise than a commercially available equipment. As a characteristics of the amplifier, the data is output from two channels, corresponding to the baseline current and the residual current. The open channel current value I_b, shown with an arrow in the figure, is used as a reference for calculating the blockage current, ΔI. As the figure is for 10μm bead,there are only two major blockage levels associated with the narrow and wide region respectively. On the other hand, these levels show greater variety for cells due to their viscoelastic properties.

After a conversion of the raw data from the amplifier to the current value, a 30kHz 8-pole Bessel low-pass filter is applied on the data. Then, the data is analyzed by a custom Matlab algorithm that locates the data points above a certain threshold. The threshold is set to be 4 times the standard deviation of the residual current to reject noise. When a data point above the threshold is located, the algorithm traverses the current trace backwards until the current level drops to the noise level and records the time-stamp associated, marking the beginning of an event. Next, the algorithm traverses forwards until the current level drops to noise

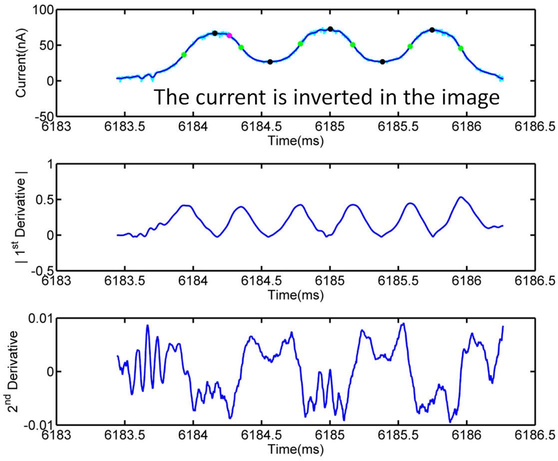

Figure 3.8: The current trace associated with an event and its derivatives. In the top panel, the trace in light blue shows the original current trace. The superimposed blue trace is the plot of 30kHz low-pass filtered data. The green dots mark the inflection points between the zones, while the black dots indicate the extrema.

level and records the time-stamp to mark the end of an event. The data between the event start and end time-stamps are analyzed for the maximum blockage level, event duration and current levels. This process is repeated for the rest of the data points in the current trace. For each event, another function specific to analyzing CTC events take over. It performs a moving average filter over the first derivative of the current and takes the absolute value of it as in figure 3.8 middle panel. This process allows to discern the greatest rate of change in the current while a particle is going through the channel. Obviously, these changes would most likely to occur at the boundaries of electric field regimes dictated by the channel geometry. Thus, the top 6 greatest magnitude inflection points are considered to be the transition points between 5 different regions of the undulating channel. Between these points, the maximum and minimum data points are found and recorded as the current level associated with the narrow and wide regions. In addition to these features, the inner function is capable of displaying each event and allows the user to choose if they would like to keep the event or not as an option. After the data analysis, the events with the correct number of current signatures are kept. Due to the channel structure in the ctc detection chip, there needs to be only 3 sections associated with the narrow regions and 2 sections associated with wide regions.

3.7 COMSOL Modeling

Various aspects of the channel geometry and its physics were computed in multiple stages. The complete channel geometry is a complicated topology that spans centimeters. Much of this area could be easily generalized in comparison to the critical features of the channel which are in the order of tens of micrometers. In order to decrease the complexity of the model geometry and simulation times, the topology was limited to the vicinity of the undulating channel and simplified. The initial goal of the simulations was to confirm that the result difference of the proposed simplifications to channel topology would be negligible with respect to the detailed model. Next, the model was simulated in 2D with time-dependence to

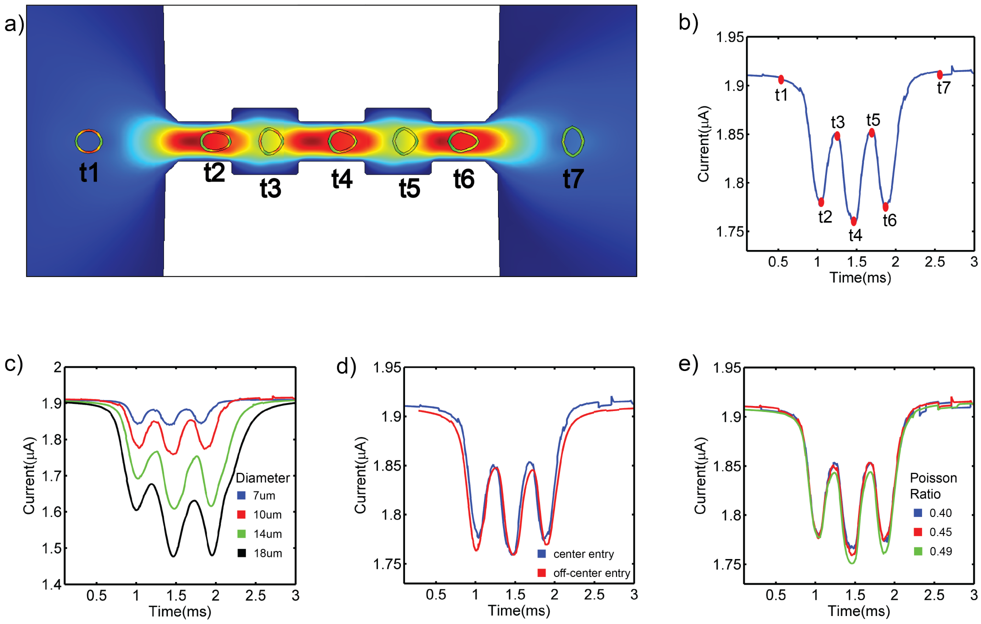

Figure 3.9: a) 2D Transient Comsol simulation of a viscoelastic cell passing through the undulating channel. t1-t7 indicated the time stamps at the different locations indicated on the figure as the cell passes through the channel. As shown in the figure the cell is deformed by varying degrees as it traverses each zone since it experiences different pressure drops. b) Example current trace from the coupled simulation, timestamps on the trace correspond to the cell at different points in the channel as indicated in (a). c). Simulated current signatures for cells with different diameters. d) Simulated current trace showing the differences in the signature when the cell enters the channel on axis versus off-axis. e) Simulated current trace as the Poisson ratio is varied.

analyze the deformation of the cell in the channel and its related current signature. Building up on the findings of the 2D model, another 3D model with precise variation of the cell sizes were simulated to elaborate electrical blockage trends, enabling the interpretation of acquired cell data.

After the confocal microscopy measurements, it became clear that the bottom of the channel had slight height variations due to the DRIE etch characteristics. The simulation of these features proved to be difficult to converge and computationally intensive even for static models that solve Navier-Stokes and Nernst-Planck equations. Therefore, it was imperative to investigate if these channel features have significant impact in current and flow profile. An accurate model of the channel was simulated with Navier-Stokes equations and Nernst-Planck equations separately in steady state condition. These results were compared with the simulation results for a simplified model and the difference was found to be negligible.

To capture the viscoelastic nature of the cells, the domain associated with the cell was modeled as a two layer structure. The outer structure simulates the cell membrane with its elastic properties, while the inner portion is an incompressible liquid like the plasma. Time-dependent simulations of complex physical phenomena can be very sensitive to initial conditions. In the case of our study, the initial conditions supplanted to the simulation needed to be computed in

2 static phases before proceeding with the actual time-dependent simulation to achieve convergence. In the first phase, the cell is placed in its initial location , However the domain associated was assigned with the properties of water, like the surrounding domains. This simulation allowed the calculation of the average flow rate in the initial location of the cell. In the second phase, the domain of the cell is removed from the simulation topology, causing the surface of the cell to act as a wall outside the channel. The boundary conditions of the cell is set to be moving with the average velocity of the flow rate calculated in the phase one as initial conditions for the static simulation. The result of the second phase provided reasonably close initial conditions of a general flow in the structure with a cell just outside the undulating channel. Finally, in the transient simulation the two layer cell structure was implemented. The transient model time steps were calculated using PARDISO solver and 5th order backward differential equations to provide a stable simulation. With the fluid flow the cell begins to move and requires mesh updates whenever element quality drops below a certain threshold. When the cell enters the undulating channel, it deforms due to the pressure gradients produced by the fluid flow in the channel as in Figure.a. The simultaneous solution of Navier-Stokes and Nernst-Plank equations with structural mechanics in time-domain made analysis of the effect of various parameters possible.

The main simulation parameters were the inlet pressure, entry angle, cell diameter, cell plasma viscosity, Poisson Ratio and Young's Modulus of the cell wall. In the interest of building an intuition about the role of these parameters, a reference set of values was chosen based on literature and simulation ease. Then, each of these parameters were changed one at a time to observe its effects. As the diameter of the cell was increased, the cell shape began to conform to the shape of the channel, sometimes bridging two wide zones. As one can see in the figure.c, the current signature associated with this situation is easily seen in the distortion of the pulse characteristics of the 14μm and 18μm diameter cells. The current simulations of center entry cause lower blockage levels in comparison to off-center entry as plotted in figure 3.9.d. On the other hand, Poisson Ratio of the cell wall determines how much the cell compresses under pressure. Young's Modulus of the cell wall dictates the flexibility of the cell under pressure, leading to higher current blockage levels with higher moduli. The last important variable is the viscosity of the inner fluid which governs the response rate of the cell to pressure changes. For example, if the viscosity is high, the cell will not be able to relax in the wide zone before entering the next narrow zone. It can be seen from the figure 3.9 that by simply looking at the current outputs, it is not easy to determine several parameters all at once. Therefore, the results were further analyzed as a function of the occurrence of current levels and cell shape given a location in the undulating channel in the next section.

Based on data analysis of the current simulation characteristics of a variety of input parameters, two locations of interest were located. These locations serve as reference measurement for cell size and deformation measurement for cell flexibility. The details of how these spots are located are discussed in Section 3.8. On these two spots, current conduction simulations in 3 dimensions were performed for various cell sizes and polar-to-equatorial axis ratios to produce analytic equations, yielding the electrical shape factor. In the first spot, the a/b ratio is kept at a constant 1.14, and the cell diameter was swept from 5μm to 20μm. In the second spot, both the cell diameter and the a/b ratio were swept within the boundaries of the channel walls. The result of these simulations allowed us to form universal equations for these two coordinates to decode the cell size and deformation based on the pulse analysis on the acquired experimental data.

3.8 Data Analysis

Deformation of the cells were measured in several stages of data analysis. The first step to accomplish was to adapt the analytic equations to the conditions of the undulating channel. Next, these equations were used to analyze the polystyrene bead data, which provided valuable insights. Using the analytic equations, the beads could be accurately sized in all the zones when the off-axis effect was canceled. But more importantly, distribution of the ΔR values exhibited a flow focusing effect which allowed us to justify skipping the off-axis correction for the cell measurements, decreasing the number of variables. However, due to the complexity of the system, the derived equations did not directly apply to cell translocations. Therefore, a detailed study and simulation of cell deformation was undertaken in COMSOL to evaluate the case specific electrical shape factors. Utilizing the simulation findings, the cell deformations were deduced using a combination of numerical and analytic methods.

The analytic equations that describe the current blockage were derived for a uniform cylindrical geometry. From the experimental data, ΔR could be calculated easily.

$$\Delta R = \underbrace{\frac{V_{applied}}{I_{baseline}}}_{R_{total}} - \underbrace{\frac{V_{applied}}{I_{blockage}}}_{R_{blockage}} \tag{3.14}$$

But the total resistance of the channel did not reflect the V in the equation 3.1 as the cross-section changed across the channel and produced different blockage levels as opposed to a single level in a simple geometry. When the basic terms of the equation 3.1 were adapted to the case of the CTC detection chip, they became:

$$R = \frac{\rho 2r}{hw} \tag{3.15}$$

$$v = \frac{4}{3}\pi r^3 \tag{3.16}$$

$$V = lhw = 2rhw \tag{3.17}$$

where h and w were the cross-sectional height and width of the channel, respectively, and r was the radius of the particle. In these equations, the total resistance, R was written as a function of the resistivity, ρ rather than a direct measurement. Due to the undulating nature of the channel, the equations derived for a simple channel geometry did not directly correspond to this particular case. Consequently, the total resistance and the volume that the particle blocks were pegged to the size of the particle and the zone that the ΔR was induced. That was the reason the length, l in the total resistance and total volume equations was two times the radius of the particle. When these values were placed back in to the equation 3.1, it becames:

$$\Delta R = f \left[\frac{4\pi\, r^3}{3(hw)^2}\right] \tag{3.18}$$

The rearrangement of the equation in this form allowed us to isolate electrical shape factor from the known values.

The analysis of the 10μm polystyrene beads was straight-forward due to the spherical shape of the beads, causing f_s to be a constant 3/2. Looking at the plot in figure 3.10.d, it is easy to see that ΔR distributions for Zone 3 and Zone 5 are almost indistinguishable while the distribution for Zone 1 is centered around a higher value. Considering the fact that all these constrictions have the same

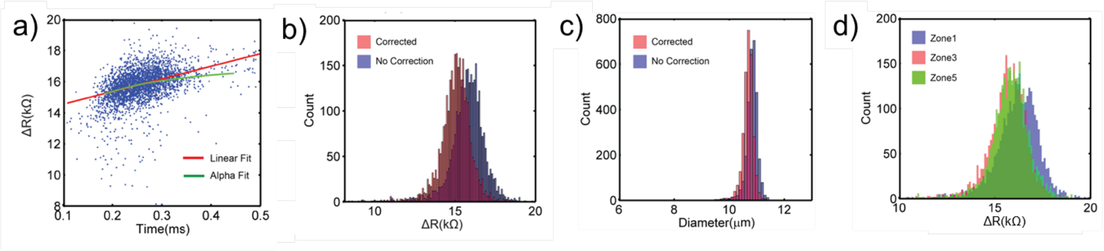

Figure 3.10: a) Resistance change, ΔR due to translocation of polystyrene beads associated with Zone 5 vs duration; Linear Fit in red used for off-axis correction; Fit for the factor (see text). b) ΔR Histogram for Zone 5 with and without off-axis correction. c) Diameter distribution of Polystyrene beads based on the resistance change in Zone 5 with and without off-axis correction. d) ΔR Distribution associated with all the narrow zones (1,3,5). Resistance change when the bead is in Zone 1 is greater compared to when it is in Zone3 and Zone5, indicating a flow focusing effect.

cross-sectional area, they are supposed to produce the same blockage level. This discrepancy is due to the off-center entry of the bead to the channel in Zone 1, causing the bead to traverse closer to the walls of the channel where the fluid flow is slower. In addition to taking longer to translocate, beads produce higher blockage levels due to the higher impact on the density of the E-field lines in comparison to the case of a center-entry.(See Section $Measuring\ Deformation$, eq 3.11 and eq 3.13)

Saleh described a simple method to negate the effects associated with the off-center beads [78]. The article proposes to fit a line over a ΔR versus duration plot and subtract it from the general ΔR population. When this method was applied on the data for Zone 5 as in figure 3.10.a, it yielded a very miniscule change(see figure 3.10.b), confirming that majority of the beads were centered when they came to the Zone 5. Furthermore,the factor α in equation 3.11 was fit using numerical methods, producing a value of 3.7. The fact that α was close to the low physical limit also demonstrated the flow focusing effect.

In order to determine the radius of the translocated beads, an array of ΔR values, ΔR_{map} was calculated as a function of a discrete set of bead radius values spanning the possible dimensions with the following equation:

$$\Delta R_{map}(r) = \frac{3}{2}\left[\frac{1}{1-0.8\left(\dfrac{d}{D}\right)^3}\right]\left[\frac{4\pi\, r^3}{3(hw)^2}\right] \quad \text{where} \quad r = \{0.01, 0.02, 0.03...20\mu m\} \tag{3.19}$$

where D was the diameter of a cylinder in the original equation 3.3. As the channel cross-section was rectangular, an effective diameter for this value was used:

$$D_{eff} = 2\sqrt{\frac{hw}{\pi}} \tag{3.20}$$

By matching the ΔR of each event to the closest ΔR_{map}, the radius of the particles were resolved through the corresponding radius sweep array indices. In figure 3.10.c, it could be seen that the size of the beads with and without correction was very similar to each other; 10.7μm and 10.8μm. Therefore, it could be stated that due to the flow focusing effect prevalent in the channel, the error associated with off-axis traversal was minimal. This finding was especially important to decrease the number of variables to account for in the analysis of cell translocations.

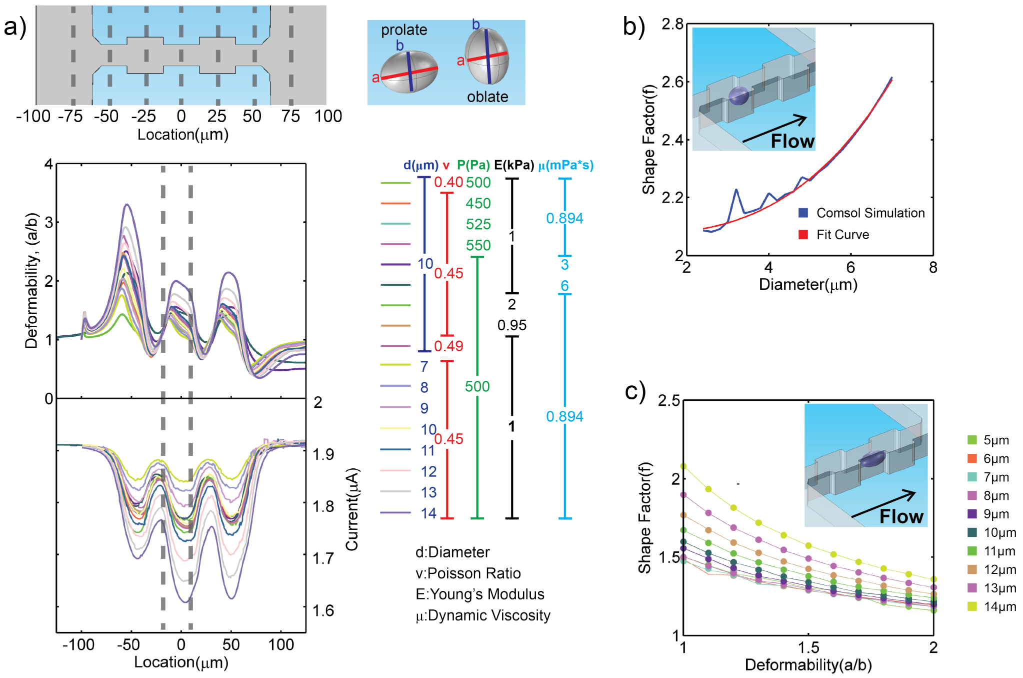

Figure 3.11: a) Deformation plots of multiple 2D COMSOL cell translocation simulations with varying model parameters. At the location marked with red circle(spot1) invariably all cells have the same deformation level(slightly prolate) and it corresponds to the current peak associated with zone 2. Also shown is the location where the current trough associated with zone 3 occurs. b) Calculated electrical shape factor for spot 1 based on 3D COMSOL current simulation for a spheroid as a function of cell diameter while undergoing the same deformation enabling the determination of cell size. c) Calculated electrical shape factor based on the 3D COMSOL current simulations for a spheroid as function of deformability for various diameters. These curves allows the determination of cell shape given the calculated diameter based on the current peak in zone 2

As opposed to bead translocation conditions, there were several additional variables in cell measurements, like the actual shape of the cell, a wider distribution of cell sizes and the flexibility of the cells, considering the off-axis effects could be discarded. The polar to equatorial axis ratio of the cells could not be determined through ΔR measurements unless the size of the cell was known. Because cells with different a/b ratio and size could produce the same level of ΔR, making a reference measurement for cell sizing imperative. A reference measurement required an identifiable current signature associated with the passage of all cells from a common location in the channel with the same a/b ratio. In order to find such a signal in an event, several 2 dimensional COMSOL simulations were performed as described earlier sections. Using the coordinates of the spline boundaries for the cell structure, a/b ratios of all the time steps were calculated and plotted versus coordinates in the channel as in figure 3.11.a. Fortunately, one spot in the channel presented properties of a reference measurement(marked with red circle in the figure 3.11.a. This particular spot corresponded to close to the end of the Zone 2 where after being pushed to assume an oblate geometry the cells were beginning to comply with the flow field of the narrow Zone 3. Since each cell went through this regime change independent of their flexibilities and several other variables, all the cells conformed to a very similar a/b ratio(between 1.14 and 1.20). The fact that the cells were in their most prolate state in the wide region, caused it to produce the lowest blockage level in the current event, providing an easily identifiable current signature.

The analytic equations derived for simple geometries did not describe the current blockage characteristics accurately. Therefore, a 3D static conduction simulation was performed in COMSOL, keeping the a/b ratio same and sweeping the radius of the cell in the coordinate of interest at Zone 2(see figure [ref]). The current data produced by the simulation was treated in the same manner as the experimental data was treated to calculate ΔR. After a rearrangement of the equation 3.18 to:

$$f = \frac{3(hw)^2 r^3}{4\pi \Delta R\ \rho} \tag{3.21}$$

the electrical shape factor was calculated for the COMSOL simulations. A power equation was fit on the simulation results for the purpose of formulating an electrical shape factor equation as a function of the cell size. The form of the equation was:

$$f = k_1 * r^{k_2} + k_3 \tag{3.22}$$

Using the same methodology as the bead data analysis, an array denoted as ΔR_{map} was calculated sweeping the variable r:

$$\Delta R_{map}(r) = f\ \left[\frac{4\pi\ r^3}{3(hw)^2}\right] = (k_1 * r^{k_2} + k_3)\left[\frac{4\pi\ r^3}{3(hw)^2}\right]$$
$$\text{where} \quad r = \{0.01, 0.02, 0.03 ... 20\mu m\} \tag{3.23}$$

The closest match for ΔR_2 from the experiment in ΔR_{map} was found and used to relate to the radius through its index. Based on the cell sizes resolved through ΔR_2(Zone 2), the electrical shape factor f could be isolated for different zones.

In order to quantify the polar to equatorial axis ratios of the cells, a deformability measurement was necessary. The requirements for such a measurement is similar to the reference measurement; an identifiable current signature associated with the passage of cells from a common location, but different a/b ratios. 2D COMSOL Simulations yielded that the peak associated with the Zone 3 displayed a wide range of a/b ratios and occurred about 4.8μm of the center of Zone 3 for all the cells, as shown in figure 3.11. Subsequent to evaluating the electrical shape factor for Zone 3 experimental data(using equation 3.21), the correspondence of it to a/b ratio was investigated. To acquire more insight about the characteristics of current blockage in the deformation measurement coordinates, another 3D static conduction simulation was perfomed in COMSOL, sweeping the cell radius and polar to equatorial axis ratio. The electrical shape factor was calculated for simulation results using equation 3.21. From this simulation, a family of curves were acquired and equation 3.22 was fitted over them as in figure 3.11.c. For describing these curves with a single equation, an empirical approach was employed. The resultant equation was:

$$f_{map} = f_s \left(\frac{1}{1 - 0.8(d/D_{eff})^3} \right) - 0.05 \tag{3.24}$$

where D_eff was calculated according to the cell's radius and a/b ratio. When the size of the cell gets large and prolate enough, a portion of the cell would be in wide Zone 4 region. Therefore, the D_eff was a function of cell radius and polar to equatorial axis ratio as well. In addition, a constant of 0.05 was required to increase the accuracy. This offset can be explained by the irregularity of the field lines around the narrow to wide region transitions.

Given the radius of the cell from Zone 2, using equation 3.24 an array was calculated by sweeping a/b from 0.1 to 10. The closest match for the experimental f in the particular f_{map} for the cell provided the index of the corresponding a/b sweep array whereby the a/b ratio. The difference in the value of a/b for different cell types could be used to distinguish

3.9 Discussion of the Data

Analysis reveals that the CTC detector chip can distinguish MNT1 cells from MCF7 cells when cells are below $\sim 14\mu$m diameter. In our measurements, as one can see in figure 3.12.c blood does not affect the measurements. This is an exceptional accomplishment, considering the reduction of infrastructure in comparison

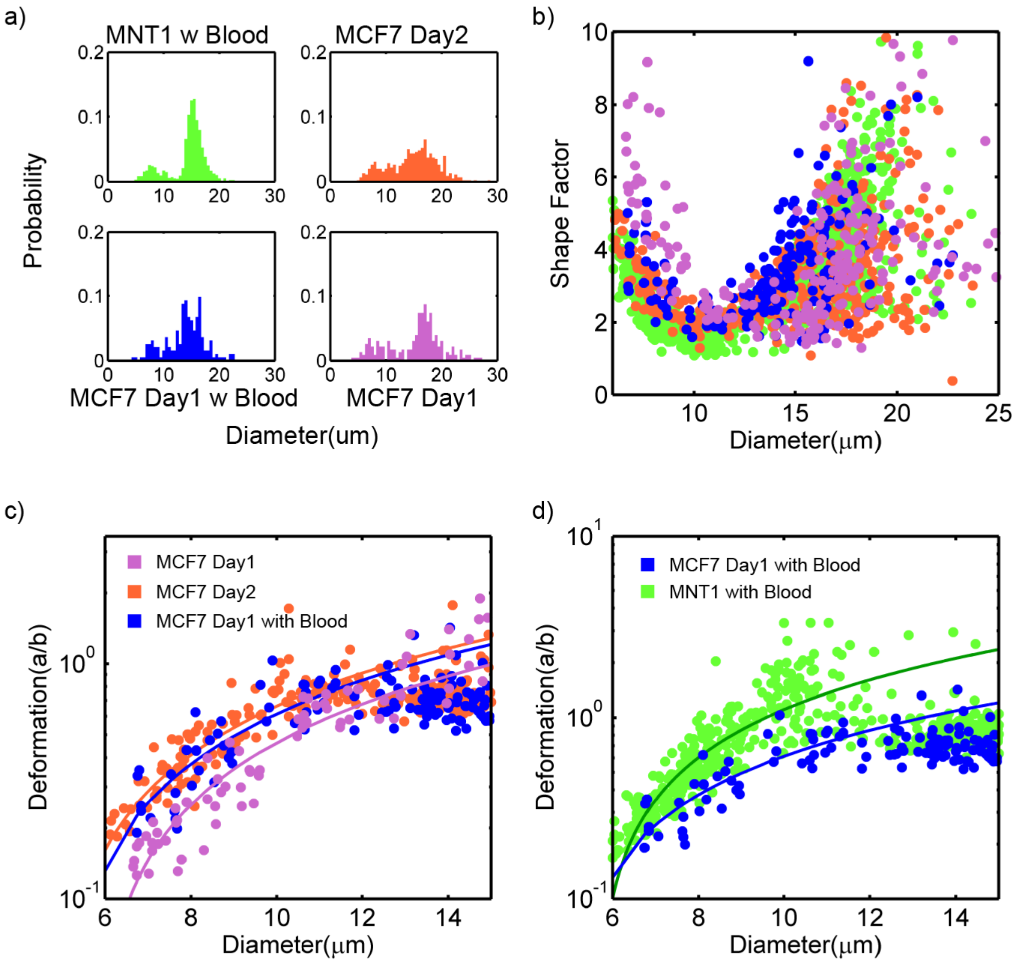

Figure 3.12: a) Size distribution for MCF7 and MNT1 cells computed from the measured current signatures using the procedure outlined in the text b) Calculated Electrical Shape Factor, f as a function of MCF7 and MNT1 cells diameters. c)Deformation of MCF7 cells as function of cell size. d) Deformation comparison of MCF7 and MNT1 cells. As seen from the plots MNT1 cells are more prolate (a¿ b) compared to MCF7 cells for diameters larger than 9μm. The fitted trend lines show that MNT1 cells are softer than MCF7.

to the cutting-edge work of Otto et al [73]. This was possible due to a coherent design and novel techniques used to perform data analysis and simulations. Utilizing this system, we can make cancer diagnostics one step closer to detecting circulating tumor cells.

Looking at the figure 3.12.a, one can see the distribution of the cell sizes used in the analysis. In part b of the figure, the electrical shape factor all the cell measurements are laid out. Although they look very similar, when the deformation, a/b is plotted the differences in the cell flexibilities are distinct. In figure 3.12, it can be seen that the slopes of the deformation as a function of times are the same even with the blood in the measurement. Based on the data, we can say that blood does not affect the quality of the measurement. Furthermore, during the experimentation, the only difference registered was an increase in the noise level of baseline current. The reason for the lack of response for red blood cells can be explained by their miniscule size compared to the cancer cells. On the other hand, inherent white blood cells, leukocites were too big to translocate through the channel, resulting in clogs. This was resolved by flushing the U channels when necessary to clear up the entry of the undulating channel. Finally, in figure 3.12.d, the difference in the slopes of MCF7 breast cancer cells and MNT1 melanoma cells are clear. Utilizing the CTC detection chip we are able to evaluate that the MNT1 cells are softer in comparison to MCF7 cells since they become increasingly more prolate with pressure induced by the narrow zones as cell size grows.

Although the CTC chip is an achievement, it has some short-comings such as being able to measure cells only up to 13μm accurately. This is due to the channel geometry which distorts the cell bigger than this diameter, causing them to span several separate zones and producing stochastic blockage levels that do not have analytic solutions. The flow rate of $14nl/min$ through the channel is too little compared to the volume of the blood required to be analyzed. To put things in perspective, it is thought that there is 1-5 CTCs per 1ml of blood [2], whereas there are 1 billion red blood cells and 10000 white blood cells. These problems can be fixed with a redesign of the channel and extensive parallelization.

We designed a specialized Coulter Counter capable of measuring the deformation of cells. This is an important achievement when the infrastructure of Authors' work is taken into account. Our CTC detector system does not require advanced camera and image recognition techniques that can be bulky and computationally intensive. The infrastructural reduction was achieved by a well-designed channel and innovation in analysis techniques. For the data analysis, custom designed level finding and curve fitting algorithms along with extensive COMSOL simulations were instrumental. As a result of these methods, the CTC detection chip can be miniaturized even further and parallelized, making on-field diagnostics possible and affordable. This technique also has an upper hand in comparison to anti-body detection based immobilization methods due to its cancer-type agnostic detection mechanism. Therefore, this endeavor can take effective cancer diagnostic techniques one step further.

Chapter 4

Future Work

4.1 Solid-State Nanopores

Solid-state nanopore with embedded electrodes is a complicated project that requires a significant amount of labor intensive testing to verify the properties of the membranes. Probing the contact pads of a 3mm diameter chip while maintaining a good seal on top and bottom surfaces is a challenge.

In the future work, the die size can be increased to 7mm x 7mm. This would enable easier handling of the chips and decrease the stringent constraints associated with assembly. The trade-off is that it will not be compatible with TEM drilling and inspection if necessary. It will require dicing in order to analyze the surface properties and pore sizes.

Another update can be changing the wafer handle with Foturan glass. Normally, it is difficult perform through etch with insulating materials like SiO_2, Si_3N_4 and Al_2O_3. On the other hand, Invenios brand Foturan glass is a photo sensitive material that provides 30:1 etch selectivity after exposure. Switching the conductive wafer handle with an insulator would greatly improve the bandwidth. It will also enable using larger contact pads as the coupling through the silicon wafer handle is eliminated. In addition, it will alleviate concerns associated with membrane exposure area through the gasket, making gasket alignment trivial.

The electrode depositions can be done in two steps to decrease the impedance of the leads from 16kOhms to tens of Ohms. This scheme would involve a thin deposition of Pt over the membrane area with fine resolution, followed by a thick deposition over the rest of the surface.

The insulator between the electrodes can be switched with ALD molybdenum disulfide, which proved to be a material that can withstand ionic currents even when it is a mono layer thick. This would ultimate increase the resolution to single base.

The last update to the design is to define the pore on each membrane by e-beam lithography. This would significantly decrease the variability in pore sizes and shapes caused by the manual TEM drilling.

In the case of the following updates, this architecture would provide a leading edge in nanopore detection with single base resolution.

4.2 DNA Nanotube Sizing

DNA nanotube sizing and other macro molecule classification projects would greatly benefit from some improvements to the experimentation setup. In order to improve the conditions in a silicon nitride nanopore, a bigger pore with lower molarity needs to be used. A good candidate size and electrolyte concentration would be 30nm diameter pore in 10mM KCl concentration. The goal is to increase the radius of the E-field extending from the pore to allow DNA nanotubes to better align with the pore axis. Moreover, the applied voltage needs to be decreased to the range of 100mV to decrease the possibility of disintegrating the DNA nanotubes inside the pore.

To better determine the size of the nanopore, it would be helpful to simulate the translocation properties. The calculated drag force could be used to estimate the translocation velocity and transform even durations to nanotube length.

Another possibility is to use a nano-channel to work in more two-dimensional geometry, causing the E-field gradient to extend for hundreds of nanometers, rather than the tens of nanometers that arise from a 3D nanopore geometry. It would be essential to have sensing electrodes embedded near the entrance and exit of the channel. Then the reservoir electrodes can be used to impose a steady current and two or even three embedded electrodes can sense changes in conductance due to translocating nanotubes in a 4-probe measurement. Using a third electrode inside the channel can provide a direct measure of translocation velocity.

4.3 Circulating Tumor Cell Detection

Developing CTC detection technologies will continue to be a great scientific endeavor for years to come. A complete CTC detection chip would incorporate many aspects of measurements to ensure reliability of the results. I will describe the first steps to take to have a more reliable system.

The channel dimensions need to be increased to accommodate bigger cells. The channel dimensions can be optimized by using COMSOL simulations. This feat can be accomplished by using the channel dimensions as fit parameters. The simulations can be solved using supercomputing clusters to shorten the development time.

Another improvement would be to integrate multiple electrodes into the channel and perform AC measurements to determine the channel conductance. Especially increasing the channel dimensions would make this design change imperative as an external electrode would have a significantly reduced signal to noise ratio.

The integration of a dean flow system at the entry of the channel can separate target size cells from red blood cells, leading to a lower noise measurement with less possibility of clog. Also, designing a flow focusing aperture before the channel entry would greatly reduce the noise in the data due to off-axis traversal.

After the accomplishment of these design changes, a wide range of cells can be tested to build a cell data bank. Using the distributions, the cancer type can potentially be resolved very accurately.

Bibliography

[1] André A Adams, Paul I Okagbare, Juan Feng, Matuesz L Hupert, Don Patterson, Jost Gottert, Robin L McCarley, Dimitris Nikitopoulos, Michael C Murphy, and Steven A Soper. Highly efficient circulating tumor cell isolation from whole blood and label-free enumeration using polymer-based microfluidics with an integrated conductivity sensor. *Journal of the American Chemical Society*, 130(27):8633–8641, 2008.

[2] Catherine Alix-Panabières and Klaus Pantel. Challenges in circulating tumour cell research. *Nature Reviews Cancer*, 14(9):623–631, 2014.

[3] and others. Means for counting particles suspended in a fluid, October 20 1953. US Patent 2,656,508.

[4] Philip M Ashton, Satheesh Nair, Tim Dallman, Salvatore Rubino, Wolfgang Rabsch, Solomon Mwaigwisya, John Wain, and Justin O'Grady. Min-

ion nanopore sequencing identifies the position and structure of a bacterial antibiotic resistance island. *Nature biotechnology*, 2014.

[5] Jingwei Bai, Deqiang Wang, Sung-wook Nam, Hongbo Peng, Robert Bruce, Lynn Gignac, Markus Brink, Ernst Kratschmer, Stephen Rossnagel, Phil Waggoner, et al. Fabrication of sub-20 nm nanopore arrays in membranes with embedded metal electrodes at wafer scales. *Nanoscale*, 6(15):8900–8906, 2014.

[6] Marija Balic, Anthony Williams, Henry Lin, Ram Datar, and Richard J Cote. Circulating tumor cells: from bench to bedside. *Annual review of medicine*, 64, 2013.

[7] Hagan Bayley. Nanopore sequencing: From imagination to reality. *Clinical chemistry*, 61(1):25–31, 2015.

[8] Nicholas AW Bell, Christian R Engst, Marc Ablay, Giorgio Divitini, Caterina Ducati, Tim Liedl, and Ulrich F Keyser. Dna origami nanopores. *Nano letters*, 12(1):512–517, 2011.

[9] L Inge Berge, T Jossang, and Jens Feder. Off-axis response for particles passing through long apertures in coulter-type counters. *Measurement Science and Technology*, 1(6):471, 1990.

[10] Daniel Branton, David W Deamer, Andre Marziali, Hagan Bayley, Steven A Benner, Thomas Butler, Massimiliano Di Ventra, Slaven Garaj, Andrew Hibbs, Xiaohua Huang, et al. The potential and challenges of nanopore sequencing. *Nature biotechnology*, 26(10):1146–1153, 2008.

[11] Tom Z Butler, Mikhail Pavlenok, Ian M Derrington, Michael Niederweis, and Jens H Gundlach. Single-molecule dna detection with an engineered mspa protein nanopore. *Proceedings of the National Academy of Sciences*, 105(52):20647–20652, 2008.

[12] Sangwon Byun, Sungmin Son, Dario Amodei, Nathan Cermak, Josephine Shaw, Joon Ho Kang, Vivian C Hecht, Monte M Winslow, Tyler Jacks, Parag Mallick, et al. Characterizing deformability and surface friction of cancer cells. *Proceedings of the National Academy of Sciences*, 110(19):7580–7585, 2013.

[13] CELLSEARCH. Cellsearch — home. `https://www.cellsearchctc.com/`. (Visited on 09/05/2015).

[14] Chinhsuan Chen, Sukru Yemenicioglu, Ahsan Uddin, Ellie Corgliano, and Luke Theogarajan. A cmos enhanced solid-state nanopore based single molecule detection platform. In *Engineering in Medicine and Biology So-*

ciety (EMBC), 2013 35th Annual International Conference of the IEEE, pages 164–167. IEEE, 2013.

[15] Jian Chen, Yi Zheng, Qingyuan Tan, Ehsan Shojaei-Baghini, Yan Liang Zhang, Jason Li, Preethy Prasad, Lidan You, Xiao Yu Wu, and Yu Sun. Classification of cell types using a microfluidic device for mechanical and electrical measurement on single cells. *Lab on a Chip*, 11(18):3174–3181, 2011.

[16] Edward H Cho, Marco Wendel, Madelyn Luttgen, Craig Yoshioka, Dena Marrinucci, Daniel Lazar, Ethan Schram, Jorge Nieva, Lyudmila Bazhenova, Alison Morgan, et al. Characterization of circulating tumor cell aggregates identified in patients with epithelial tumors. *Physical biology*, 9(1):016001, 2012.

[17] John Chu, Marcos González-López, Scott L Cockroft, Manuel Amorin, and M Reza Ghadiri. Real-time monitoring of dna polymerase function and stepwise single-nucleotide dna strand translocation through a protein nanopore. *Angewandte Chemie*, 122(52):10304–10307, 2010.

[18] Igor Cima, Chay Wen Yee, Florina S Iliescu, Wai Min Phyo, Kiat Hon Lim, Ciprian Iliescu, and Min Han Tan. Label-free isolation of circulat-

ing tumor cells in microfluidic devices: Current research and perspectives. *Biomicrofluidics*, 7(1):011810, 2013.

[19] Scott L Cockroft, John Chu, Manuel Amorin, and M Reza Ghadiri. A single-molecule nanopore device detects dna polymerase activity with single-nucleotide resolution. *Journal of the American Chemical Society*, 130(3):818–820, 2008.

[20] SJ Cohen, CJA Punt, N Iannotti, BH Saidman, KD Sabbath, NY Gabrail, J Picus, MA Morse, E Mitchell, MC Miller, et al. Prognostic significance of circulating tumor cells in patients with metastatic colorectal cancer. *Annals of Oncology*, 20(7):1223–1229, 2009.

[21] FA Coumans, Guus van Dalum, Markus Beck, and LW Terstappen. Filter characteristics influencing circulating tumor cell enrichment from whole blood. *PloS one*, 8(4):e61770, 2013.

[22] Massimo Cristofanilli, G Thomas Budd, Matthew J Ellis, Alison Stopeck, Jeri Matera, M Craig Miller, James M Reuben, Gerald V Doyle, W Jeffrey Allard, Leon WMM Terstappen, et al. Circulating tumor cells, disease progression, and survival in metastatic breast cancer. *New England Journal of Medicine*, 351(8):781–791, 2004.

[23] Massimo Cristofanilli, Daniel F Hayes, G Thomas Budd, Mathew J Ellis, Alison Stopeck, James M Reuben, Gerald V Doyle, Jeri Matera, W Jeffrey Allard, M Craig Miller, et al. Circulating tumor cells: a novel prognostic factor for newly diagnosed metastatic breast cancer. *Journal of Clinical Oncology*, 23(7):1420–1430, 2005.

[24] Sarah E Cross, Yu-Sheng Jin, Jianyu Rao, and James K Gimzewski. Nanomechanical analysis of cells from cancer patients. *Nature nanotechnology*, 2(12):780–783, 2007.

[25] Sarah E Cross, Yu-Sheng Jin, Julianne Tondre, Roger Wong, JianYu Rao, and James K Gimzewski. Afm-based analysis of human metastatic cancer cells. *Nanotechnology*, 19(38):384003, 2008.

[26] Vincenzo De Giorgi, Pamela Pinzani, Francesca Salvianti, John Panelos, Milena Paglierani, Agata Janowska, Marta Grazzini, Janine Wechsler, Claudio Orlando, Marco Santucci, et al. Application of a filtration-and isolation-by-size technique for the detection of circulating tumor cells in cutaneous melanoma. *Journal of Investigative Dermatology*, 130(10):2440–2447, 2010.

[27] Ralph W Deblois, Charles P Bean, and Roy KA Wesley. Electrokinetic measurements with submicron particles and pores by the resistive pulse technique. *Journal of colloid and interface science*, 61(2):323–335, 1977.

[28] RW DeBlois and CP Bean. Counting and sizing of submicron particles by the resistive pulse technique. *Review of Scientific Instruments*, 41(7):909–916, 1970.

[29] Jaap den Toonder. Circulating tumor cells: the grand challenge. *Lab on a chip*, 11(3):375–377, 2011.

[30] Ian M Derrington, Tom Z Butler, Marcus D Collins, Elizabeth Manrao, Mikhail Pavlenok, Michael Niederweis, and Jens H Gundlach. Nanopore dna sequencing with mspa. *Proceedings of the National Academy of Sciences*, 107(37):16060–16065, 2010.

[31] Udara Dharmasiri, Samuel K Njoroge, Małgorzata A Witek, Morayo G Adebiyi, Joyce W Kamande, Mateusz L Hupert, Francis Barany, and Steven A Soper. High-throughput selection, enumeration, electrokinetic manipulation, and molecular profiling of low-abundance circulating tumor cells using a microfluidic system. *Analytical chemistry*, 83(6):2301–2309, 2011.

[32] Michael D Fischbein and Marija Drndić. Electron beam nanosculpting of suspended graphene sheets. *Applied Physics Letters*, 93(11):113107, 2008.

[33] Daniel Fologea, Eric Brandin, James Uplinger, Daniel Branton, and Jiali Li. Dna conformation and base number simultaneously determined in a nanopore. *Electrophoresis*, 28(18):3186, 2007.

[34] Slaven Garaj, W Hubbard, A Reina, J Kong, D Branton, and JA Golovchenko. Graphene as a subnanometre trans-electrode membrane. *Nature*, 467(7312):190–193, 2010.

[35] Elisabeth P Gates, Andrew M Dearden, and Adam T Woolley. Dna-templated lithography and nanofabrication for the fabrication of nanoscale electronic circuitry. *Critical Reviews in Analytical Chemistry*, 44(4):354–370, 2014.

[36] Helen Gogas, AMM Eggermont, Axel Hauschild, Peter Hersey, P Mohr, Dirk Schadendorf, Alan Spatz, and Reinhard Dummer. Biomarkers in melanoma. *Annals of Oncology*, 20(suppl 6):vi8–vi13, 2009.

[37] DC Golibersuch. Observation of aspherical particle rotation in poiseuille flow via the resistance pulse technique: I. application to human erythrocytes. *Biophysical journal*, 13(3):265, 1973.

[38] Daniel R Gossett, Westbrook M Weaver, Albert J Mach, Soojung Claire Hur, Henry Tat Kwong Tse, Wonhee Lee, Hamed Amini, and Dino Di Carlo. Label-free cell separation and sorting in microfluidic systems. *Analytical and bioanalytical chemistry*, 397(8):3249–3267, 2010.

[39] Eo C Gregg and K David Steidley. Electrical counting and sizing of mammalian cells in suspension. *Biophysical journal*, 5(4):393–405, 1965.

[40] Rizal F Hariadi and Bernard Yurke. Elongational-flow-induced scission of dna nanotubes in laminar flow. *Physical Review E*, 82(4):046307, 2010.

[41] David P Hoogerheide, Slaven Garaj, and Jene A Golovchenko. Probing surface charge fluctuations with solid-state nanopores. *Physical review letters*, 102(25):256804, 2009.

[42] Han Wei Hou, Majid Ebrahimi Warkiani, Bee Luan Khoo, Zi Rui Li, Ross A Soo, Daniel Shao-Weng Tan, Wan-Teck Lim, Jongyoon Han, Ali Asgar S Bhagat, and Chwee Teck Lim. Isolation and retrieval of circulating tumor cells using centrifugal forces. *Scientific reports*, 3, 2013.

[43] Shuang Hou, Libo Zhao, Qinglin Shen, Juehua Yu, Charles Ng, Xiangju Kong, Dongxia Wu, Min Song, Xiaohong Shi, Xiaochun Xu, et al. Polymer nanofiber-embedded microchips for detection, isolation, and molecular analysis of single circulating melanoma cells. *Angewandte Chemie International Edition*, 52(12):3379–3383, 2013.

[44] David W Inglis, Robert Riehn, RH Austin, and JC Sturm. Continuous microfluidic immunomagnetic cell separation. *Applied Physics Letters*, 85(21):5093–5095, 2004.

[45] Laura M Innes, Chin-Hsuan Chen, Matthew Schiel, Matthew Pevarnik, Florian Haurais, Maria Eugenia Toimil-Molares, Ivan Vlassiouk, Luke Theog-

arajan, and Zuzanna S Siwy. Velocity profiles in pores with undulating opening diameter and their importance for resistive-pulse experiments. *Analytical chemistry*, 86(20):10445–10453, 2014.

[46] Ashish V Jagtiani, Joan Carletta, and Jiang Zhe. An impedimetric approach for accurate particle sizing using a microfluidic coulter counter. *Journal of Micromechanics and Microengineering*, 21(4):045036, 2011.

[47] Ashish V Jagtiani, Joan Carletta, and Jiang Zhe. A microfluidic multichannel resistive pulse sensor using frequency division multiplexing for high throughput counting of micro particles. *Journal of Micromechanics and Microengineering*, 21(6):065004, 2011.

[48] Mette Jepsen, Rasmus S Sørensen, Ebbe S Andersen, Jørgen Kjems, and Victoria Birkedal. Single molecule fret analysis of the closed and open states of a dna origami box. *Biophysical Journal*, 108(2):175a, 2015.

[49] Erika Jonietz. Mechanics: The forces of cancer. *Nature*, 491(7425):S56–S57, 2012.

[50] Giorgos Karakousis, Ruifeng Yang, and Xiaowei Xu. Circulating melanoma cells as a predictive biomarker. *Journal of Investigative Dermatology*, 133(6):1460–1462, 2013.

[51] John J Kasianowicz, Eric Brandin, Daniel Branton, and David W Deamer. Characterization of individual polynucleotide molecules using a membrane channel. *Proceedings of the National Academy of Sciences*, 93(24):13770–13773, 1996.

[52] Ryuji Kawano, Toshihisa Osaki, Hirotaka Sasaki, and Shoji Takeuchi. A polymer-based nanopore-integrated microfluidic device for generating stable bilayer lipid membranes. *Small*, 6(19):2100–2104, 2010.

[53] Brian J Kirby, Mona Jodari, Matthew S Loftus, Gunjan Gakhar, Erica D Pratt, Chantal Chanel-Vos, Jason P Gleghorn, Steven M Santana, He Liu, James P Smith, et al. Functional characterization of circulating tumor cells with a prostate-cancer-specific microfluidic device. *PloS one*, 7(4):e35976, 2012.

[54] Jim Kling. Beyond counting tumor cells. *Nature biotechnology*, 30(7):578–580, 2012.

[55] Stefan W Kowalczyk, Alexander Y Grosberg, Yitzhak Rabin, and Cees Dekker. Modeling the conductance and dna blockade of solid-state nanopores. *Nanotechnology*, 22(31):315101, 2011.

[56] Akinori Kuzuya and Yuichi Ohya. Nanomechanical molecular devices made of dna origami. *Accounts of chemical research*, 47(6):1742–1749, 2014.

[57] Kate R Lieberman, Gerald M Cherf, Michael J Doody, Felix Olasagasti, Yvette Kolodji, and Mark Akeson. Processive replication of single dna molecules in a nanopore catalyzed by phi29 dna polymerase. *Journal of the American Chemical Society*, 132(50):17961–17972, 2010.

[58] Jie Liu, Radoslaw Bombera, Loïc Leroy, Yoann Roupioz, Dieudonné R Baganizi, Patrice N Marche, Vincent Haguet, Pascal Mailley, and Thierry Livache. Selective individual primary cell capture using locally bio-functionalized micropores. *PloS one*, 8(3):e57717, 2013.

[59] Pik Kwan Lo, Kimberly L Metera, and Hanadi F Sleiman. Self-assembly of three-dimensional dna nanostructures and potential biological applications. *Current opinion in chemical biology*, 14(5):597–607, 2010.

[60] Elizabeth A Manrao, Ian M Derrington, Andrew H Laszlo, Kyle W Langford, Matthew K Hopper, Nathaniel Gillgren, Mikhail Pavlenok, Michael Niederweis, and Jens H Gundlach. Reading dna at single-nucleotide resolution with a mutant mspa nanopore and phi29 dna polymerase. *Nature biotechnology*, 30(4):349–353, 2012.

[61] Elizabeth A Manrao, Ian M Derrington, Mikhail Pavlenok, Michael Niederweis, and Jens H Gundlach. Nucleotide discrimination with dna immobilized in the mspa nanopore. *PLoS One*, 6(10):e25723, 2011.

[62] Dena Marrinucci, Kelly Bethel, Anand Kolatkar, Madelyn S Luttgen, Michael Malchiodi, Franziska Baehring, Katharina Voigt, Daniel Lazar, Jorge Nieva, Lyudmila Bazhenova, et al. Fluid biopsy in patients with metastatic prostate, pancreatic and breast cancers. *Physical biology*, 9(1):016003, 2012.

[63] James Clerk Maxwell. *A treatise on electricity and magnetism*, volume 1. Clarendon press, 1881.

[64] Christopher A Merchant, Ken Healy, Meni Wanunu, Vishva Ray, Neil Peterman, John Bartel, Michael D Fischbein, Kimberly Venta, Zhengtang Luo, AT Charlie Johnson, et al. Dna translocation through graphene nanopores. *Nano letters*, 10(8):2915–2921, 2010.

[65] Mirna Mihovilovic, Nicholas Hagerty, and Derek Stein. Statistics of dna capture by a solid-state nanopore. *Physical review letters*, 110(2):028102, 2013.

[66] U Mirsaidov, Winston Timp, Xueqing Zou, Valentin Dimitrov, K Schulten, Andrew P Feinberg, and G Timp. Nanoelectromechanics of methylated dna in a synthetic nanopore. *Biophysical journal*, 96(4):L32–L34, 2009.

[67] Jose G Moreno, M Craig Miller, Steve Gross, W Jeffrey Allard, Leonard G Gomella, and Leon WMM Terstappen. Circulating tumor cells predict sur-

vival in patients with metastatic prostate cancer. *Urology*, 65(4):713–718, 2005.

[68] Danielle Morton, Shahab Mortezaei, Sukru Yemenicioglu, Michael J Isaacman, Ian C Nova, Jens H Gundlach, and Luke Theogarajan. Tailored polymeric membranes for mycobacterium smegmatis porin a (mspa) based biosensors. *Journal of Materials Chemistry B*, 2015.

[69] Sunitha Nagrath, Lecia V Sequist, Shyamala Maheswaran, Daphne W Bell, Daniel Irimia, Lindsey Ulkus, Matthew R Smith, Eunice L Kwak, Subba Digumarthy, Alona Muzikansky, et al. Isolation of rare circulating tumour cells in cancer patients by microchip technology. *Nature*, 450(7173):1235–1239, 2007.

[70] John S Oliver and John Thompson. Method and system for analysis of protein and other modifications on dna and rna, September 25 2013. US Patent App. 14/036,509.

[71] Patrick O'Neill, Paul WK Rothemund, Ashish Kumar, and D Kuchnir Fygenson. Sturdier dna nanotubes via ligation. *Nano letters*, 6(7):1379–1383, 2006.

[72] Toshihisa Osaki, Hiroaki Suzuki, Bruno Le Pioufle, and Shoji Takeuchi. Multichannel simultaneous measurements of single-molecule translocation

in α-hemolysin nanopore array. *Analytical chemistry*, 81(24):9866–9870, 2009.

[73] Oliver Otto, Philipp Rosendahl, Alexander Mietke, Stefan Golfier, Christoph Herold, Daniel Klaue, Salvatore Girardo, Stefano Pagliara, Andrew Ekpenyong, Angela Jacobi, et al. Real-time deformability cytometry: on-the-fly cell mechanical phenotyping. *Nature methods*, 2015.

[74] Klaus Pantel, Ruud H Brakenhoff, and Burkhard Brandt. Detection, clinical relevance and specific biological properties of disseminating tumour cells. *Nature Reviews Cancer*, 8(5):329–340, 2008.

[75] Ashley A Powell, AmirAli H Talasaz, Haiyu Zhang, Marc A Coram, Anupama Reddy, Glenn Deng, Melinda L Telli, Ranjana H Advani, Robert W Carlson, Joseph A Mollick, et al. Single cell profiling of circulating tumor cells: transcriptional heterogeneity and diversity from breast cancer cell lines. *PloS one*, 7(5):e33788, 2012.

[76] Zhenpeng Qin, Jiang Zhe, and Guo-Xiang Wang. Effects of particle's off-axis position, shape, orientation and entry position on resistance changes of micro coulter counting devices. *Measurement Science and Technology*, 22(4):045804, 2011.

[77] Lord Rayleigh. Lvi. on the influence of obstacles arranged in rectangular order upon the properties of a medium. *The London, Edinburgh, and Dublin Philosophical Magazine and Journal of Science*, 34(211):481–502, 1892.

[78] OA Saleh and LL Sohn. Correcting off-axis effects in an on-chip resistive-pulse analyzer. *Review of scientific instruments*, 73(12):4396–4398, 2002.

[79] E Samson, J Marchand, and KA Snyder. Calculation of ionic diffusion coefficients on the basis of migration test results. *Materials and Structures*, 36(3):156–165, 2003.

[80] Grégory F Schneider, Stefan W Kowalczyk, Victor E Calado, Grégory Pandraud, Henny W Zandbergen, Lieven MK Vandersypen, and Cees Dekker. Dna translocation through graphene nanopores. *Nano letters*, 10(8):3163–3167, 2010.

[81] Eric R. Schuur. www.screencell.com/wp-content/uploads/2013/01/screencell-white-paper.pdf. `http://www.screencell.com/wp-content/uploads/2013/01/ScreenCell-White-Paper.pdf`. (Visited on 09/05/2015).

[82] Jiwook Shim, Gwendolyn I Humphreys, Bala Murali Venkatesan, Jan Marie Munz, Xueqing Zou, Chaitanya Sathe, Klaus Schulten, Farhad Kosari,

Ann M Nardulli, George Vasmatzis, et al. Detection and quantification of methylation in dna using solid-state nanopores. *Scientific reports*, 3, 2013.

[83] Ralph MM Smeets, Ulrich F Keyser, Diego Krapf, Meng-Yue Wu, Nynke H Dekker, and Cees Dekker. Salt dependence of ion transport and dna translocation through solid-state nanopores. *Nano Letters*, 6(1):89–95, 2006.

[84] WR Smythe. Flow around a sphere in a circular tube. *Physics of Fluids (1958-1988)*, 4(6):756–759, 1961.

[85] WR Smythe. Flow around a spheroid in a circular tube. *Physics of Fluids (1958-1988)*, 7(5):633–638, 1964.

[86] Reimar Spohr. *Ion tracks and microtechnology: principles and applications.* Reimar Spohr, 1990.

[87] Shawn Steen, John Nemunaitis, Tammy Fisher, and Joseph Kuhn. Circulating tumor cells in melanoma: a review of the literature and description of a novel technique. *Proceedings (Baylor University. Medical Center)*, 21(2):127, 2008.

[88] Subra Suresh. Biomechanics and biophysics of cancer cells. *Acta Materialia*, 55(12):3989–4014, 2007.

[89] Vinay Swaminathan, Karthikeyan Mythreye, E Tim O'Brien, Andrew Berchuck, Gerard C Blobe, and Richard Superfine. Mechanical stiffness grades metastatic potential in patient tumor cells and in cancer cell lines. *Cancer research*, 71(15):5075–5080, 2011.

[90] AmirAli H Talasaz, Ashley A Powell, David E Huber, James G Berbee, Kyung-Ho Roh, Wong Yu, Wenzhong Xiao, Mark M Davis, R Fabian Pease, Michael N Mindrinos, et al. Isolating highly enriched populations of circulating epithelial cells and other rare cells from blood using a magnetic sweeper device. *Proceedings of the National Academy of Sciences*, 106(10):3970–3975, 2009.

[91] Makusu Tsutsui, Sakon Rahong, Yoko Iizumi, Toshiya Okazaki, Masateru Taniguchi, and Tomoji Kawai. Single-molecule sensing electrode embedded in-plane nanopore. *Scientific reports*, 1, 2011.

[92] Makusu Tsutsui, Masateru Taniguchi, Kazumichi Yokota, and Tomoji Kawai. Identifying single nucleotides by tunnelling current. *Nature nanotechnology*, 5(4):286–290, 2010.

[93] A Uddin, S Yemenicioglu, CH Chen, E Corigliano, K Milaninia, and L Theogarajan. Integration of solid-state nanopores in a 0.5 μm cmos foundry process. *Nanotechnology*, 24(15):155501, 2013.

[94] Ashfaque Uddin, Chin-Hsuan Chen, Sukru Yemenicioglu, Kaveh Milaninia, Ellie Corigliano, Madoo Varma, and Luke Theogarajan. Integrated nanopore detectors in a standard complementary metal-oxide-semiconductor process. In *APS Meeting Abstracts*, volume 1, page 50001, 2012.

[95] Ashfaque Uddin, Sukru Yemenicioglu, Chin-Hsuan Chen, Ellie Corgliano, Kaveh Milaninia, Fan Xia, Kevin Plaxco, and Luke Theogarajan. Biosensing with integrated cmos nanopores. In *SPIE NanoScience+ Engineering*, pages 846010–846010. International Society for Optics and Photonics, 2012.

[96] Anja Ulmer, Oleg Schmidt-Kittler, Jörg Fischer, Ulf Ellwanger, Gernot Rassner, Gert Riethmüller, Gerhard Fierlbeck, and Christoph A Klein. Immunomagnetic enrichment, genomic characterization, and prognostic impact of circulating melanoma cells. *Clinical Cancer Research*, 10(2):531–537, 2004.

[97] Meni Wanunu. Nanopores: A journey towards dna sequencing. *Physics of life reviews*, 9(2):125–158, 2012.

[98] Tatsuro Watanabe, Hiromi Kuramochi, Atsushi Takahashi, Kazue Imai, Naoko Katsuta, Tomonobu Nakayama, Hirota Fujiki, and Masami Suganuma. Higher cell stiffness indicating lower metastatic potential in b16

melanoma cell variants and in (-)-epigallocatechin gallate-treated cells. *Journal of cancer research and clinical oncology*, 138(5):859–866, 2012.

[99] Denis Wirtz, Konstantinos Konstantopoulos, and Peter C Searson. The physics of cancer: the role of physical interactions and mechanical forces in metastasis. *Nature Reviews Cancer*, 11(7):512–522, 2011.

[100] Wenwei Xu, Roman Mezencev, Byungkyu Kim, Lijuan Wang, John McDonald, and Todd Sulchek. Cell stiffness is a biomarker of the metastatic potential of ovarian cancer cells. *PloS one*, 7(10):e46609, 2012.

[101] Peng Yin, Rizal F Hariadi, Sudheer Sahu, Harry MT Choi, Sung Ha Park, Thomas H LaBean, and John H Reif. Programming dna tube circumferences. *Science*, 321(5890):824–826, 2008.

[102] Jiang Zhe, Ashish Jagtiani, Prashanta Dutta, Jun Hu, and Joan Carletta. A micromachined high throughput coulter counter for bioparticle detection and counting. *Journal of Micromechanics and Microengineering*, 17(2):304, 2007.

Appendix A

Glossary

10HT DNA: 10-Helix DNA nanotube

1165: Photoresist remover

AZ300mif: Photoresist developer

AZ400K: Photoresist developer

ALD: Atomic layer deposition

AZnLOF2020: Negative photoresist

AZnLOF2070: Negative photoresist

AZP4110: Positive photo resist

bp: basepair

Bosch process: Plasma etching consisting of passivation and etch cycles. It ensures higher aspect ratio features

CIS: The chamber where the investigated sample is added.

CMC: Circulating melanoma cell

CMOS: Complementary Metal Oxide Semiconductor

CTC: Circulating tumor cell

DI: Deionized water

DRIE: Deep reactive ion etching

dsDNA: Double stranded DNA

ECD: Event charge deficit

Ellipsometer: Film thickness measurement device

EMT: Epithelialmesenchymal transition

EpCAM: Epithelial cell adhesion molecule

ICP RIE: Inductively coupled plasma reactive ion etching

MCF7: Breast cancer cell

MNT1: Skin cancer cell, melanoma.

PECVD: Plasma enhanced chemical vapor deposition

PR: Photoresist

SEM: Scanning electron microscope

ssDNA: Single stranded DNA

TEM: Transmission electron microscope

TEM Grid: Chips made for TEM inspection

TRANS: The chamber where the investigated sample arrives after passing through the pore.

translocation: The passage of DNA from CIS to TRANS chamber.

Appendix B

Matlab Algorithms

List of functions: eventstats

findbaseline

findextrema

translocations

```
%This is an algorithm that detects enhancement and blockage pulses. It is
%able to recursively enter into long segments of events and analyzes them
%as new data spans. Sukru Yemenicioglu 08/23/2015

%Variable list:
%Input Variables%%%%%%
%time: 1D array. needs to be in milliseconds
%data: 1D array. can be Amps or nanoamps, does not matter
%level: Tracks the nesting level inside events.
%Output Variable
%events: the avariable that stores all the pulse statistics

function[events] = eventstats(time, data, level)
%events variable is the array that all the statistics are recorded
events=[];
lofdata=length(data);

i=1;

%span variable determines the window size for moving average filter while
%calcualting the baseline. If the number of data points are above 100k, the
%span length is 10k. Otherwise, it is 1k.

span=1000;

if(lofdata>100000)
    span=10000;
end

%findbaseline function calculates the baseline, filtered data for long
%events, threshold for long events and threshold for short events.

tic%Tracks the amount of time it takes to calculate the baseline
[baseline slowline threshold1 threshold2]=findbaseline(data,span);
toc

% Gathers all the data points above/below short events threshold
temp=[];
peak_locs=find(abs(data-baseline)>threshold1);
temp(1:length(peak_locs),1 )=1;
peak_locs=[peak_locs temp];
temp=[];
% Gathers all the data points above/below long events threshold
% the second column in peak_temp marks which threshold the data points
% crossed. The second threshold has priority over the short event threshold
peak_temp=find(abs(slowline-baseline)>threshold2);
temp(1:length(peak_temp),1)=2;
peak_temp=[peak_temp temp];
clear temp;

% Merges the data points for long event and short event thresholds
peak_locs=sortrows(peak_locs);
peak_locs=[peak_locs; peak_temp];
[temp ind]=unique(peak_locs(:,1));
peak_locs=peak_locs(ind,:);
clear temp;
```

```
clear peak_temp;

% In order to track long events filtered data is added as a second column
% to the data. It allows to refer to it in the same loop for finding the
% events
data=[data slowline];

clear slowline;

if(isempty(peak_locs))
        return;
end

lofpeak_locs=length(peak_locs(:,1)); %

start_sample = 1;

estart = peak_locs(start_sample,1); % event start index variable
eend = peak_locs(start_sample,1); % event end index variable
%-------------------------------------------
i=1;

% The loop that traverses the data for all the enhancement and blocakge
% events
while i<lofpeak_locs
    tempevents=[];

    % Determines if it is an enhancement or blockage event
    % type=1 is enhancement event
    if(data(peak_locs(i,1), peak_locs(i,2))>baseline(peak_locs(i,1)))
        type=1;

        a=0;
        % Finds the beginning of the event. Traces the data points backward↙
until it
        % comes back to the baseline.
        while data(peak_locs(i,1)-a,peak_locs(i,2))>((baseline(peak_locs(i,↙
1)-a)))
            a=a+1;
            if((peak_locs(i,1)-a) < 1)
                   break
            end
        end

        estart=peak_locs(i,1)-(a-1);

        a=0;
        b=1;
        % Finds the last data point above the threshold. If there is
        % another event that is nearer than 1000 indices, it considers it↙
part of the same event.
        while ((peak_locs(i+b,1)-peak_locs(i+b-1,1))<1000)
            b=b+1;
            if(((i+b) > lofpeak_locs))
                   break
            end
```

```
        end

        b=b-1;
        % Finds end of the event. Traces the data points forward until it
        % comes back to the baseline.
        while data(peak_locs(i+b,1)+a,peak_locs(i+b,2) )>(baseline↙
((peak_locs(i+b,1)+a)))
            a=a+1;
            if((peak_locs(i+b,1)+a) > lofdata)
                   break
            end
        end

        eend=peak_locs(i+b,1)+(a-1);

    else
        % blockage event calculations. type=2
        type=2;

        a=0;
        % Finds the beginning of the event. Traces the data points backward↙
until it
        % comes back to the baseline.
        while data(peak_locs(i,1)-a,peak_locs(i,2))<((baseline(peak_locs(i,↙
1)-a)))
            a=a+1;
            if((peak_locs(i,1)-a) < 1)
                   break
            end
        end

        estart=peak_locs(i,1)-(a-1);

        a=0;
        b=1;
        % Finds the last data point above the threshold. If there is
        % another event that is nearer than 1000 indices, it considers it
        % part of the same event.
        while ((peak_locs(i+b,1)-peak_locs(i+b-1,1))<1000)
            b=b+1;
            if(((i+b) > lofpeak_locs))
                   break
            end
        end

        b=b-1;
        % Finds end of the event. Traces the data points forward until it
        % comes back to the baseline.
        while data(peak_locs(i+b,1)+a,peak_locs(i+b,2) )<(baseline↙
((peak_locs(i+b,1)+a)))
            a=a+1;
            if((peak_locs(i+b,1)+a) > lofdata)
                   break
            end
        end
```

```
        eend=peak_locs(i+b,1)+(a-1);

    end
    % updates the index tracking variable, i. If there is an event before
    % 1000 index points it ignores it. This is handy for ripples after
    % large events.
    while( peak_locs(i,1)<= (eend+1000))
    i=i+1;
        if(i>lofpeak_locs)
            break
        end
    end

    % based on the indices the corresponding event start and end time.
    estartt=time(estart);
    eendt=time(eend);
    dur=eendt-estartt;

    % if the event is shorter than the bandwidth allows skip the event
    if(dur<(1/15))
        continue
    end

    % integrates the charge in the event
    totalcharge=1e-9.*sum(data(estart:eend,1)-baseline(estart:eend)).*(time↙
(2)-time(1))./1e6./1.6e-19; %in ke

    % baseline of the event
    ebaseline=mean(baseline(estart:eend));
    eavg=100*(mean(data(estart:eend,1))-ebaseline)/ebaseline;

    if(type==1)
        ratio=100*(max(data(estart:eend,1))-ebaseline)/ebaseline;
    else
        ratio=100*(min(data(estart:eend,1))-ebaseline)/ebaseline;
    end

    try
        if((eend-estart)>20000)
            tempevents=eventstats(time(estart:eend), data(estart:eend,1),↙
level+1);
        end
    end

    % Stores all the statistics in the same variable.
    events=[events; tempevents; level type estartt eendt dur ebaseline eavg↙
ratio totalcharge];

end
```

```
% This is the function that finds the baseline. It makes histogram of all
% data points and fits gaussian distributions over it. The most prominent
% peak is considered to be associated with the baseline. If the number of
% data points are over 200k, the user is asked to intervene to adjust the
% parameters.  Sukru Yemenicioglu 08/23/2015

% Variable List:
% data: the set of data to be analyzed
% span: determines the
function[baseline slowline threshold1 threshold2]=findbaseline(data, span)

% verysmooth is an updated version of the smooth function built-in matlab.
% It runs a lot faster.
tempbaseline=verysmooth(data,span);

%Makes a histogram of the smoothed data
[counts bins]=hist(tempbaseline,span/5);

offset=bins(find(counts==max(counts)));

%sets up the parameters for a gaussian fit
lower=[0 offset*0.5 0 ];
upper=[max(counts) offset*1.5 offset*0.5];
startpoint=[max(counts)/2 offset offset/100];

s = fitoptions('Method','NonlinearLeastSquares',...
'Lower',lower,...
'Upper',upper,...
'Startpoint',startpoint,...
'MaxIter',1e8,...
'TolFun',1e-6,...
'TolX',1e-6,...
'MaxFunEvals',1e4,...
'DiffMinChange',1e-8,...
'DiffMaxChange',1e-1,...
'Robust', 'On');

f=fittype('c1*exp(-((x-u1)^2)/(2*s1^2))', 'independent', 'x',↙
'coefficients',['c1'; 'u1'; 's1'], 'options', s);

%fits the guassian distribution on the curve
[fitobj j]=fit(bins',counts',f);

coeff=[fitobj.c1 fitobj.u1 fitobj.s1];

%if the data points are more than 200000, it asks to user to confirm the
%fit
if(length(data)>200000)
    close all;
    figure(10)
    plot(bins, counts);
    hold on
    plot(bins,fitobj.c1.*exp(-((bins-fitobj.u1).^2)./(2.*fitobj.s1^2)),↙
'g');
    hold off
    ok=input('If it looks good enter 1:\n');
```

```
else
    ok=1;
end


%When the user wants to intervene the  algorithm asks the locations of the↙
peaks
% ok=1;
while(ok~=1)

   params=input('Please enter the peak locations as in the following↙
format: i.e. [ 0.035; 0.051; 0.063]\nPeak Locations:\n');
   numofgauss=length(params(:,1));

    formula=[];
    lower=[];
    upper=[];
    startpoint=[];
    legendvals=cellstr('hist');


    % Based on the number of peaks the algorithm sets up a formula with the
    % appropriate number of guassian distributions
    for i=1:numofgauss
        legendvals=[legendvals num2str(i)];

        if (i==1)
            coeff=cellstr([['c' num2str(i)]; ['u' num2str(i)]; ['s' num2str↙
(i)]]);
        else
            coeff=[coeff; ['c' num2str(i)]; ['u' num2str(i)]; ['s' num2str↙
(i)]];
            formula=[formula '+'];
        end

        formula=[formula 'c' num2str(i) '*exp(-((x-u' num2str(i) ')^2)/↙
(2*s' num2str(i) '^2))'];
        lower=[lower 0 params(i,1)*0.5 0 ];
        upper=[upper max(counts) params(i,1)*1.5 params(i,1)*0.5];
        startpoint=[startpoint max(counts)/2 params(i,1) params(i,2)];

    end

    %fit alogrithm parameters
    s = fitoptions('Method','NonlinearLeastSquares',...
        'TolFun',1e-6,...
        'TolX',1e-6,...
        'MaxFunEvals',1e6,...
        'DiffMinChange',1e-8,...
        'MaxIter',1e4,...
        'Robust', 'On',...
        'Lower',lower,...
        'Upper',upper,...
        'Startpoint',startpoint);

    f=fittype(formula, 'independent', 'x', 'coefficients',coeff, 'options',↙
```

```
s);

    [fitobj j]=fit(bins',counts',f)

    subplot(2,1,1)
    plot(bins, counts);
    hold on;
    fitvals=coeffvalues(fitobj);

    plotcolors=['k' 'g' 'm' 'c' 'y' 'r'];

    for i=1:numofgauss
        tempvals=fitvals((3*(i-1)+1):(3*(i-1)+3));
        tempy=tempvals(1).*exp(-((bins-tempvals(2)).^2)./(2.*tempvals(3).↙
^2));
        plot(bins, tempy, plotcolors(1+mod(i,6)));
    end

    legend(legendvals);
    hold off

    % Plots the downsampled data
    subplot(2,1,2)
    plot(downsample(data,30), 'linewidth',2)

    ok=input('If it looks good enter the peak:\n');


    if(ok>0)
        coeff=fitvals((3*(ok-1)+1):(3*(ok-1)+3));
        ok=1;
    elseif(ok==-1)
        ok=1;
        coeff=fitvals((3*(ok-1)+1):(3*(ok-1)+3));
        coeff(3)=input('Enter the threshold:\n')/4;
        if(input('Do you want to enter the baseline?:\n'))
            coeff(2)=input('Enter the baseline:\n');
        end
    end

end

newdata=data;

map=[find(tempbaseline>(coeff(2)+coeff(3)*2)); find(tempbaseline<(coeff(2)-↙
coeff(3)*2))];
map=sort(map);

newdata(map)=coeff(2);
invmap=1:length(data);
invmap(map)=[];

% thresholds are set according the standard deviations of the gaussian fit
% for the long events. THe
% distributions and data without events.
threshold1=std(data(invmap))*4;
```

```
threshold2=coeff(3)*4;

baseline=verysmooth(newdata,span);
slowline=verysmooth(data,span);
```

```
% The algorithm finds the extrema and inflection points for 3 peaks and 2
% troughs. Sukru Yemenicioglu

% Variable list:
%Input variables:
%time: 1D array in milliseconds
%data: 1D array
%dataraw: unfiltered data
%baseline: calculated reference level from the main function
%makeplot: Activation of this variable allows the user to select the events
%manually
%Output variables:
%skip: If the event has more peaks than expected it gives a signal for the
%main function to not place it in the events array
%extrematime: Time stamps of local minimum and maximums
%extremavals: Magnitude values for local minimum and maximums
%transitiontime: Time stamps of inflection points between local extrema
%transitionvals: Magnitude values of inflection points between local
%extrema
%spheretime: Not used
%sphereval: Not used

function[skip extrematime extremavals transitiontime transitionvals↙
spheretime sphereval]=findextrema(time, data, dataraw, baseline, makeplot)

                    extrematime(1:5,1)=-1;
                    extremavals(1:5,1)=-1;
                    transitiontime(1:6,1)=-1;
                    transitionvals(1:6,1)=-1;
                    spheretime=-1;
                    sphereval=-1;
                    skip=-1;

                    if(length(data)<75)
                        return
                    end

                    datao=data;
                    data=verysmooth(data,20);

                    % takes the 1st derivative of the data and smooths it
                    d1data=diff(data);
                    d1data=verysmooth(d1data,50);
                    d1data=abs(d1data)-max(abs(d1data))*0.05;
                    meand1data=max(d1data)/3;
                    d2data=verysmooth(diff(diff(data)),50);
                    threshold(1:length(d1data))=meand1data;

                    index1=1;
                    index2=1;
                    transitionind=[];
                    extremaind=[];

                    % Check the length of the event
                    if((time(end)-time(1))<50)
                        %The loop that finds the transition points between
```

```
                        %extrema
                        while(index2<length(time)-2)
                            index1=min(find(d1data(index1:end)>0))+index1;
                            index2=min(find(d1data(index1:end)<0))+index1;
                            if(isempty(index2) || index2>length(d1data))
                                index2=length(d1data);
                            end

                            transitionind=[transitionind; max(d1data↙
(index1:index2)) find(d1data(index1:index2)==max(d1data(index1:index2)))↙
+index1];

                            index1=index2;
                        end

                        sortedtransitionind=sort(transitionind(:,↙
1),'descend');

                        try
                            transitionind=transitionind(find(transitionind↙
(:,1)>=sortedtransitionind(6)),2);
                        catch
                            transitionind=transitionind(:,2);
                        end

                        % The loop that find the extrema based on the
                        % transition points
                        for i=1:(length(transitionind)-1)

                              i1=transitionind(i);
                              i2=transitionind(i+1);

                              templine=data(i1)+((data(i2)-data(i1))/(i2-↙
i1)).*(0:(i2-i1));


                              if(length(find((data(i1:i2)-templine')>0))>↙
((i2-i1)/2))
                                  extremaind=[extremaind; find(data(i1:i2)↙
==max(data(i1:i2)))+i1];
                              else

                                  extremaind=[extremaind; find(data(i1:i2)↙
==min(data(i1:i2)))+i1];
                              end

                        end

                        try
                            sphereind=round(transitionind(2)-(transitionind↙
(2)-extremaind(1))*0.45);
                            spheretime=time(sphereind)-time(1);
                            sphereval=data(sphereind)/baseline;
                        catch
                            sphereind=-1;
                            sphereval=-1;
```

```
                            spheretime=-1;
                            return
                        end

                        if(~isempty(extremaind) && extremaind(end)>length↙
(time))
                            extremaind(end)=length(time);
                        end

                        if(length(extremaind)~=5 && length(transitionind)↙
~=6)
                            return
                        end

                        %plots the event and gives to option to choose to
                        %keep the event.
                        if(makeplot==1)
                            subplot(3,1,1)
                            plot(time,dataraw,'c', 'linewidth', 2);
                            hold on
                            plot(time,datao,'b', 'linewidth', 2);
                            h1=plot(time(transitionind), datao↙
(transitionind), '.g', 'linewidth',2);
                            h2=plot(time(extremaind), datao(extremaind), '.↙
k', 'linewidth',2);
                            h3=plot(time(sphereind),datao(sphereind),'.↙
m','linewidth',2);

                            set(h1,{'markers'},{20})
                            set(h2,{'markers'},{20})
                            set(h3,{'markers'},{20})

                            box on
                            xlabel('Time(ms)', 'Fontsize', 16);
                            ylabel('Current(nA)', 'Fontsize', 16);
                            set(gca,'FontSize',16, 'linewidth', 2);

                            hold off
                            subplot(3,1,2)
                            plot(time(2:end),d1data, 'linewidth', 2);


                            box on
                            xlabel('Time(ms)', 'Fontsize', 16);
                            ylabel('| 1^{st} Derivative |', 'Fontsize',↙
16);
                            set(gca,'FontSize',16, 'linewidth', 2);


                            subplot(3,1,3)
                            plot(time(3:end),d2data, 'linewidth', 2)

                            box on
                            xlabel('Time(ms)', 'Fontsize', 16);
                            ylabel('2^{nd} Derivative', 'Fontsize', 16);
                            set(gca,'FontSize',16, 'linewidth', 2);
```

```
                            set(gcf, 'Units', 'pixels');
                            set(gcf, 'OuterPosition', [0,0,1000, 1000])

                            ok=0;
                            while(ok==0)
                                try
                                    skip=input('To keep the event enter↙
"1":');

                                    if(isnumeric(skip) && skip~=-1)
                                        ok=1;
                                    end
                                end
                            end

                        end

                    end
                    %if the number of extrema is higher than expected, it↙
sets them to
                    %expected number of peaks
                    if(length(transitionind)>6)
                        transitiontime(1:6,1)=time(transitionind(1:6),1)-↙
time(1);
                        transitionvals(1:6,1)=datao(transitionind(1:6),1)↙
/baseline;
                    else
                        transitiontime(1:length(transitionind))=time↙
(transitionind)-time(1);
                        transitionvals(1:length(transitionind))=datao↙
(transitionind)/baseline;
                    end

                    if(length(extremaind)>5)
                        extrematime(1:5,1)=time(extremaind(1:5),1)-time(1);
                        extremavals(1:5,1)=datao(extremaind(1:5),1)↙
/baseline;
                    else
                        extrematime(1:length(extremaind))=time(extremaind)-↙
time(1);
                        extremavals(1:length(extremaind))=datao(extremaind)↙
/baseline;
                    end
```

```
% Translocation v1.1
% It can also analyze regular heka files( not clogprot) 08/25/2014
% function [void] = translocations(system,folder,threshold,samplingrate,↙
filter,isblockage);

function [void] = translocations(system,folder,threshold,samplingrate,↙
filter,isblockage, findext, plotevent)

% translocations(system,folder,threshold,samplingrate,filter,isblockage);

cd(char(folder));
names=dir;
lofnames=length(names);
cd ..
SR=samplingrate;

if(isblockage==1)
    type='block';
else
    type='enhance';
    if(strcmp('jenset', system))
        disp('Error: Jenset does not produce enhancement events')
        return
    end
end

confilename=[char(system) '_' char(folder) '_SR' num2str(samplingrate/1000)↙
'kHz_TRS' num2str(threshold*1000) 'pA_LP' num2str(filter/1000) 'kHz_' type↙
'.txt'];

for g=3:lofnames %the step size of two skips the index tdms files
        data=[];
        cd(char(folder));
        names=dir;
        switch char(system)
            case 'heka'
                data=sigopen(char(names(g).name));
                data=simple_lowpass_filter(data, SR, 15e3);
                if(filter~=0)
                    data=simple_lowpass_filter(data,SR,filter);
                end
                data_baseline=[];
                data_baseline=ultrasmoothv3(data, 10001); % calculates the↙
baseline
                if(isblockage==1)
                    peak_locs = find(data > (data_baseline+threshold));
                else
                    data=-data;
                    data_baseline=-data_baseline;
                    peak_locs = find(data > (data_baseline+threshold));
                end
                factor1=1;
                factor2=62;
                factor3=0;
            case 'hekaclogprotv2'
                data=clogprotopenv2(char(names(g).name));
```

```
                data=simple_lowpass_filter(data, SR, 15e3);
                if(filter~=0)
                    data=simple_lowpass_filter(data,SR,filter);
                end
                data_baseline=[];
                data_baseline=ultrasmoothv3(data, 10001); % calculates the↙
baseline
                if(isblockage==1)
                    peak_locs = find(data > (data_baseline+threshold));
                else
                    data=-data;
                    data_baseline=-data_baseline;
                    peak_locs = find(data > (data_baseline+threshold));
                end
                factor1=1;
                factor2=62;
                factor3=0;
             case 'hekaclogprotv1'
                data=clogprotopen(char(names(g).name));
                data=simple_lowpass_filter(data, SR, 15e3);
                if(filter~=0)
                    data=simple_lowpass_filter(data,SR,filter);
                end
                data_baseline=[];
                data_baseline=ultrasmoothv3(data, 10001); % calculates the↙
baseline
                if(isblockage==1)
                    peak_locs = find(data > (data_baseline+threshold));
                else
                    data=-data;
                    data_baseline=-data_baseline;
                    peak_locs = find(data > (data_baseline+threshold));
                end
                factor1=1;
                factor2=62;
                factor3=0;
            case 'jenset'
                data=1e9.*simple_tdms_2c(char(names(g).name));
                data_baseline=[];
                data_baseline=data(:,1); % calculates the baseline
                if(filter~=0)
                    data_baseline=simple_lowpass_filter(data_baseline, SR,↙
filter);
                    data=simple_lowpass_filter(data(:,2),SR,filter);
                end
                residuemean=mean(data);
                data=data-residuemean;
                peak_locs=find(data>threshold);
                factor1=0;
                factor2=10000;
                factor3=residuemean;
             case 'text'
                data=-load(char(names(g).name));
                if(filter~=0)
                    data=simple_lowpass_filter(data,SR,filter);
                end
```

```
                data_baseline=[];
                data_baseline=ultrasmoothv3(data, 50001); % calculates the↙
baseline
                if(isblockage==1)
                    peak_locs = find(data > (data_baseline+threshold));
                else
                    data=-data;
                    data_baseline=-data_baseline;
                    peak_locs = find(data > (data_baseline+threshold));
                end
                factor1=1;
                factor2=500;
                factor3=0;
            case 'lbheka'
                data=sigopen(char(names(g).name));
                data=simple_lowpass_filter(data, SR, 10e3);
                if(filter~=0)
                    data=simple_lowpass_filter(data,SR,filter);
                end
                data_baseline=[];
                data_baseline=ultrasmoothv3(data, 1001); % calculates the↙
baseline
                if(isblockage==1)
                    peak_locs = find(data > (data_baseline+threshold));
                else
                    data=-data;
                    data_baseline=-data_baseline;
                    peak_locs = find(data > (data_baseline+threshold));
                end
                factor1=1;
                factor2=7;
                factor3=0;

            case 'jensetctc'
                data=1e9.*simple_tdms_ctc_2c_new(char(names(g).name));
                dataraw=data(:,2);
                data_baseline=[];
                data_baseline=data(:,1); % calculates the baseline
                if(filter~=0)
                    data_baseline=simple_lowpass_filter(data_baseline, SR,↙
filter);
                    data=simple_lowpass_filter(data(:,2),SR,filter);

                end
                residuemean=mean(data);
                data=data-residuemean;
                dataraw=dataraw-mean(dataraw);
                peak_locs=find(data>threshold);
                factor1=0;
                factor2=10000;
                factor3=residuemean;

            case 'jensetctcv2'
                data=1e9.*simple_tdms_ctc_2c_new(char(names(g).name));
                dataraw=data(:,2);
                data_baseline=[];
```

```
                data_baseline=data(:,1); % calculates the baseline
                if(filter~=0)
                    data_baseline=smooth(data_baseline, round(SR/filter));
                    data=smooth(data(:,2),round(SR/filter));

                end
                residuemean=mean(data);
                data=data-residuemean;
                dataraw=dataraw-mean(dataraw);
                peak_locs=find(data>threshold);
                factor1=0;
                factor2=10000;
                factor3=residuemean;

        end

        SR = samplingrate;
        Q = 1/SR;
        time = Q:Q:Q*length(data); % sets the time column according to↙
100kHz sampling rate
        time=1000*transpose(time);

        events=[];
        lengthofdata=length(data);


        %Loop that finds the positive and then the negative peaks

        %----------------------------------------




        if(length(peak_locs)==0)%4 - if there is no data point above the↙
threshold, the loop skips to the second iteration(negative events)
            cd ..
            continue
        else

            lofpeak_locs=length(peak_locs); %
            peak_starts_ends = [];

            start_sample = 1;

            peak_start = peak_locs(start_sample);
            peak_end = peak_locs(start_sample);
            %-------------------------------------------
            i=1;
%Note: I changed the beginning and ending of the event to the half of the
%trhreshold from quarter of the threshold on 04272015

            while i<lofpeak_locs % finds the beginning of the event. Traces↙
the data points backward until it drops below 20% of the threshold level.

                a=0;
                while data(peak_locs(i)-a)>(factor1*(data_baseline↙
```

```
(peak_locs(i)-a))+(threshold/2))
                    a=a+1;
                    if((peak_locs(i)-a) < 1)
                           break
                    end
                end

                peak_start=peak_locs(i)-(a-1);

                a=0;
                b=1;
                while ((peak_locs(i+b)-peak_locs(i+b-1))<factor2) % finds↙
the ending of the event. Traces the data points forward until it drops↙
below 20% of the threshold level.
                    b=b+1;
                    if(((i+b) > lofpeak_locs))% | find(data(peak_locs(i):↙
peak_locs(i+b))<mean(data_baseline(peak_locs(i):peak_locs(i+b)))) )
                           break
                    end
                end

                b=b-1;

                while data(peak_locs(i+b)+a)>(factor1*data_baseline↙
((peak_locs(i+b)+a))+(threshold/2))
                    a=a+1;
                    if((peak_locs(i+b)+a) > lengthofdata)
                           break
                    end
                end

                peak_end=peak_locs(i+b)+(a-1);



                baseline = mean(data_baseline(peak_start:peak_end))-↙
factor3;
                peakmax = max(data(peak_start:peak_end))-baseline*factor1;

                peak_startt=time(peak_start);
                peak_endt=time(peak_end);
                peakduration=peak_endt-peak_startt;

                chargedef = sum(data(peak_start:peak_end)-data_baseline↙
(peak_start:peak_end))*((1/SR)*1e-9/1.6e-16);  % In units of kilo electrons

                while( peak_locs(i)<= peak_end) %updates the count of↙
events
                    i=i+1;
                    if(i>lofpeak_locs)
                        break
                    end
                end

                blockageratio=100*(peakmax/baseline);
```

```
                if(findext==1)
                    [extrematime extremavals transitiontime transitionvals]↙
= findextrema(time(peak_start:peak_end),data(peak_start:peak_end),dataraw↙
(peak_start:peak_end),baseline,plotevent);%
%                     if(skip==1)
%                         continue
%                     end
%                     size(extrematime)
%                     size(extremavals)
%                     size(transitiontime)
%                     size(transitionvals)
%                     '-----------------------------'
                    events=[events; (g-2) peak_startt peak_endt↙
peakduration peakmax abs(baseline) abs(blockageratio) chargedef extrematime↙
(1:5,1)' extremavals(1:5,1)' transitiontime(1:6,1)' transitionvals(1:↙
6,1)'];
                else
                    events=[events; (g-2) peak_startt peak_endt↙
peakduration peakmax abs(baseline) abs(blockageratio) chargedef];
                end

            end


        end

        cd ..

        dlmwrite(confilename, events, 'delimiter',  '\t', '-↙
append','precision','%.10f');

end

beep on;
beep;
```